Gain through filtering in fiber cavity resonators

Stefano Negrini

▶ **To cite this version:**

Stefano Negrini. Gain through filtering in fiber cavity resonators. Optics [physics.optics]. Université de Lille, 2023. English. NNT : 2023ULILR049 . tel-04500081

HAL Id: tel-04500081
https://theses.hal.science/tel-04500081

Submitted on 11 Mar 2024

HAL is a multi-disciplinary open access archive for the deposit and dissemination of scientific research documents, whether they are published or not. The documents may come from teaching and research institutions in France or abroad, or from public or private research centers.

L'archive ouverte pluridisciplinaire **HAL**, est destinée au dépôt et à la diffusion de documents scientifiques de niveau recherche, publiés ou non, émanant des établissements d'enseignement et de recherche français ou étrangers, des laboratoires publics ou privés.

Université de Lille

Université de Lille

Doctoral School **ED SMRE 104**

University Department **Laboratoire de Physique des Lasers, Atomes et Molécules - PhLam**

Thesis defended by **Stefano Negrini**

Defended on **28th November, 2023**

In order to become Doctor from Université de Lille

Academic Field **Physics**

Speciality **Optics and Lasers, Physical Chemistry and Atmosphere**

Gain through filtering in fiber cavity resonators

Thesis supervised by Arnaud Mussot Supervisor
Matteo Conforti Co-Supervisor

Committee members

Referees	Giovanna Tissoni	Professor at Institut de Physique de Nice
	Yannick Dumeige	Professor at Université de Rennes - Président du Jury
Examiners	Stefano Trillo	Professor at Università di Ferrara
	Auro M. Perego	Senior Researcher at Aston Institute of Photonique Technologies
	Saliya Coulibaly	Maître de Conference HDR Université de Lille
Supervisors	Arnaud Mussot	Professor at Université de Lille
	Matteo Conforti	Chargé de Recherche HDR PhLam UMR 8523 CNRS

Colophon

Doctoral dissertation entitled “Gain through filtering in fiber cavity resonators”, written by Stefano Negrini, completed on 27th February, 2024, typeset with the document preparation system LaTeX and the yathesis class dedicated to theses prepared in France.

Université de Lille

Université de Lille

Doctoral School **ED SMRE 104**

University Department **Laboratoire de Physique des Lasers, Atomes et Molécules - PhLam**

Thesis defended by **Stefano Negrini**

Defended on **28th November, 2023**

In order to become Doctor from Université de Lille

Academic Field **Physics**

Speciality **Optics and Lasers, Physical Chemistry and Atmosphere**

Gain through filtering in fiber cavity resonators

Thesis supervised by Arnaud Mussot Supervisor
Matteo Conforti Co-Supervisor

Committee members

Referees	Giovanna Tissoni	Professor at Institut de Physique de Nice
	Yannick Dumeige	Professor at Université de Rennes - Président du Jury
Examiners	Stefano Trillo	Professor at Università di Ferrara
	Auro M. Perego	Senior Researcher at Aston Institute of Photonique Technologies
	Saliya Coulibaly	Maître de Conference HDR Université de Lille
Supervisors	Arnaud Mussot	Professor at Université de Lille
	Matteo Conforti	Chargé de Recherche HDR PhLam UMR 8523 CNRS

Université de Lille

Université de Lille

École doctorale **ED SMRE 104**

Unité de recherche **Laboratoire de Physique des Lasers, Atomes et Molécules - PhLam**

Thèse présentée par **Stefano Negrini**

Soutenue le **28 novembre 2023**

En vue de l'obtention du grade de docteur de l'Université de Lille

Discipline **Physics**

Spécialité **Optics and Lasers, Physical Chemistry and Atmosphere**

Gain induit par des filtres dans les cavités fibrées passives

Thèse dirigée par Arnaud Mussot directeur
Matteo Conforti co-directeur

Composition du jury

Rapporteurs	Giovanna Tissoni	professeure à l'Institut de Physique de Nice
	Yannick Dumeige	professeur à l'Université de Rennes - Président du Jury
Examinateurs	Stefano Trillo	professeur à l'Università di Ferrara
	Auro M. Perego	directeur de recherche à l'Aston Institute of Photonique Technologies
	Saliya Coulibaly	Maître de Conference HDR Université de Lille
Directeurs de thèse	Arnaud Mussot	professeur à l'Université de Lille
	Matteo Conforti	Chargé de Recherche HDR PhLam UMR 8523 CNRS

This thesis has been prepared at the following research units.

Laboratoire de Physique des Lasers, Atomes et Molécules - PhLam
2, Av. Jean Perrin
59650 Villeneuve-d'Ascq
France

Institut de Recherche sur les Composants logiciels et matériels pour l'Information et la Communication Avancée (IRCICA)
50, Av. Halley
59650 Villeneuve-d'Ascq
France

Fundings

This Project has received funding from the European Union's Horizon 2020 research and innovation programme under the Marie Sklodowska-Curie grant agreement No 861152

Not all those who wander are lost;

J.R.R. Tolkien

Mobilis in Mobili - Devise du Nautilus

Jules Verne

Gain through filtering in fiber cavity resonators

Abstract

In this work, we study the phenomenon of modulation instability (IM) in fiber ring resonators, induced by asymmetric spectral losses in the form of a filter. The phenomenon, known as gain through filtering (GTF), consists in the modification of the phase matching condition of the resonator, given by the phase signature of the filter. We first characterised this phenomenon theoretically and experimentally in a passive fibre resonator for both normal and anomalous dispersion regimes, highlighting the relationship between GTF instabilities and parametric MI. We then developed a theoretical model to describe the formation of GTFs in a polarisation-maintaining (PM) cavity. Using this model, we have shown how it is theoretically possible to obtain two MI spectra with detuned spectral peaks. This is made possible by using a PM filter with a different loss profile in the two polarisation axes. In the more general context of fibre cavities, we have studied the effect of a synchronisation mismatch between the repetition rate of the pulse train driving the cavity and the natural repetition rate of the cavity. The mismatch results in a shift of the sideband of the MI spectra due to the competition between two MI regimes: absolute and convective. Finally, we built two active cavity devices. They consist of a fibre cavity in which a section of doped fibre (erbium or thulium dopant) is embedded in the coil to act as an amplifier. By carefully adjusting the gain of the amplifier, it's possible to compensate for the losses and still remain in a passive regime (below the lasing threshold). By using erbium-doped fiber as active media we were able to obtain GTF at very low power, while by using thulium-doped fiber we were able to generate MI at a wavelength of $2\mu m$.

Keywords: nonlinear optics, optical fiber, passive fiber cavity, modulation instability, gain through filtering, active cavity

Laboratoire de Physique des Lasers, Atomes et Molécules - PhLam
2, Av. Jean Perrin – 59650 Villeneuve-d'Ascq – France

Gain induit par des filtres dans les cavités fibrées passives

Résumé

Dans ce travail, nous étudions le phénomène d'instabilité de la modulation (IM) dans les résonateurs en anneau à fibre, induit par des pertes spectrales asymétriques. Le phénomène, connu sous le nom de gain through filtering (GTF), consiste en la modification de la condition accord de phase du résonateur, donnée par la signature de phase du filtre. Nous avons d'abord caractérisé ce phénomène théoriquement et expérimentalement dans un résonateur à fibre passif pour les régimes de dispersion normale et anormale, en mettant en évidence la relation entre les instabilités GTF et le MI paramétrique. Nous avons ensuite développé un modèle théorique pour décrire la formation des GTF dans une cavité à maintien de polarisation (PM). En utilisant ce modèle, nous avons montré comment il est théoriquement possible d'obtenir deux spectres MI avec des pics spectraux désaccordés. Ceci est possible en utilisant un filtre PM avec un profil de perte différent dans les deux axes de polarisation. Dans le contexte plus général des cavités à fibres, nous avons étudié l'effet d'un décalage de synchronisation entre le taux de répétition du train d'impulsions qui alimente la cavité et le taux de répétition naturel de la cavité. Le décalage entraîne un déplacement de la bande latérale des spectres MI en raison de la concurrence entre deux régimes MI : absolu et convectif.Enfin, nous avons construit deux dispositifs à cavité active. Ils consistent en une cavité à fibre dans laquelle une section de fibre dopée (dopant erbium ou thulium) est incorporée dans la bobine pour agir comme un amplificateur. En ajustant soigneusement le gain de l'amplificateur, il est possible de compenser les pertes tout en restant dans un régime passif (en dessous du seuil de télédiffusion). En utilisant une fibre dopée à l'erbium comme média actif, nous avons pu obtenir une FGT à très faible puissance, tandis qu'en utilisant une fibre dopée au thulium, nous avons pu générer un MI à une longueur d'onde de $2\mu m$.

Mots clés : optique non linéaire, fibre optique, cavité de fibre passive, instabilité de la modulation, gain par filtrage, cavité active

Remerciements

First of all, I would like to thank the PhLam laboratory for hosting me during these three years. In particular, the director, Cristian Focsa, and the director of the PhD programme, Céline Toubin. I would also like to mention the project that allowed me and five other amazing people from all over Europe to spend three years (or more) studying frequency combs and their applications: Horizon 2020 Mefista ETN (Grant Agreement No. 861152).

I would really like to thank all the members of the Jury who took the time to read this work: Mme. Giovanna Tissoni, Professor from the Institute of Physics of Nice, Yannick Dumeige, Professor from the University of Renne, Stefano Trillo, Professor from the University of Ferrara, Auro Michele Perego, research director from the Aston Institute of Photonic Technologies (Birmingham, UK) and Saliya Coulibaly, metre de conferance from University of Lille.

I always like practical work. And if this thesis depended solely on my organisational skills and desires, I'd probably be lost under a mountain of fibre reels and filters, with few results and a big headache. I really wants to show some gratitude to my supervisors in this big project. In my experience, a good supervisor is not only someone who is able to lead their group scientifically, but also someone who is able to create a sense of cohesion between the members of the group. So I really have to thank Arnaud Mussot, not only for the scientific support and guidance during this three-year project, but also for the great example of how a good team should work. But I'll take the credit for the Negroni. Thanks to Matteo Conforti, not only for meticulously finding all the errors in every single work I've done here, but also for his great sympathy and support. As we say in the team, Matteo is always right.

I would also like to thank Auro M. Perego for welcoming me into his group at Aston University during my two-month secondment in Birmingham. It was a pleasure to work in such a friendly and stimulating environment. A special though also for Stefano Trillo for having teaching me the basics of elctro-magnetic propagation and nonlinear optics.

During these three years, I met a lot of nice people. Some were fellow doctoral students, some were staff at our research facility here in Villenevue d'Ascq. Not

only did we share an infinite number of lunches, but we also shared a world pandemic, which is something not everyone can say! It was so great to work with all of you and I will never forget this time. I'll try to list everyone in order of appearance: Guillaume and Dylan, postgraduates (now doctors) who really helped me, especially (but not only) in the beginning when my French was, let's say, not the best. JB, Etienne and Andrea, post-docs during my first month here. Then: Gaëlle (without her, no one would remember to eat at 12.06), Vincent (who always has a good word for everyone), Jean (he's a wise man, nothing to add), Aymeric (he knows pretty much everything), Laure (who always brought us cake) and Sarah (who unfortunately became addicted to crossword puzzles), always next door for lunch. Next, some fellow travellers under the same supervisor: Eve-Line and Thomas, representing the two extremes of the behavioural spectrum: the first one, one of the most spontaneous and energetic people I've ever met, and the second one, one of the most composed and tidy people I've ever met, thank you both, I'll try to take some examples from you. Thanks also to the infinitely friendly Maroun and Alex, even though their office was far away from mine (about 6 metres), we had some opportunities to have a chat and it was always nice. The newcomers: Eloïse and Nolan, good luck for your future!

A big thank you to the entire Photonique Team: Monika, Laurent, Geraud, Alex, Andy, Sid, Esben..and many other. It was a real pleasure.

My thesis was part of an international project. This allowed me to meet some very fantastic people all over Europe! I would like to thank and remember the fellow PhD students of our European project, MEFISTA: Nayeem, Moritz, Qing, Alberto and Anamika. We shared the endless bureaucratic delays of the pandemic, but also some very nice and laughing dinners. Thank you for making everything a little more bearable.

For those who though about me, over there in Italy, I see you my friend! Thanks to my family, especially to Chiara. Without you it wouldn't have been possible.

Contents

Introduction

Of all the physical phenomena that human kind has tamed in history, light is one of the most interesting and useful. Not only it allows the peregrine traveller to find its path into the night, but it has always been used to communicate messages faster and far away, like the lighthouses around the coast of every sea or, in more recent time, the fiber optical based communication networks.

The science that studies light and its interaction with matter is called optics. When the interaction of light and matter produces intensity dependent changes in the physical properties of the medium through which the light travels, we enter the domain of nonlinear optics. The history of non-linear effects is relatively recent: Kerr effects were first theorised by John Kerr in 1850. Raman scattering [1] was actually discovered and measured by Raman and Krishnan in 1928, and two-photon absorption was first theorised by Maria Göppert-Mayer [2] in 1930. The discovery of laser radiation by T. Maiman in 1960 [3, 4] was a real milestone in the history of optical technologies, no exception for the study of nonlinear phenomena. In 1961, second harmonic generation was observed by Franken [5], and soon after two-photon absorption by Kaiser [6]. Then, in very fast succession, stimulated Raman scattering (SRS) [7, 8], stimulated Brillouin scattering (SBS) [9], four-wave mixing [10] and intensity dependent refractive index [11] where observed by means of lasers.

With the discovery of low loss silica fibres in 1970 [12] another major revolution in telecommunications began, giving to the laser an efficient medium for light transmission. The high photon density provided by laser sources confined in the small diameter of the core of a low-loss fibre created the perfect environment for studying nonlinear effects. Indeed, since 1972, a number of nonlinear effects have been characterised in fibre optics, including SBS [13], SRS

[14], self-phase modulation [15], optical Kerr effect [16], FWM [17] and also fibre solitons [18, 19].

In the 1980s [20], a nonlinear phenomenon already known in other fields of physics [21, 22], was theorised in the field of optical fibres: Modulation Instability (MI). In this context, MI can appear in the anomalous dispersion regime of an optical fibre thanks to the interplay between dispersion and nonlinear Kerr effect. This leads to a phase matching between the pump and a specific frequency that, as a consequence, is amplified and grows in space. In the time domain, this lead to the formation of a train of pulses [23, 24], while in the frequency domain the spectrum develops sidebands around the central pump [25]. After the first experimental observation, MI has to be a fundamental effect for triggering effects such as supercontinuum generation [26] or rogue wave formation [27, 28, 29].

The first studies of MI in optical fibres were made using an anomalous dispersion fibre as the medium, as this was a critical requirement for the phase matching condition. The generation of MI in the positive dispersion regime has been explored with new degrees of freedom added to the system such as periodic variation of power [30], periodic variation of nonlinearity [31], birefringence [32, 33] and dispersion modulation [34, 35, 36, 37, 38, 39, 40].

The efficiency of non-linear effects can be increased by using resonant cavities. These systems consist of loops created with mirrors, optical fibres or bulk materials in which light can circulate and interact with the input signal. The structure of such devices leads to a variety of complex phenomena such as optical bistability, self-oscillation and chaotic behaviour [41, 42, 43].

Regarding cavity modulation instability, the phenomenon was first observed in 1988 [44] in an unstabilised cavity. In the early '90s, theoretical studies of Healterman *et al.* deeply explored MI in cavity devices [45, 46], but only in 1997 Coen *et al.* created a suitable stabilised setup for studying the phenomenon [47]. Since then, a number of interesting phenomena have been demonstrated such as MI-induced bistable switching [43, 48] or the stable generation of pulse trains [49]. Fibre cavities then proved to be an optimal platform for the formation and study of temporal cavity solitons [50]. Besides the fundamental interest, some interesting applications of cavity solitons have been proposed, such as their use

as bits in all-optical buffers, especially in microresonators [51, 52, 53]. It has also been shown how MI is the fundamental phenomenon that allows the creation of Kerr frequency combs, with applications ranging from metrology, precision spectroscopy or sensing [54, 55, 56].

An important parameter which rule the MI dynamics in optical fiber is the loss term. In long range communications, MI can be a limiting factor. In this context many studies have been conducted to characterise the dependency of MI from losses [57, 25, 58]. From a more fundamental point of view, in a fascinating study of 2004, Tanemura *et al.* demonstrated that it is possible to stimulate MI in normal dispersion fiber, by means of wavelength-depending losses, asymmetric respect a central pump. More recently, this study has been expanded, showing how loss-induced MI is actually very general phenomenon in nonlinear optical system [59] which can be exploited in fiber amplifiers, optical parametric oscillators and frequency combs generation. The existence of spectral-dependent losses can also indirectly lead to phase matching by altering the system's phase mismatch parameter. This can be achieved thanks to the phase profile naturally associated to the dissipation of the filter by the Kramers-Kronig (KK) relations. That means that loss-induced MI can be conveniently obtained with narrow filters, such as Fiber Bragg Grating (FBG). In the context of fiber cavity resonator, the theory of this phenomenon, called Gain-Through-Filtering (GTF), has been extensively illustrated by Perego *et al.* [60], and the phenomenon has been experimentally demonstrated by Bessin [61] in 2019. In the latter, the authors exploited GTF to generate frequency tuneable optical frequency combs in a fiber cavity, by changing the frequency distance between the filter and the pump of the system.

In this work, we aim to characterise GTF in fibre cavities from a broader perspective. In particular, we investigate how GTF instabilities coexist with parametric instabilities and how parameters such as phase detuning, input power and dispersion influence their evolution. We have generalised the theory of GTF [60] to the case of a polarization-maintaining (PM) fibre cavity. The aim of this theoretical study is to demonstrate the generation of a dual-frequency comb in a fiber resonator, which have grate interest in domain such as spectroscopy [62, 63]. Enhancing the efficiency of our experimental setup is an important

point of this study. Inspired by the work of Englebert *et al.*, we developed an active cavity resonator [64, 65, 66], with which we are able to generate GTF at ultra-low input power. We also developed a dedicated theory for modeling GTF in an active cavity. Using the same idea, we were able to record MI spectra in a resonator pumped at $2\mu m$ for the first time. Finally, we present a study to understand the effect of a synchronisation mismatch between the pulse drive train and the natural repetition rate of the cavity.

We would like to mention that part of this work was possible thanks to the collaboration of several people. In particular: Nicolas Englebert, of the ULB, for the development of the active cavity; Auro M. Perego and Minji Shi, for the theory of GTF in the active cavity; Moritz Bartnick, within the ITN Mefista project, for the study of MI at 2 μm, and Saliya Coulibaly for the study of the effects of synchronisation mismatch in fibre cavities.

The manuscript is organized as follows:

In **Chapter 1** we give a general overview of light propagation in optical fibres and optical fibre resonators, describing the characteristics of these devices. We also introduce the two models used to describe the propagation of light and nonlinear effects in fibre resonators: The Ikeda map [67] and the Lugiato-Lefever equation [68]. In **Chapter 2** we formally introduce MI by performing a linear stability analysis for both Ikeda map and LLE models. With the same analysis we describe the main feature of GTF. In **Chapter 3** we describe the main experimental setup, focusing on the adaptation of the Pound-Drever-Hall stabilisation technique. We then theoretically and experimentally characterise the coexistence of GTF and parametric MI, both in the normal and anomalous dispersion regime of a fibre resonator. In particular, we focus on the dependence of these instabilities on parameters such as linear phase detuning and input power. In **Chapter 4** we develop a model to describe polarization maintaining GTF, with the goal of developing dual-frequency-comb spectra. We adapted the Ikeda Map and LLE models to a polarization maintaining (PM) resonators, and performed a linear stability analysis to compute the parametric gain. Both the parametric gain and the MI spectra are then characterized, as functions of the main parameters of the model. In **Chapter 5** we illustrate our theoretical and experimental investigation of the effects of pump-cavity synchronisation

mismatch. Thanks to the implementation of a time-lens system in the setup, we are able to show the round-trip-to-roundtrip time drift of the modulated signal. In the frequency domain, a much less intuitive frequency shift of the MI sideband is recorded. In **Chapter 6** we describe the implementation of the active cavity experimental setup and GTF theory adapted to this device. With these elements, we are able to record GTF with dramatically lower power threshold, compared to the passive cavity case. Finally, in **Appendix A**, we report a preliminary study on the formation of MI in a cavity setup pumped at $2\mu m$. This is possible thanks to a further adaptation of the active cavity setup, which allows to compensate the losses that are normally too high to allow MI. To the best of our knowledge, this is the first experimental proof of MI at these wavelengths and paves the way for very interesting studies such as solitons formation and direct generation of optical frequency combs in the 2μm range.

Chapter 1

Fiber Optic cavity

In this chapter we propose a general overview of the main concepts involved in the propagation of light. The concept of optical resonator is then introduced, together with the two main models usually used to describe it: the full Ikeda map and Lugiato-Lefever equation. For both formulations, we will present some fundamental characterisations of the steady states of the cavity, both in the linear and nonlinear regime.

1.1 Light propagation in optical fiber

An optical fibre is a waveguide and, in its simplest form, is structured as a coaxial cylinder of silica glass of different compositions. The inner part, called *core*, is characterised by its refractive index n_1. An intermediate part, called *cladding*, is characterised by a slightly lower refractive index n_c. The outermost part is called *jacket* and has a protective purpose. The difference between the refractive indices of the core and the cladding gives this structure its guiding properties. In particular, the light that satisfies the condition of total internal reflection (TIR) [69], remains contained in the core and will propagate along the fibre. In general, the refractive index difference between the core and cladding is obtained by doping the glass during the manufacturing process.

This is just the simplest structure an optical fibre can have and it is called step index. By varying the geometry of the core and cladding, a wide range of

different fibres can be obtained: from graded index fibres (GRIN), in which the difference between the two indexes decreases gradually from one to the other, to hollow core fibres [70], in which the core is, as the name suggests, hollow, which are themselves a special type of photonic crystal fibre (PCF). The geometrical characteristics, as well as the refractive index, define the main properties of an optical fibre, such as losses, dispersion, birefringence, non-linear properties and number of modes. The mode is the transverse profile that the intensity of the light acquires as it propagates through a fibre, and for the purposes of this thesis we will focus only on single mode fibres, meaning that only the fundamental mode is sustained during propagation.

1.1.1 Losses

When light propagates through any material, it suffers losses. In optical fibres, a common way to define losses is by the attenuation factor α. If P_0 is the power launched at the input of an optical fibre, then after a propagation of L metres, the transmitted power P_T can be expressed as $P_T = P_0 \exp(-\alpha L)$.

Fibre losses depend on the wavelength of the light. In particular, for a standard fibre, there is a minimum value of about $0.2 dB/km$ in the region around 1.55 μm, which is therefore the "standard" wavelength in telecommunications.

Several factors contribute to the losses α: material absorption, physical bending that causes the light to escape the waveguide, dispersion losses and *Rayleigh scattering*. The latter is due to the intrinsic fluctuation of the density of the fibres, resulting in a fluctuation of the refractive index which causes the light to be scattered in all directions.

1.1.2 Chromatic dispersion

A fundamental property of light propagating in a dielectric medium is chromatic dispersion. This property is the result of the interaction between the light and the bound electrons of a medium, and results in a frequency dependence of the refractive index of the material $n(\omega)$. This means that the chromatic components of a wave packet travelling in a dielectric medium, such as an optical fibre, will travel at different speeds $c/n(\omega)$. In the low power regime, where non-linear

effects are not significant, this behaviour can lead to dispersion-induced pulse broadening, which is particularly detrimental in the propagation of short pulses. Assuming that the spectral width of an electromagnetic wave is much smaller than its centre frequency ($\Delta\omega << \omega_0$), the effect of fibre dispersion is accounted for by expanding the propagation constant β in a Taylor series around the carrier frequency ω_0:

$$\beta(\omega) = n(\omega)\frac{\omega}{c} = \beta_0 + \beta_1(\omega - \omega_0) + \frac{1}{2}\beta_2(\omega - \omega_0)^2 + \dots, \tag{1.1}$$

where

$$\beta_m = \left(\frac{d^m\beta}{d\omega^m}\right)_{\omega=\omega_0} (m = 0, 1, 2, \dots). \tag{1.2}$$

The parameter β_1 is the inverse of the group velocity, *i.e.*, the velocity at which the envelope of a pulse moves in a medium, while β_2 represents the group velocity dispersion (GVD). The GVD consist in the alteration of the velocity of propagation of different frequencies that compose a wave envelope which, at linear power, leads to the broadening of the envelope. It can also be expressed with a different parameter, D, defined as:

$$D = \frac{d\beta_1}{d\lambda} = -\frac{2\pi c}{d\lambda^2}\beta_2 = -\frac{\lambda}{c}\frac{d^2n}{d\lambda^2}. \tag{1.3}$$

One can define *zero-dispersion-wavelength* (ZDW) that wavelength at which the GVD equals zero and, in standard single-mode fibers, its value is approximately $\lambda_D \approx 1.3\ \mu$m.

The value of D and β_2 depends on the materials and geometric characteristics of the waveguide, so it is possible to shift the optical fibre ZDW through the typical telecom values of 1.55 μm, which is a common method to better control the pulse shape over long distances. This type of fibre is typically referred to as *Dispersion Shift Fibers* (DSF). The sign of the sign of β_2 identifies two different propagation regimes: *normal* ($\beta_2 > 0$), where the red components of the spectrum will travel faster than the blue components, and *anomalous* ($\beta_2 < 0$), where the the opposite is true. At low power, chromatic dispersion bring to the broadening of light pulses no matter the dispersion regime, but at high power the sign of β_2

could lead to fundamentally different effects, like in the self-phase modulation case (SPM) [71].

1.1.3 Fiber non-linearities and Kerr Effect

Nonlinear phenomena can occur in any dielectric medium exposed to a high intensity electromagnetic field. At a fundamental level, the non-linear response is related to the harmonic motion of the bound electrons under the influence of the optical fields. As a result, the total vector **P** induced by the electric field **E** is non-linear and satisfies

$$\mathbf{P} = \epsilon_0 \left(\chi^{(1)} \cdot \mathbf{E} + \chi^{(3)} \vdots \mathbf{EEE} \right) \tag{1.4}$$

where ϵ_0 is the vacuum permittivity, $\chi^{(j)}$ is the j_{th} order susceptibility and **E** is the electric field. We limited the expansion of **P** to the first and third order of $\chi^{(j)}$. For the focus of this dissertation, higher order susceptibilities are not taken into consideration, while the second order $\chi^{(2)}$ can be neglected considering the centro-symmetric nature of silica fibers. On the other hand, $\chi^{(3)}$ is responsible for a wide range of nonlinear phenomena, such as third-harmonic-generation, four-wave-mixing and non linear refraction. The first two are generally not very efficient in optical fibers, but a large number of non linear effects in optical fibers are a consequence of non-linear refraction. A typical example is Kerr effect, that consists in the dependency of the refractive index of the fiber from the intensity of the light intensity. In particular, the refractive index takes the form $n = n_0 + n_2 I$, where n_2 is the nonlinear-index coefficient, and I is the intensity of light. Often, it is practical to define the non-linear parameter of an optical fiber as $\gamma = n_2 \omega_0 / c A_{eff}$, where ω_0 is the frequency of the light, and A_{eff} is the effective mode area. In standard optical fibers ranges in $A_{eff} \approx 1 - 100 \mu m^2$, leading to a $\gamma \approx 1 - 100 W^{-}1/km$ with $n_2 \approx 2.6 \times 10^{-20} m^2/W$ [72].

1.1.4 Nonlinear Schrödinger Equation

One common model to describe the propagation of a pulse in an optical fiber is called Non Linear Shrödinger Equation (NLSE) [73] which, in its simpler form,

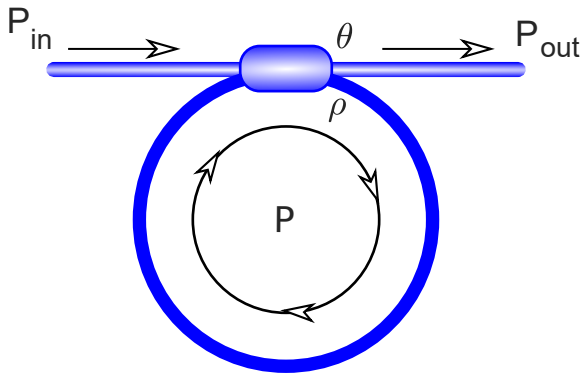

Figure 1.1 – Basic scheme of a fiber ring cavity. P_{in} is the power of the input signal, which is injected inside the resonator through the coupler, characterized by the reflection and transmission parameter, ρ and θ respectively. P is the intracavity power and P_{out} is the power of the signal coupled out of the cavity.

can be written as:

$$\frac{\partial E(z,\tau)}{\partial z} = -\frac{\alpha}{2}E(z,\tau) - i\frac{\beta_2}{2}\frac{\partial^2 E(z,\tau)}{\partial \tau^2} + i\gamma|E(z,\tau)|^2 E(z,\tau) \tag{1.5}$$

where τ is the time defined in the reference frame travelling at the same group velocity of the pulse at the carrier frequency ω_0, E is the envelope of the pulse and z is the longitudinal coordinate. In the equation there are several elements described in the previous paragraphs: α takes into account the fibre losses, β_2 describes the GVD and γ the non-linearities. This equation is the basic model used to simulate the evolution in time and space of a pulse propagating along optical fibers. If necessary, the model can be extended to include, for example, the effects of higher order dispersion ($\beta_3, \beta_4, \dots$) [74, 75] or other effects (Raman responses, self-steepening [76]).

1.2 Passive Optical Resonator

The model described in the previous section 1.1.4 illustrates the propagation of light in an optical fiber. The main devices analysed in this thesis are fiber optical cavities, which is a remarkably simple type of optical resonators. They are composed by piece of optical fiber, closed into a loop through an optical

coupler [47]. The coupler used for this kind of application is usually a 2x2 fiber coupler, described through its transmission (θ) and reflection (ρ) parameters. Without taking into account the losses of the coupler, those two parameters satisfy the relation $\rho^2 + \theta^2 = 1$. A schematic example of that a fiber cavity is provided in Fig 1.1. The optical power is injected through the input port, where it is partially coupled inside the cavity. The injected light travels along the cavity and, once it reaches the coupler, a portion is re-coupled inside the cavity, interfering with the input signal, while a portion is coupled outside the cavity through the output port. This continuous interaction between the intracavity and input fields, in a so called multi-pass configuration, is the fundamental mechanism which allows to enhance dynamics which would be difficult to study in a single-pass configuration, i.e. a simple optical fiber. In particular it allows the creation of complex dynamics, such as bistability [42, 43], and nonlinear effects such as chaos [41, 45]. The propagation of light inside the cavity is described by the NLSE Eq. (1.5), which takes into account the effects of losses, chromatic dispersion and the nonlinearity of the material. To complete the model of the system, one has to include the *cavity boundary conditions*, which takes into account the effect of the coupler. Mathematically:

$$E^{(m+1)}(0,\tau) = \theta E_{in} + \rho E^{(m)}(L,\tau)e^{i\phi_0}, \tag{1.6}$$

where $E^{(m)}(z,\tau)$ is the optical field at the m_{th} round-trip in the cavity, E_{in} is the input field, and ϕ_0 is the phase collected by the signal during propagation in the cavity. Eq. (1.6) has a very simple interpretation: the intracavity fields at the round trip $m+1$ are equal to the superposition of the input field θE_{in} with the recirculated intracavity field at the end of the round trip m $\rho E^{(m)}(L,\tau)e^{i\phi_0}$. This equation describes the interferometric nature of the device and in particular highlights the crucial role of ϕ_0, which can be described as $\phi_0 = \beta_0 L$ with $\beta_0 = \omega_0 n/c = 2\pi n/\lambda_0$. This linear phase can depend on the frequency of the signal ω_0, the length of the cavity L and its refractive index n. We will describe later the effect of the Kerr nonlinearity on the phase accumulated by the signal inside the cavity and how it fundamentally changes the behaviour.

In summary, the dynamics of a fiber cavity can be described by a mathemati-

cal model commonly knows as Ikeda map [77], which pair together NLSE and boundary condition equations, and reads:

$$\begin{cases} \dfrac{\partial E(z,\tau)^{(m)}}{\partial z} = -\dfrac{\alpha}{2}E(z,\tau) - i\dfrac{\beta_2}{2}\dfrac{\partial^2 E(z,\tau)^{(m)}}{\partial \tau^2} + i\gamma|E(z,\tau)^{(m)}|^2 E(z,\tau)^{(m)} \\ E^{(m+1)}(0,\tau) = \theta E_{in} + \rho E^{(m)}(L,\tau)e^{i\phi_0}. \end{cases} \tag{1.7}$$

This map can be extended to include the effect of, for example, higher order dispersion or additional components in the cavity, such as filters, as we will see in the next chapters.

1.2.1 Steady-states and cavity resonances

Given the description of the system, the first characterisation that can be done is the analysis of the steady state of the cavity. We consider a continuous wave ($\dfrac{\partial^2 E(z,\tau)^{(m)}}{\partial \tau^2} = 0$). The cw solution at the roundtrip m reads as:

$$E^{(m)}(z) = \bar{E}\exp(i\gamma P z),\ P = |\bar{E}|^2 \tag{1.8}$$

where $E^{(m)}(z)$ is the intracavity field of the cavity at round trip m, $\bar{E}$ is the stationary field solution, and P is the power associated with the stationary field. Stationary means that the field doesn't change from roundtrip to roundtrip, thus $E^{(m+1)}(0) = E^{(m)}(0) = \bar{E}$. We can now calculate the steady state of the cavity using the boundary conditions of the Eqs (1.6), which leads to:

$$\bar{E} = \frac{\theta E_{in}}{1 + \rho e^{i\phi_0}} \tag{1.9}$$

which in terms of measurable powers becomes:

$$P = \frac{\theta^2 P_{in}}{1 + \rho^2 - 2\rho\cos(\phi_0)} \tag{1.10}$$

Up to now, we considered the coupler in its ideal form, thus without taking into account the losses. There are two main kind of losses to consider: excess losses of the coupler (typically from 5 – 10%) and linear losses of the fiber, already

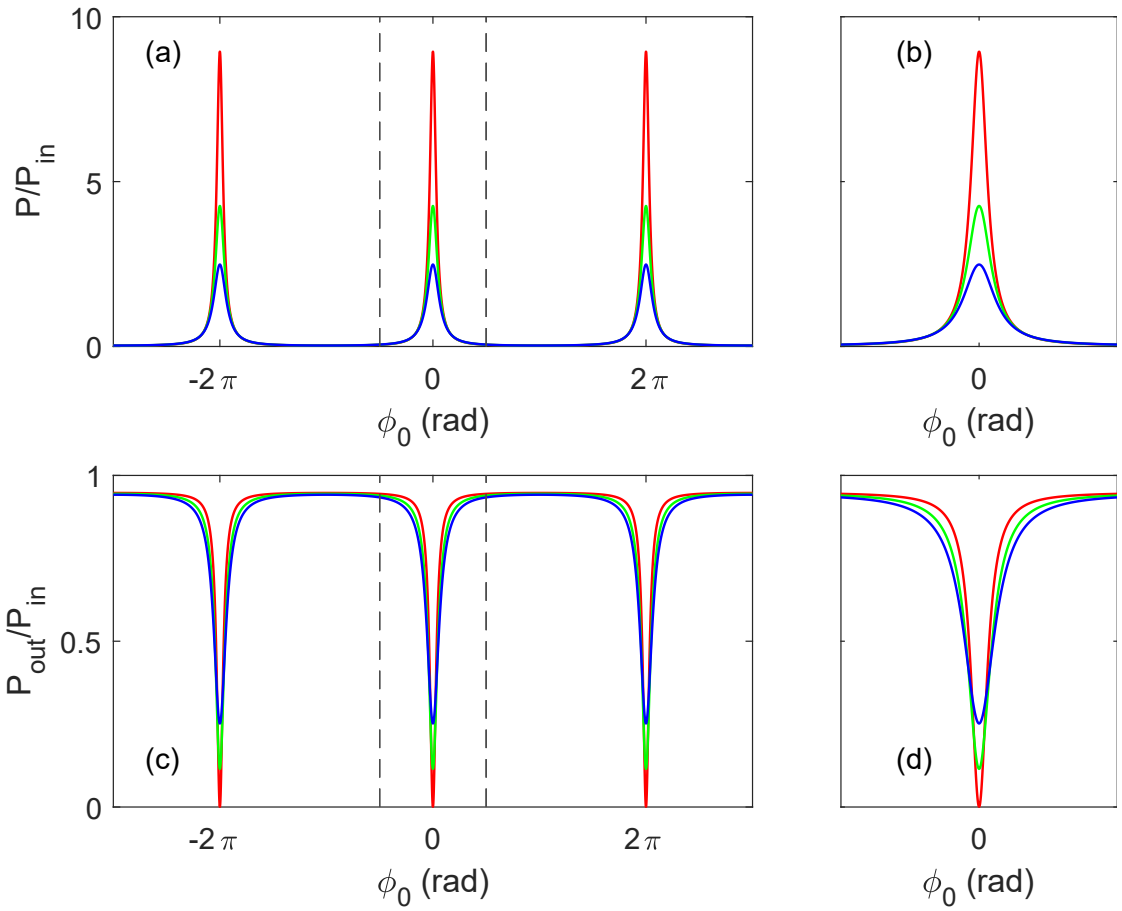

Figure 1.2 – Representation of the linear resonances of the cavity: (a) intracavity linear response of the cavity (Eq. (1.10)), (b) zoom of the response around the central resonance. (c) Output response of the cavity (Eq. (1.11)) and the relative zoom (d). For all the figures, the computation has been made with the following parameters: $L = 50\,m$, $P_{in} = 1\,W$, $\rho = \sqrt{0.9}$, $\theta = \sqrt{0.1}$, $k_0 = 5\%$ and the losses $a = [0.97, 0.92, 0.87]$ relatively, corresponding to a Finesse of 15, 20 and 30 relatively.

introduced before. One can simply lump all the losses in the coupler description, by re-defying the reflection and transmission coefficient as follows: $\rho = a\alpha_0\rho$ and $\theta = \alpha_0\theta$, with $\alpha_0 = \sqrt{1-k_0}$ and k_0 being the excess losses of the coupler, while $a = \exp(\alpha_f L/2)$ accounts for the linear losses. It is also possible to describe the relation between the input and output power as [78]:

$$P_{out} = \alpha_0^2 P_{in} - (1 - (a\alpha_0)^2)P. \tag{1.11}$$

A simple analysis of Eq. (1.10) shows that its maximum is reached for $\phi_0 = 2k\pi\, k \in \mathcal{N}$, the condition at which the cavity is said to be resonant. Remembering the linear phase $\phi_0 = \omega_0 nL/c = 2\pi f_0 nL/c$, we can see that it is proportional to the frequency of the driving pump. Thus, the 2π intervals between two successive resonances correspond to a frequency spacing usually referred to as the *free spectral range* ($FSR = c/nL$). From a practical point of view, this quantity is useful because it allows to define the fineness $\mathcal{F}$ as the ratio between the FSR and the full-width half-maximum (FWHM) of the resonance $\mathcal{F} = FRS/FWHM$. Then, knowing $\mathcal{F}$, one can estimate the losses of the cavity by the relation $\mathcal{F} = \pi/\alpha$, where α is the total power loss of the cavity (both linear and coupler excess losses).

Another practical use of the finesse parameter is to calculate the ρ factor directly, implicitly including all losses with the definition $\mathcal{F} = \pi\sqrt{\rho}/(1-\rho)$ [78, 79]. Losses can also be related to the quality factor of a cavity, defined as $\mathcal{Q} = \mathcal{F} \times 2\pi\omega_0/FSR$. Figures 1.2 illustrate the ratio P/P_{in} derived from Eq. (1.10) as a function of the linear phase ϕ_0 at different values of fineness. In particular, in Fig. 1.2(a) it is possible to see the typical Airy function profile of the resonance, which is periodically repeated for $\phi_0 = 2k\pi\, k \in \mathcal{N}$. Fig. 1.2 (b) is a zoom on the resonance corresponding to $\phi = 0$ rad, the blue, green and red traces represent a fineness of $[15, 20, 30]$ respectively. Physically, these plots represent the amount of power stored in the cavity and, as expected, the maximum is at $\phi_0 = 0 \mod (2\pi)$ rad. The cavity can store more power than is injected at the input, and when the driving input field is resonant, the intracavity power is at its maximum. The effect of losses is visible in the finesse evolution: the higher the losses, the lower and wider the resonance, and thus the lower the finesse.

Figures 1.2(c) and (d), are a plot of Eq. (1.11) as a function of the linear phase ϕ_0 at different finesse value. The interpretation of this function is complementary to that of the resonance function. Being the ratio between the output and input power, this function has values strictly in the interval $[0, 1]$. In ideal conditions (no losses), at the resonant frequency P_{out}/P_{in} is zero because all the input power is transmitted and stored inside the cavity, while outside resonance the same ratio is one because all the light bypasses the cavity. In reality, a percentage of the input light is always coupled to the output of the cavity (θ^2), and the

coupler suffers excess losses, so these two theoretical values are never reached in reality. The use of the transmission or resonance function to characterise the cavity depends on the situation. Getting access to the P_{in} of a cavity means having an additional coupler [47, 80], which can be convenient but adds more losses due to the additional splicing that has to be done.

To obtain a good quality cavity, it is desirable to work with the lowest possible losses. Typical values of finesse are in the range of $[10, 50]$ in passive fibre resonators [80, 81, 82], which are relatively small compared to other types of resonators [56, 53]. Recently, an interesting approach to dramatically improve the finesse of passive fibre cavities has been proposed by Englebert *et al.*. It consists of embedding an active medium in the cavity, such as an erbium-doped fibre, by keeping the gain below the lasing threshold. This makes it possible to compensate for the losses while keeping the entire cavity "passive" [64, 65]. With this method, finenesses of the order of 100 can be achieved, which is a huge improvement compared to a traditional passive fibre resonator.

1.2.2 Effect of Kerr non-linearities

At high optical powers, the guiding medium begins to behave in a non-linear manner. In particular, the signal propagating in the cavity at high power undergoes a phenomenon of self-phase modulation (SPM), as consequence of the Kerr effect. In this state, the total phase accumulated by the signal can be described as $\Phi = \phi_0 + \gamma LP$, where ϕ_0 is the linear phase, P is the intracavity power, L is the length of the cavity and γ is the nonlinear coefficient (or Kerr coefficient). Taking this into account, the intracavity power function is modified as follows:

$$P = \frac{\theta^2 P_{in}}{1 + \rho^2 - 2\cos(\phi_0 + \gamma LP)} \tag{1.12}$$

Eq. (1.12) can be solved numerically by fixing an input power as a function of ϕ_0. The result is shown in Fig. 1.3, where we have plotted it for $P_{in} = [0.1, 0.5, 1]\,W$ for the red, green and blue traces respectively. The first obvious difference from the linear case is the tilting effect due to the non-linear phase shift. Looking at the zoom of Fig. 1.3 (b), one can see that the shift of the peak of the resonances

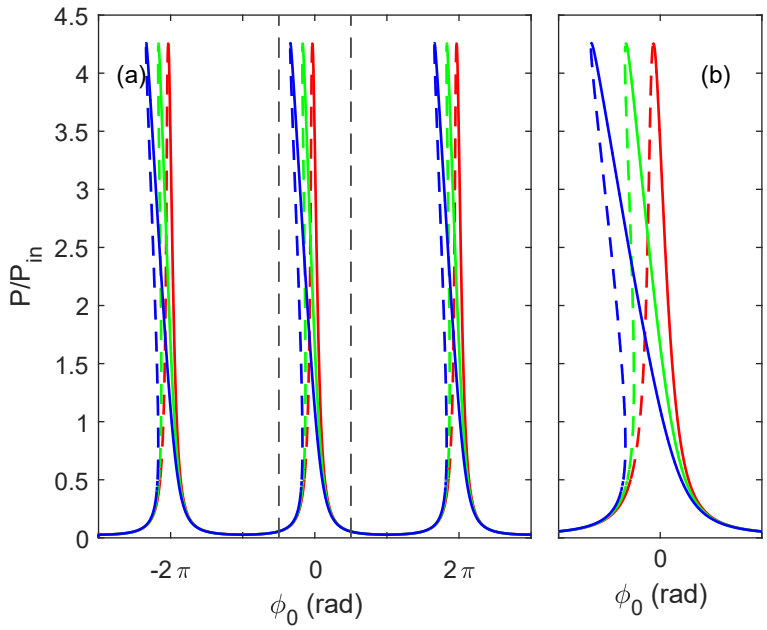

Figure 1.3 – Representation of the tilting action of the Kerr effect on the resonances of the cavity: (a) intracavity linear response of the cavity (Eq. (1.12)), (b) zoom of the response around the central resonance. The computation has been made with the following parameters: $L = 50\,m$, $\rho = \sqrt{0.9}$, $\theta = \sqrt{0.1}$, $k_0 = 5\%$, $\gamma = 5/W/km$, $a = 0.97$ corresponding to a Finesse of 30. The input power is $P_{in} = [0.1, 0.5, 1]\,W$ for the red, green and blue traces respectively.

is proportional to the input power: the higher the input power, the steeper the resonance. The physical meaning of a tilted resonance is that, for a given ϕ_0, the cavity can manifest more than one intracavity power, of which only some are stable. For example, in Fig. 1.3(b), the solid lines are the stable state that can be maintained inside the cavity, while the dashed lines are the unstable state. This situation is called "multi-stability" and it is the starting point for many non-linear phenomena such as soliton formation and shock waves [83, 42, 84, 41, 43, 85, 51, 86, 87].

1.2.3 Lugiato-Lefever Model

Under certain restrictions (listed below) it is indeed possible to derive from the Ikeda map of the system (1.7) a more compact model known as the Lugiato-Lefever equation (LLE) [68, 46, 88, 89]. This model is also known as the mean-

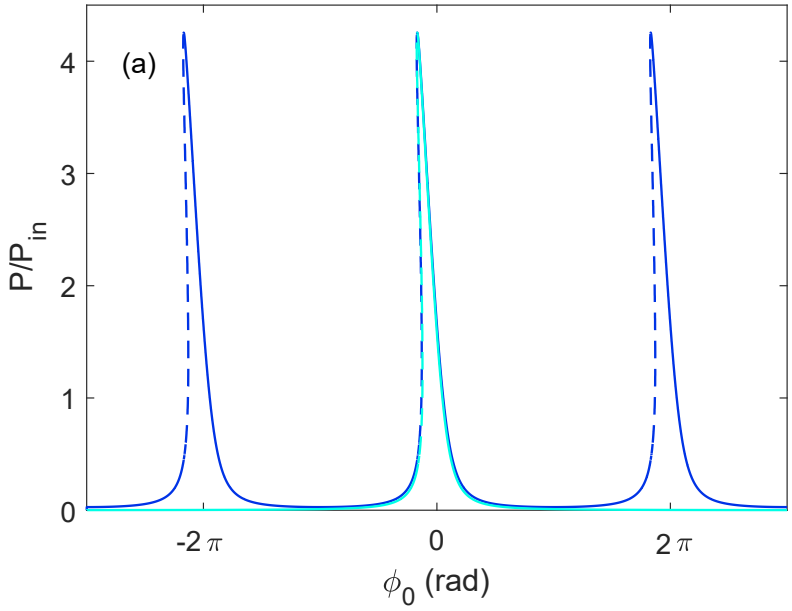

Figure 1.4 – Comparison between the resonances computed with the Ikeda map model (blue) and LLE model (cyan). The resonances for Ikeda map are computed from Eq. (1.12), while for the LLE Eq. (1.14) is used. In both cases, the parameters are: $L = 50\,m$, $P_{in} = 0.5\,W$, $\rho = \sqrt{0.9}$, $\theta = \sqrt{0.1}$, $k_0 = 5\%$, $\gamma = 5/W/km$, losses $a = 0.97$ relatively, corresponding to a finesse of 30.

field approximation and, as the name suggests, it is derived by averaging the NLSE over a round trip, including the boundary conditions. In order to be valid, several assumptions have to be made, the first of which is that the field does not vary much from round trip to round trip. It is also assumed that the total losses of the cavity are relatively small ($\alpha << 1$), that the phase of the input signal is relatively close to resonance ($|\phi_0 - 2k\pi| << 1$, $\gamma LP << 1$), and that the dispersion length of the fibre is greater than the length of the cavity. If these assumptions are met, the Lugiato-Lefever equation becomes:

$$\frac{\partial E(z,\tau)}{\partial z} = -\frac{\alpha}{L}E(z,\tau) - i\frac{\delta_0}{L} - i\frac{\beta_2}{2}\frac{\partial^2 E(z,\tau)}{\partial \tau^2} + i\gamma|E(z,\tau)|^2 E(z,\tau) + \frac{\theta}{L}E_{in} \qquad (1.13)$$

where $\delta_0 = 2k\pi - \phi_0$ is called the cavity phase detuning, it describes the phase shift between the pump signal and the nearest cavity resonance, and $\alpha = 1 - \rho$ is the total power dissipation of the cavity.

It is possible to compute the steady states ($\partial E/\partial z = 0$, $\partial E^2/\partial \tau^2 = 0$), which

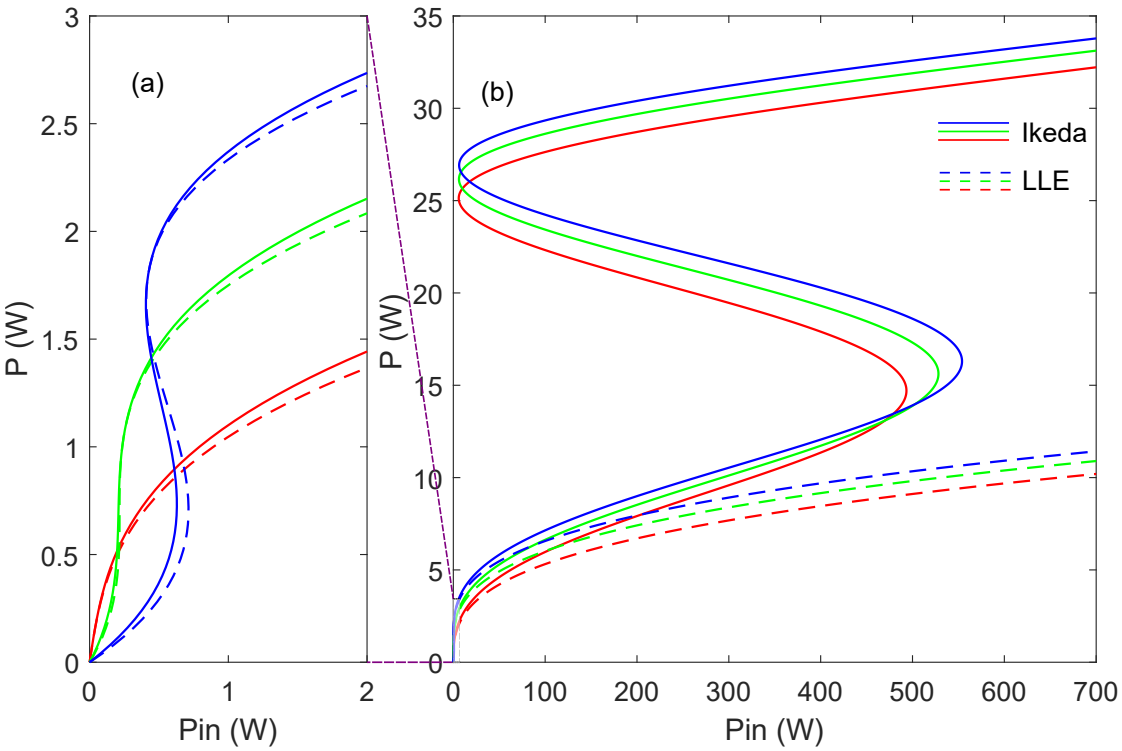

Figure 1.5 – Bistable response of a cavity. (a) is a zoom of the function for $P_{in} = [0, 2]\, W$. (b) plot of the same function for higher P_{in} interval, one can note the major difference between this models: the Ikeda map always present multiple branches, corresponding to multiple steady state, even if they occur for prohibitive input powers. The parameters are: $L = 50\, m$, $\rho = \sqrt{0.9}$, $\theta = \sqrt{0.1}$, $k_0 = 5\%$,losses $a = 0.97$, $\gamma = 5/W/km$, $\alpha = 1 - \rho$, $\phi_0 = [0, \alpha\sqrt{3}, 3\alpha]$ for the red, green and blue traces respectively.

correspond to the following equation:

$$\frac{P}{P_{in}} = \frac{\theta^2}{(\delta_0 - \gamma L P)^2 + \alpha^2}. \tag{1.14}$$

To highlight the differences between the Ikeda map model and the LLE model, we show in Fig. (1.4) a plot where we compare the steady state for the two models. The blue trace is for the Ikeda map and the cyan trace is for the LLE. The first and most obvious difference is that, as expected from the mathematical description, the LLE trace has only a single resonance. This is a direct consequence of the

single longitudinal mode hypotheses, and can indeed become a limiting factor when the intracavity power P becomes relatively high. Indeed, the effect of the power P is to tilt the resonance of the cavity through the Kerr effect (γLP). For sufficiently high powers, the resonances computed with the Ikeda map model can actually superimpose each other, but this is not the case with the LLE model due to the lack of neighbouring resonances.

Further differences between the two models can be highlighted by analysing P as function of P_{in} at a fixed phase detuning. In Fig. 1.5 we plot $P = f(P_{in})$ for different linear phases. The solid lines are the curves for the Ikeda map model and the dashed lines are for the LLE model. The red traces have a linear phase of zero, then the green and blue traces are increasingly detuned. In particular, in Fig. 1.5 (a) it is interesting to see that as the phase increases, the curves begin to take on a typical "S" shape, meaning that for a given ϕ_0, a single value of P_{in} corresponds to several possible values of P. This is an equivalent representation of the "multi-stable" regime described in the previous section, but using this description it is possible to identify the phase detuning at which the S-shaped function becomes multivalued. This phase is $\delta_0 = \alpha\sqrt{3}$ and whenever this threshold is crossed the cavity is in a multi-stable state.

For low power regimes, as in Fig. 1.5 (a), the overall difference between the Ikeda and LLE model is not very pronounced. A discrepancy is visible at high powers, as in Fig. 1.5 (b), where the Ikeda traces actually manifest more multi-valued branches, while the LLE traces continue without deviation. Again, the reason for this lies in the approximations made to derive the LL model, one of which is a low P. We note that these levels of input power ($> 100\ W$) are prohibitive in our context, but the deviation between the two models starts to be relevant already around ($20/30\ W$), which can be easily reached in pulsed driven systems.

The S-shape function helps to understand if the cavity can develop more stable states, but to understand if a state (P_{in}, P) is stable, another level of analysis has to be done. The stability of a given state (P_{in}, P, ϕ_0) can be studied by performing a linear stability analysis for the LLE relative to the ansatz $E = \bar{E} + b\exp\lambda t$ [90, 45]. After some simple calculation, one finds that the system is

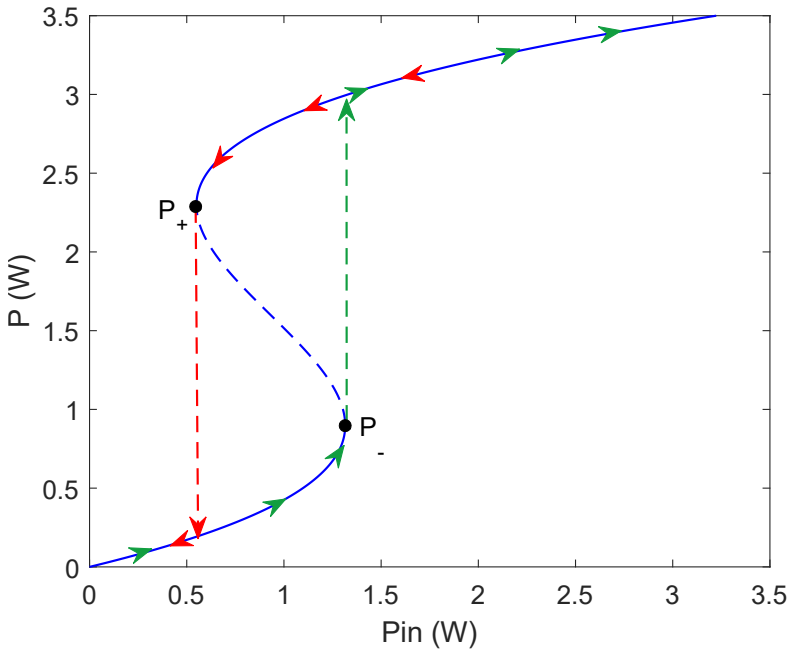

Figure 1.6 – Example of the hysteresis cycle of $P(P_{in})$ in case of a bistable cavity. The green arrows shows the path followed by P when starting from the lower branch of the curve and rising the input power, the red arrows shows the path of P when starting on the upper branch and lower the input power. The parameters are: $L = 50\,m$, $\rho = \sqrt{0.9}$, $\theta = \sqrt{0.1}$, $k_0 = 5\%$,losses $a = 0.97$, $\alpha = 1 - \rho$, $\phi_0 = 3\alpha$.

unstable whenever the following expression is positive:

$$\lambda = -\frac{\alpha}{L} \pm \sqrt{4\gamma P \frac{\delta_0}{L} - \left(\frac{\delta_0}{L}\right)^2 - 3(\gamma P)^2}. \tag{1.15}$$

In case of bistability, it is easy to demonstrate that the intracavity powers relatives to the negative sloped branch of the curves are unstable. In particular, it is possible to delimit the intracavity power P corresponding to the negative branch by calculating the roots of $\partial P_{in}/\partial P = 0$ which reads:

$$P_{\pm} = \frac{2\delta_0 \pm \sqrt{\delta_0^2 - 3\alpha^2}}{3\gamma L}. \tag{1.16}$$

These points are usually referred to as the up-switch knee $(P_{in}^{\uparrow}; P_{-})$ and the down-switch knee $(P_{in}^{\downarrow}; P_{+})$, so named because whenever the input power approaches

these values, the intracavity power jumps directly to the upper (or lower, depending on the sign of the change) stable state without entering the unstable negative-sloped branch. This mechanism is illustrated in Fig. 1.6: the blue curve is the representation of the S-shaped function at a fixed phase detuning δ_0 for the LLE. By increasing the input power, the intracavity power increases, following the green arrows on the lower branch of the curve. As soon as the input power reaches the up-switch knee value ($P\_$), the intracavity power jumps to the upper branch where it continues to follow the curve. On the other hand, if we start from the upper branch and reduce the input power, the intracavity power will fall, following the red arrows, to the down-switch knee point, where it will fall to the lower branch if it is exceeded. it is possible to note how, in this cycle, the intermediate branch is never reached by the intracavity field [80].

1.3 Summary

- In this chapter we have introduced the main notion behind light propagation in dispersive media, describing losses, chromatic dispersion and the nonlinear response of the medium. With that, we introduced the Non-Linear Schrödinger Equation (NLSE), which can be used to describe the propagation of light in non linear media.
- We introduced the basic structure of a fibre-optic resonator and define two of the main models used for its description: the Ikeda map and the Lugiato Lefever Equation (LLE) model. With these models we were able to characterise the basic feature of the resonator: steady states and resonances in the linear regime. We then considered the effect of non-linearities with the Kerr effect, and showed the main differences between the Ikeda map and the LLE model.

Chapter 2

Modulation Instability and Gain Through Filtering

This chapter is dedicated to the general description of Modulation Instability (MI) in fibre ring resonators and more specifically to the Gain-Through-Filtering (GTF) phenomenon, a particular method of inducing MI. In general, MI is a common nonlinear phenomenon [91] that can be found in many different fields of physics [21, 22, 92, 93], including optics [23]. In nonlinear optics, MI appears as the amplification of phase-matched frequencies rising symmetrically with respect to a high-power pump. In optical fibres, such an effect can be achieved thanks to the interplay between nonlinear and dispersive effects, and it's first observation in fibre optics dates back to 1986 [25]. The simpler form of MI is observed in the anomalous dispersion regime, unless the system has additional degrees of freedom, such as strong birefringence [94, 95], higher order dispersion [96], or multimode propagation [97]. In optical cavities, this additional degree of freedom is given by the interaction between the input and intracavity fields, which interfere with each other in a constructive way, depending on the phase mismatch between the pump and the resonant frequency of the cavity. The first experimental observation of this phenomenon was made in 1988 [44] in a non-stabilised cavity and in 1997 in a properly stabilised fibre-optic cavity [47].Since then, MI has been widely studied [90, 98, 47, 80]. Unlike the "single-pass" configuration of an optical fibre, in an optical resonator the geometry of the

system provides another degree of freedom in the phase matching process [46, 90], represented by linear phase detuning. Recently, it has been shown that the inclusion of spectrally localised losses is a counterintuitive mechanism that can lead to MI gain [58, 59]. In the context of optical fibre cavities, narrow filters can induce a modification of the phase matching condition of the resonator, resulting in the formation of MI spectra [60, 61]. Part of this work will be dedicated to the characterisation of the GTF phenomenon in fibre ring cavities, and we will start this analysis from a theoretical description of the phenomenon.

2.1 Theory of Modulation Instability

In this section we will describe the stability analysis for the Ikeda map [67] and the LLE [68]. The result of this analysis will be the calculation of the growth rate of a given frequency during its propagation, which we will refer to as *parametric gain*.

2.1.1 Linear stability analysis of Ikeda Map

We begin by describing the stability analysis of the Ikeda map. For the sake of clarity, we assume that the losses of the cavity are combined in the factor ρ which is linked to the finesse with $\mathcal{F} = \pi\sqrt{\rho}/(1-\rho)$. Equation (1.7) takes the form:

$$\begin{cases} i\dfrac{\partial E_n(z,\tau)}{\partial z} - \dfrac{\beta_2}{2}\dfrac{\partial^2 E_n(z,\tau)}{\partial \tau^2} + \gamma|E_n(z,\tau)|^2 E_n(z,\tau) = 0,\ 0 < z < L \\ E_{n+1}(z=0,\tau) = \theta E_{in} + \rho e^{i\phi_0} E_n(z=L,\tau) \end{cases} \tag{2.1}$$

The CW reads as:

$$E_n(z,\tau) = \bar{E}e^{i\gamma P z},\ P = |\bar{E}|^2.$$

As shown in the previous chapter, the complex field and power steady states, can be written as:

$$\bar{E} = \frac{\theta}{1-\rho e^{i\phi}} E_{in}, \tag{2.2}$$

$$P = \frac{\theta^2}{1+\rho^2-2\rho\cos(\phi)} P_{in}. \tag{2.3}$$

with $\phi = \phi_0 + \gamma PL$. To study the stability of the steady state, we consider the following perturbation:

$$E_n(z,\tau) = [\sqrt{P} + \eta_n(z,t)]e^{i\gamma Pz},\ |\eta_n| \ll \sqrt{P}. \tag{2.4}$$

We can assume that the intracavity field is real, since the steady state phase does not affect the solution of the system in this case. By linearising the NLSE Eq.(2.1) with respect to the small perturbation, we obtain

$$i\frac{\partial \eta_n}{\partial z} - \frac{\beta_2}{2}\frac{\partial^2 \eta_n}{\partial \tau^2} + P\gamma(\eta_n + \eta_n^*) = 0.$$

This equation describes the evolution of the perturbation in z. Now we can write the perturbation explicitly as $\eta_n = a_n + ib_n\,(a_n, b_n \in \mathbb{R})$. Since we are interested in the spectra of the perturbation, we define $\hat{a_n} = \hat{a_n}(z,\omega)$, $\hat{b_n} = \hat{b_n}(z,\omega)$ (where the symbol $\hat{}$ represents the Fourier transform), and split the real and imaginary parts in the following system

$$\begin{cases} \frac{\partial \hat{a_n}}{\partial z} = -\frac{\beta_2}{2}\omega^2 \hat{b_n}, \\ \frac{\partial \hat{b_n}}{\partial z} = \left(\frac{\beta_2}{2}\omega^2 + 2\gamma P\right)\hat{a_n}. \end{cases} \tag{2.5}$$

The solution over a roundtrip, thus from $z = 0$ to $z = L$, can be found by calculating the matrix exponential relative to the system, and it reads:

$$\begin{pmatrix} \hat{a}_n(L) \\ \hat{b}_n(L) \end{pmatrix} = \begin{pmatrix} \cos(KL) & -\frac{\beta_2\omega^2}{2K}\sin(KL) \\ -\frac{2K}{\beta_2\omega^2}\sin(KL) & \cos(KL) \end{pmatrix} \begin{pmatrix} \hat{a}_n(0) \\ \hat{b}_n(0) \end{pmatrix}, \tag{2.6}$$

with $K(\omega) = \sqrt{\frac{\beta_2\omega^2}{2}(\frac{\beta_2\omega^2}{2} + 2\gamma P)}$ being the wave number of the perturbation. To complete the analysis one has to consider the boundary condition of the cavity. In particular, by plugging the perturbed steady state equation (2.4) into the boundary condition of the system (2.1) and splitting the real and imaginary

parts in the frequency domain, we obtain:

$$\begin{pmatrix}\hat{a}_{n+1}(0)\\ \hat{b}_{n+1}(0)\end{pmatrix} = \rho\begin{pmatrix}\cos(\phi) & -\sin(\phi)\\ \sin(\phi) & \cos(\phi)\end{pmatrix}\begin{pmatrix}\hat{a}_n(L)\\ \hat{b}_n(L)\end{pmatrix}. \tag{2.7}$$

At this point we have all the elements to describe the perturbation's spectrum. First, the complete system can be written by substituting Eq. (2.6) into Eq.(2.7), which gives:

$$\begin{pmatrix}\hat{a}_{n+1}(0)\\ \hat{b}_{n+1}(0)\end{pmatrix} = \rho\begin{pmatrix}\cos(\phi) & -\sin(\phi)\\ \sin(\phi) & \cos(\phi)\end{pmatrix}\begin{pmatrix}\cos(KL) & -\frac{\beta_2\omega^2}{2K}\sin(KL)\\ -\frac{2K}{\beta_2\omega^2}\sin(KL) & \cos(KL)\end{pmatrix}\begin{pmatrix}\hat{a}_n(L)\\ \hat{b}_n(L)\end{pmatrix}. \tag{2.8}$$

The eigenvalue of the product of the boundary condition and propagation matrix can be written as:

$$\lambda_{1,2} = \frac{\Delta}{2} \pm \sqrt{\frac{\Delta^2}{4} - \rho^2}, \tag{2.9}$$

where $\Delta = \rho[2\cos(\phi)\cos(KL) - \frac{\beta_2\omega^2+2\gamma P}{K}\sin(\phi)\sin(KL)]$. Whenever $|\lambda_{1,2}| > 1$, the CW solution of the system Eq. (2.2) is unstable, and the perturbation grow exponentially as $\exp(g_{MAP}(\omega)z)$, where the MI gain is defined as:

$$g_{MAP}(\omega) = \frac{2}{L}\ln\max\{|\lambda_1|,|\lambda_2|\}. \tag{2.10}$$

It is possible to verify that the gain is positive for $|\Delta| > 1 + \rho^2$. In the good cavity limit ($\rho \simeq 1$), threshold becomes $|\Delta| = 2$, and at moderate powers we also have that $\frac{\beta_2\omega^2+2\gamma P}{K} \simeq 2$. Under those assumption, we find that the most unstable frequencies satisfy the following condition:

$$K + \frac{\gamma PL + \phi_0}{L} = m\pi/L,\ m = \pm 0, \pm 1, \pm 2, \ldots. \tag{2.11}$$

The solution for $m = 0$ can be interpreted as a phase matching condition, while $m \neq 0$ describes *parametric resonance* [99], associated to the round-trip periodicity of the system. This stability analysis allows us to understand the conditions under which the system can modulationally unstable. In Fig. (2.1) we propose a series of plots describing $g_{MAP}(\omega)$, from Eq. (2.10), as a function of the intra-

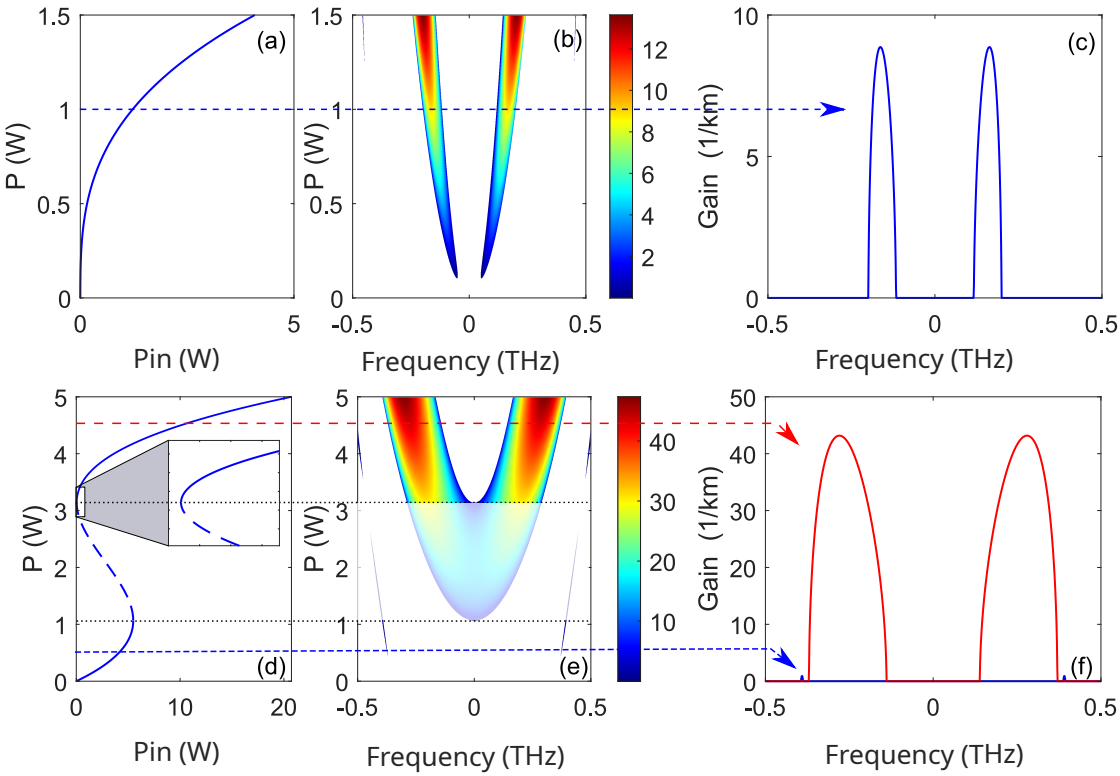

Figure 2.1 – (a) intracavity vs input power for $\phi_0 = 0\,rad$. (b) gain as function of intracavity power, (c) an example of gain for $P = 1\,W$. (d) intracavity vs input power for $\phi_0 = -\pi/4\,rad$, with a zoom on the upper branch switching knee. (e) gain as function of intracavity power, (f) two example of gains: $P = 0.5\,W$ in blue, parametric instability, $P = 4.5\,W$. The parameters used in the calculations are: $\beta_2 = -19\,ps^2/km$, $\gamma = 5\,/W/m$, $L = 50\,m$, $\rho = \sqrt{0.95}$, $\theta = \sqrt{0.05}$.

cavity power P in the case of anomalous dispersion ($\beta_2 < 0$). In particular, Fig. (2.1) (b) and (c) show the gain and a snapshot for $P = 1\,W$, respectively. In Fig. (2.1) (a) we have plotted the steady state relation $P = f(P_{in})$. Since $\phi_0 = 0\,rad$, the function doesn't show a negatively sloped branch at such low power, so the system is monostable.

By analysing the gain we can see a pair of bands growing and moving outward respect to the pump as the power increases. At higher powers, around $P_{in} = 1.3$ W, it's also possible to spot two very thin additional bands. Those are referred to as *parametric* gain bands, and they can be interpreted as solution for $m \neq 0$ of Eq. (2.11).

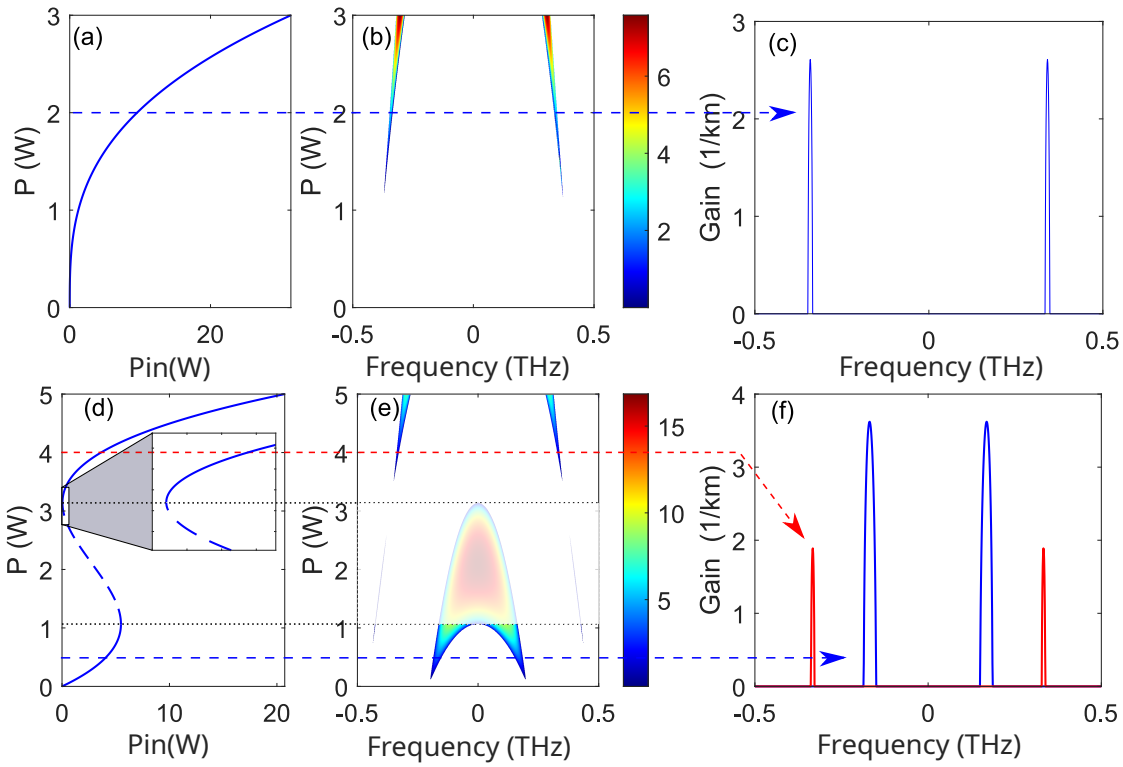

Figure 2.2 – (a) intracavity vs input power for $\phi_0 = 0\,rad$. (b) gain as function of intracavity power, (c) an example of gain for $P = 2\,W$. (d) intracavity vs input power for $\phi_0 = -\pi/4\,rad$, and a zoom on the upper switching knee. (e) gain as function of intracavity power, (f) two example of gains: $P = 0.5\,W$ in blue, $P = 4\,W$ in red. The parameters used in the calculations are: $\beta_2 = 19\,ps^2/km$, $\gamma = 5/W/m$, $L = 50\,m$, $\rho = \sqrt{0.95}$, $\theta = \sqrt{0.05}$.

In Fig. 2.1 (e) and (f) we have plotted the same function as in the panels above, but with the cavity in a bistable regime $\phi_0 = -\pi/4\,rad$. In particular, we can see in Fig. 2.1 (d) that the steady state relation acquires a negatively sloped branch. In chap 1.2.3 we discussed why such branches contain unstable solutions, and by looking at the gain it's immediately clear why. Indeed, by considering at the shaded area in Fig. 2.1 (e), which corresponds to the negatively sloped branch in Fig. 2.1 (d), we can see how the gain positive for $f = 0\,THz$, which is the frequency of the pump. On the contrary, on both the lower and upper branches of the S-shaped curve, the MI gain band does not includes the zero frequency.

In Fig. (2.2) we have done the same analysis but with a normally dispersive fibre ($\beta_2 > 0$). This time, as shown in Fig. (2.2) (b). We also propose an example in the bistable regime, the panels (d), (e), (f) of the same figure. In particular, we can see that the system can sustain MI bands in the lower branch as well as in the upper branch of the bistable curve. All parameters are listed in the figure captions.

2.1.2 Linear stability analysis of LLE

The LLE model reads as follows:

$$L\frac{\partial E}{\partial z} = (-\alpha + i\phi_0)E - i\frac{\beta_2 L}{2}\frac{\partial^2 E}{\partial \tau^2} + iL\gamma|E|^2E + \theta\sqrt{P_{in}}. \tag{2.12}$$

The steady state complex field and power are:

$$\bar{E} = \frac{\theta\sqrt{P_{in}}}{\alpha - i(\phi_0 + L\gamma\bar{P})} \tag{2.13}$$

$$\bar{P} = \frac{\theta^2 P_{in}}{\alpha^2 + (\phi_0 + L\gamma\bar{P})^2} \tag{2.14}$$

The perturbed steady state can be written as:

$$E = E_0 + a(z)e^{i\omega\tau} + b(z)e^{-i\omega\tau},\ E_0 = \sqrt{\bar{P}}e^{i\zeta},\ |a|,|b| \ll |E_0|. \tag{2.15}$$

Similar to what was done for the Ikeda model, one can substitute Eq. (2.15), into Eq. (2.12), and then split the component of the opposite oscillation $\pm\omega$, to get the following system:

$$L\frac{\partial}{\partial z}\begin{pmatrix} a \\ b^* \end{pmatrix} = \begin{pmatrix} -\alpha + i\mu(\omega) & iL\gamma E_0 \\ -iL\gamma E_0^* & -\alpha - i\mu(\omega) \end{pmatrix}\begin{pmatrix} a \\ b^* \end{pmatrix}, \tag{2.16}$$

with $\mu(\omega) = \phi_0 + \beta_2\omega^2 L/2 + 2\gamma L\bar{P}$, which can be interpreted as a phase mismatch parameter. At this point the calculation of the eigenvalue of the matrix in eq.

(2.16) is relatively simple, and it reads

$$\lambda_{\pm} = -\alpha \pm \sqrt{(L\gamma\bar{P})^2 - \mu(\omega)^2}, \tag{2.17}$$

from which the one can define the MI gain as:

$$g_{LLE}(\omega) = 2\frac{\max \Re\mathfrak{e}(\lambda_{\pm})}{L}. \tag{2.18}$$

Whenever $g_{LLE}(\omega) > 0$, the amplitude of the perturbation grows exponentially as $\exp[g_{LLE}(\omega)z]$. One of the advantages of the LLE model is that it's possible to obtain a single expression for of the most unstable frequency and the maximum gain as:

$$\omega_T = \sqrt{\frac{2}{\beta_2}(\frac{\delta_0}{L} - 2\gamma\bar{P})},\ g_{LLE}(\omega_T) = \frac{-\alpha}{L} + \gamma P. \tag{2.19}$$

The cavity will sustain the MI only if $g_{LLE}(\omega) > 0$ and ω_T is real. From those relation one can identify two necessary conditions, depending on the sign of β_2, under which the cavity can sustain MI:

- $\beta_2 < 0 : P > P_{th}, P > P_{\omega}$
- $\beta_2 > 0 : P > P_{th}, P < P_{\omega}$

with $P_{th} = \alpha/L\gamma$ derived from the condition $g_{LLE}(\omega_T) = 0$ and $P_{\omega} = \delta_0/2\gamma L$ derived from the constraint that ω_T must be real. These conditions are not sufficient to define the range in which the system can sustain modulation instability. In fact, it's also necessary that the intracavity power does not fall in the unstable part of the steady state relation. We recall that, thanks to the formulation of the LLE model, we can define the up-switch and down-switch powers as $P_{\pm} = \frac{2\delta_0 \pm \sqrt{\delta_0^2 - 3\alpha^2}}{3\gamma L}$. Any intracavity power between the up and down switch values corresponds to an unstable state.

The chart of instability is drawn in Fig. 2.3, where panel (a) shows the case of anomalous dispersion and (b) the case of normal dispersion. The x-axes of the figure represent the normalised phase detuning (δ_0/α) and the y-axes the intracavity power. For both the anomalous and normal dispersion cases, the

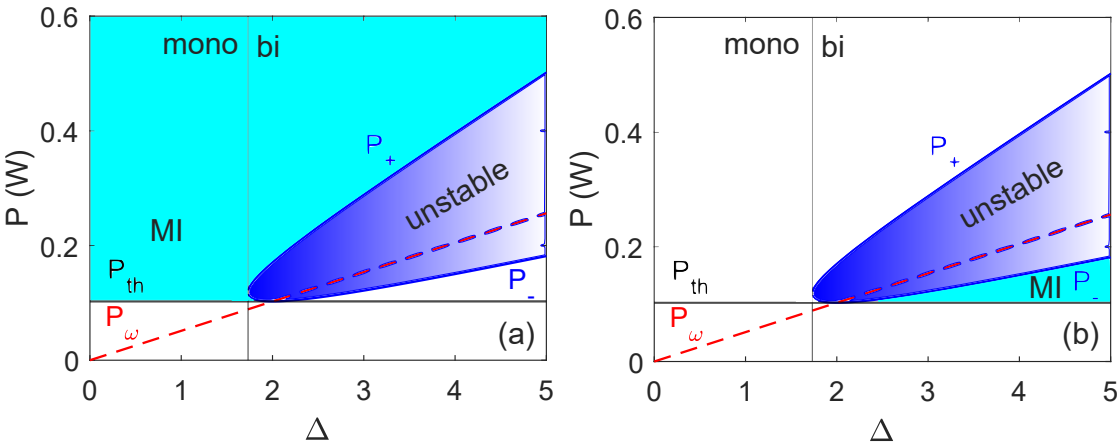

Figure 2.3 – Instability chart for the LLE model. (a) the anomalous dispersion regime, (b) normal dispersion regimes. The parameters used for the computation are: $L = 50\,m$, $\beta_2 = \pm 19 ps^2/m$, $\gamma = 5/W/m$, $\rho = \sqrt{0.95}$ and $\alpha = 1 - \rho$.

blue curves represent $P_{\pm}$, which delimits the region in the (P, Δ) plane where the homogeneous steady state of the cavity is unstable. The vertical line at $\Delta = \sqrt{3}$ is the border between mono and bistability of the cavity. The cyan area in the two figures represent the domain of existence of modulation instability and, for both anomalous and normal dispersion, when the power is below the threshold P_{th}, the system remains stable. In Fig. 2.3 (a) MI is predicted for $P > P_{th}$ and $P > P_{+}$ (cyan area).In the case of the normal dispersion, Fig. 2.3(b), the map shows that MI is only possible if $P_{-} < P < P_{th}$.

These two maps gives a summary of the stability conditions of the cavity, but no information about the spectral characteristic of the MI. Thus, as done for the Ikeda Map model in the previous section, we propose a couple of example of gain maps computed computed with Eq. 2.17, to illustrate the shape of the MI gain in the anomalous and normal dispersion regime.

In Fig. 2.4 (b) we propose the gain for anomalous dispersion ($\beta_2 < 0$), in the monostable regime $\phi_0 = 0\,rad$. In Fig. 2.4 (c), the plot illustrates a snapshot of the gain for $P = 1\,W$, and in Fig. 2.4 (a), the steady state relation between P and P_{in} is illustrated. In Fig. 2.4 (e) we have plotted the same function but in the bistable case $\phi_0 = -\pi/4\,rad$. Again, the shaded area indicates the homogeneous unstable states of the cavity, so MI is only possible when the intracavity power is on the upper stable branch of the curve in Fig. 2.4 (d). An example of the gain

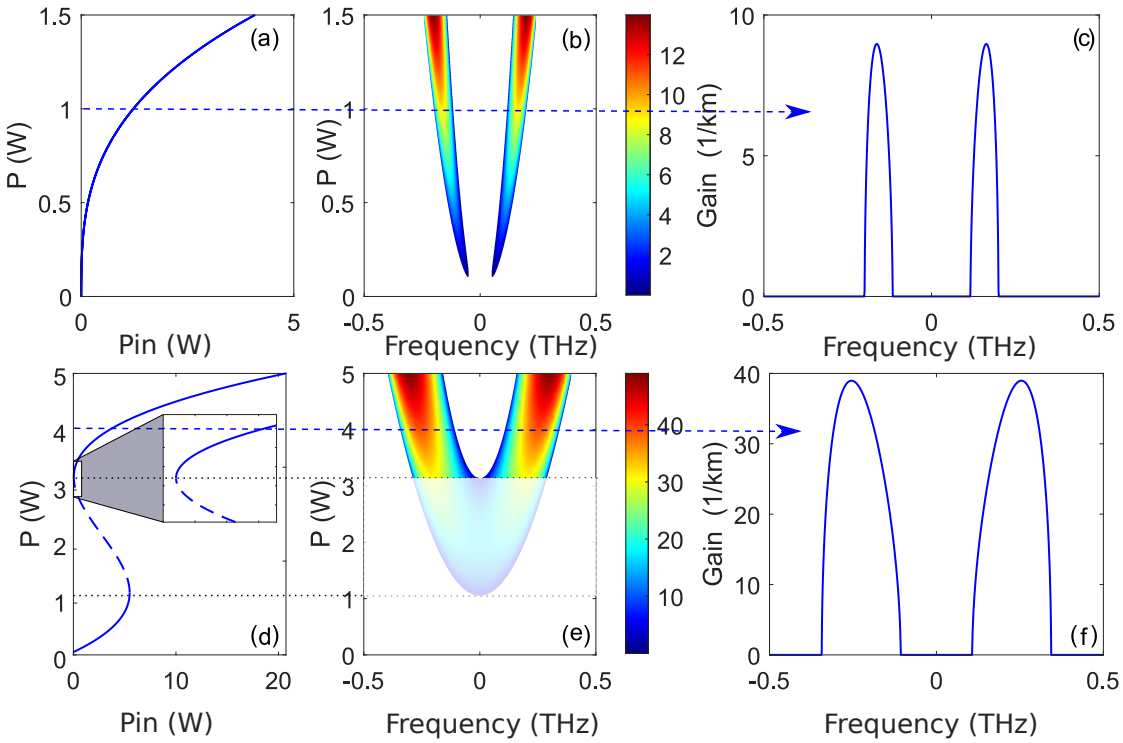

Figure 2.4 – (a) intracavity vs input power for $\phi_0 = 0\,rad$. (b) gain as function of intracavity power, (c) an example of gain for $P = 1\,W$. (d) intracavity vs input power for $\phi_0 = -\pi/4\,rad$, with a zoom on the up switching knee. (e) gain as function of intracavity power, (f) an example of gain: $P = 1\,W$. The parameters used in the calculations are: $\beta_2 = -19\,ps^2/km$, $\gamma = 5\,/W/m$, $L = 50\,m$, $\rho = \sqrt{0.95}$, $\theta = \sqrt{0.05}$.

for $P = 4\,W$ is shown in Fig. 2.4 (e).

Finally, we propose in Fig. 2.5 an example for the normal dispersion case. This time MI is destabilized only in the bistable case, because of the conditions analysed above. In particular, from Fig. 2.5 (b), the gain shows MI only in the lower branch of the bistable curve of Fig 2.5 (a). As can be seen, these results are basically identical to those shown in Figs. 2.1 and 2.2, with the main difference being the absence of parametric instabilities. The Ikeda model, due to its periodic nature, allows the prediction of parametric instabilities that are "lost" in the derivation of the mean-field approximation. On the other hand, the LLE is more compact and can be much faster in terms of numerical integration. For these reasons, in this dissertation we will use either the LLE or the Ikeda

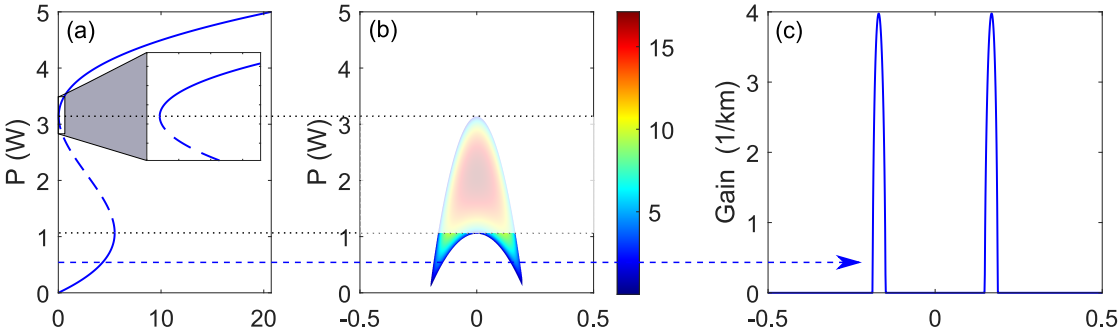

Figure 2.5 – (a) intracavity vs input power for $\phi_0 = -\pi/4\,rad$. (b) gain as function of intracavity power, (c) an example of gain: $P = 0.5\,W$. To note that with this model, the cavity seems to not sustain gain in monostable regime, when normally dispersive. The parameters used in the calculations are: $\beta_2 = 19 ps^2/km$, $\gamma = 5/W/m$, $L = 50\,m$, $\rho = \sqrt{0.95}$, $\theta = \sqrt{0.05}$.

model, depending on the topic we are analysing.

2.2 Gain Through Filtering

In section, we are going to analyse the theory of the Gain-Through-Filtering (GTF) process [60, 61], which consist in the destabilization of MI sidebands given by the presence of unbalanced losses respect a strong pump. We propose here the stability analysis GTF, with the aim of calculating a parametric gain model for both the Ikeda map and the LLE. We also propose an overall analysis of the dependence of the parametric gain on the most common parameters of the filter.

2.2.1 Filter model

Before going into the detailed stability analysis of the process, we present the model of the filter used. In particular, we use a Fibre Bragg Grating (FGB), which is particularly suitable for this application because it can be spliced directly into the cavity with minimal losses. Due to causality, the real and imaginary parts of the transfer function of the filter can be conveniently related by the Kramer-Kronig relations [100]. In particular, KK relates the transfer function

and phase of the filter with the following relation:

$$\psi(\omega) = \mathcal{H}[F(\omega)] = \mathcal{H}[\ln|H(\omega)|], \tag{2.20}$$

where the Hilbert transform is defined as $\mathcal{H}[f(x)] = \frac{1}{\pi}\text{P.V.}\int_{-\infty}^{+\infty}\frac{f(y)dy}{x-t}$, P.V. denoting the principal value of the integral [60]. The transfer function of the filter is defined as

$$H(\omega) = e^{F(\omega)+i\psi(\omega)} = \mathbb{F}[h(t)], \tag{2.21}$$

with $\mathbb{F}$ representing the Fourier transform, and $h(t)$ the impulse response of the filter. In this dissertation, we will consider a higher order Lorentzian to fit the amplitude response of the filter ($F(\omega)$), which allows an analytical formulation of the Hilbert transform for the phase ($\psi(\omega)$), as follow:

$$F(\omega) = b\frac{a^4}{(\omega-\omega_f)^4 + a^4} \tag{2.22}$$

$$\psi(\omega) = ba\frac{(\omega-\omega_f)[(\omega-\omega_f)^2 + a^2]}{\sqrt{(2)}[(\omega-\omega_f)^4 + a^4]} \tag{2.23}$$

with a being related to the bandwidth of the filter, and $b < 0$ being a non-dimensional number which sets the maximum attenuation of the filter. This model is very convenient to use, not only because it provides an analytical description of the filter, but also because it accurately describes the amplitude of the FBG. An example of a fitted filter is shown in Fig. 2.6: (a) reports a plot of the measured (red) and fitted (blue) power loss profile of the filter, and (b) a plot of the phases. As can be seen, the parameters $a = 78\,(rad/ns)$ and $b = -2.35$ allow a very good fit for both amplitude and phase. In the following we will use the description of the filter given by the analytical model of equations 2.22 and 2.23.

2.2.2 Stability analysis with Ikeda map

Having already developed all the calculation for the stability analysis of the Ikeda Map, in this section we will report only the main passages, also reported

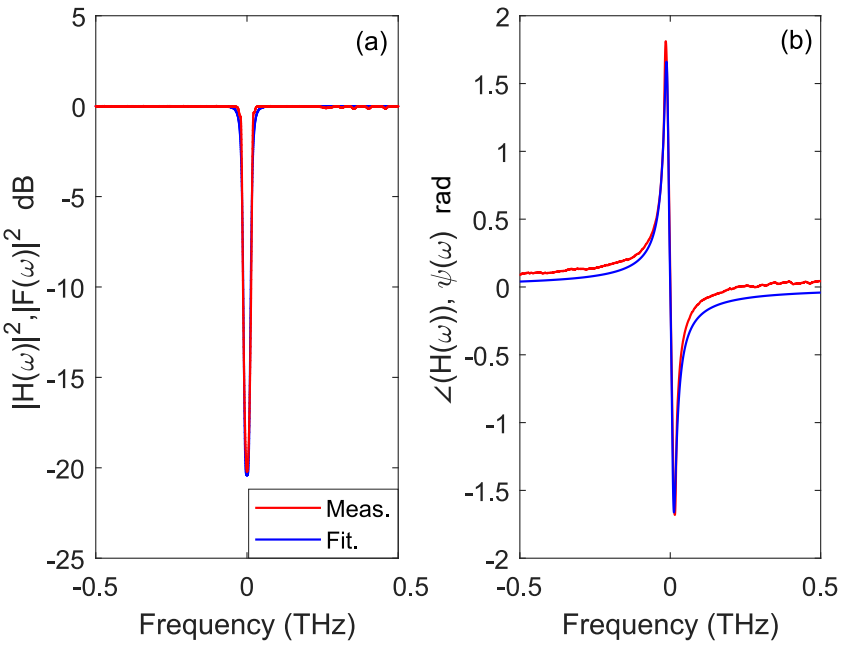

Figure 2.6 – Measured and fitted characteristic of the filter: (a) power attenuation profile; (b) phase profile. The fitting has been done with the model of Eqs. (2.22) and (2.23), with $a = 78\ rad/ns$ and $b = -2.35$.

in [60]. An advantage of using the Ikeda map model is that it is very easy to generalize for studying GTF. Indeed, it's sufficient to rewrite the boundary condition of the map. By assuming that the filter is located just before the coupler ($z = L$), the model reads:

$$\begin{cases} i\dfrac{\partial E_n(z,\tau)}{\partial z} - \dfrac{\beta_2}{2}\dfrac{\partial^2 E_n(z,\tau)}{\partial \tau^2} + \gamma|E_n(z,\tau)|^2 E_n(z,\tau) = 0,\ 0 < z < L \\ E_{n+1}(z=0,\tau) = \theta E_{in} + \rho e^{i\phi_0} h(t) \star E_n(z=L,\tau) \end{cases} \tag{2.24}$$

where $\star$ indicates the convolution operation. Note that the only difference with the Ikeda map of eqs. (2.1) is the presence of the filter in the boundary condition, whose impulsive response is convoluted with the envelope of the signal $E_n(z = L, \tau)$ at the end of the n_{th} round trip.

As before, the first step is to look for the stationary CW field inside the fiber,

that can be found by assuming the solution to take the form

$$E_n(z = L, \tau) = \bar{E} e^{i\gamma z},\ P = |\bar{E}|^2.$$

Given that field formulation, one can obtain the complex field and power of the steady state of the cavity as

$$\bar{E} = \frac{\theta}{1 - \rho e^{i\phi} H(0)} E_{in} \tag{2.25}$$

$$\bar{E} = \frac{\theta^2}{1 + \rho^2 |H(0)|^2 - 2\rho |H(0)| \cos(\phi + \psi(0))} P_{in}, \tag{2.26}$$

where $\phi = \phi_0 + \gamma LP$ is the total power accumulated by the signal inside the cavity, E_{in} and P_{in} are the field and power of the input signal. Note that, compared to the homogeneous cavity steady states in Eqs. (2.2) and (2.3), we have the contribution of the filter amplitude $H(0)$, which acts as an additive loss, and its phase $\psi(0)$ as an additive phase shift. The stability of the steady states is done in exactly the same way as before. We assume a small perturbation superimposed on the field as:

$$E_n(z, t) = [\sqrt{P} + \eta_n(z, t)] e^{i\gamma P z},\ |\eta_n| \ll \sqrt{P}$$

The description of the propagation of the pulse inside the fibre of the cavity, from $z = 0$ to $z = L$, can be done by again linearising the system and calculating the matrix exponent for $z = L$. The result is:

$$\begin{pmatrix} \hat{a}_n(L) \\ \hat{b}_n(L) \end{pmatrix} = \begin{pmatrix} \cos(KL) & -\frac{\beta_2 \omega^2}{2K} \sin(KL) \\ -\frac{2K}{\beta_2 \omega^2} \sin(KL) & \cos(KL) \end{pmatrix} \begin{pmatrix} \hat{a}_n(0) \\ \hat{b}_n(0) \end{pmatrix}, \tag{2.27}$$

The difference is in the boundary condition matrix. In particular, the effect of the filter and coupler on the perturbation (in the frequency domain) can be described as follows:

$$\begin{pmatrix} \hat{a}_{n+1}(0) \\ \hat{b}_{n+1}(0) \end{pmatrix} = \rho \begin{pmatrix} \cos(\phi) & -\sin(\phi) \\ \sin(\phi) & \cos(\phi) \end{pmatrix} \begin{pmatrix} H_e(\omega) & -H_o(\omega) \\ H_o(\omega) & H_e(\omega) \end{pmatrix} \begin{pmatrix} \hat{a}_n(L) \\ \hat{b}_n(L) \end{pmatrix}. \tag{2.28}$$

where the even and odd part of the filter are defined as:

$$H_e(\omega) = \mathcal{F}\{\Re\mathfrak{e}[h(t)]\} = \frac{H(\omega) + H^*(-\omega)}{2},$$

$$H_o(\omega) = \mathcal{F}\{\mathrm{Im}[h(t)]\} = \frac{H(\omega) - H^*(-\omega)}{2i}.$$

At this point, by combining the matrices (2.27) and (2.28), we get the total evolution of the perturbation inside the fibre, the filter and the coupler as:

$$\begin{pmatrix} \hat{a}_n(L) \\ \hat{b}_n(L) \end{pmatrix} = \rho \begin{pmatrix} \cos(KL) & -\frac{\beta_2\omega^2}{2K}\sin(KL) \\ -\frac{2K}{\beta_2\omega^2}\sin(KL) & \cos(KL) \end{pmatrix} \mathrm{x} \begin{pmatrix} \cos(\phi) & -\sin(\phi) \\ \sin(\phi) & \cos(\phi) \end{pmatrix} \begin{pmatrix} H_e(\omega) & -H_o(\omega) \\ H_o(\omega) & H_e(\omega) \end{pmatrix} \begin{pmatrix} \hat{a}_n(0) \\ \hat{b}_n(0) \end{pmatrix}, \quad (2.29)$$

Despite its cumbersome description, the total matrix formulation is actually quite convenient because it isolates the three main elements: the propagation in the fibre, the boundary conditions and the filter. It follows that these three elements can be easily modified in the event of a change in the system, such as multiple fibres or different types of filter. The eigenvalues of total matrix reads as

$$\lambda_{1,2} = \frac{\Delta}{2} \pm \sqrt{\frac{\Delta^2}{4} - W}, \quad (2.30)$$

where

$$W = \rho^2(H_e(\omega)^2 + H_o(\omega)^2),$$
$$\Delta = \rho\Big[2\cos(KL)(H_e(\omega)\cos(\phi) - H_o(\omega)\sin(\phi)) - \frac{\beta_2\omega^2 + 2\gamma P}{K}\sin(KL)(H_o(\omega)\cos(\phi) + H_e(\omega)\sin(\phi))\Big] \quad (2.31)$$

When $|\lambda_{1,2}| > 1$, the perturbation power grows as $\exp[g_{MAP}(\omega)z]$, so the MI gain can be defined as:

$$g_{MAP}(\omega) = \frac{2}{L}\ln\max|\lambda_1|,|\lambda_1|. \quad (2.32)$$

2.2.3 Stability analysis with LLE

A generalised Lugiato-Lefever model that describe the propagation in a cavity including a filter has been derived in [60]:

$$L\frac{\partial E}{\partial z} = [-\alpha + i\phi_0 + \Phi\star + i\Psi\star]E - \frac{iL\beta_2}{2}\frac{\partial^2 E}{\partial \tau^2} + iL\gamma|E|^2E + \theta\sqrt{P_{in}}. \tag{2.33}$$

The only differences with respect to the LLE, are the filters terms $\Phi(t) = \mathcal{F}^{-1}[F(\omega)]$ and $\Psi(t) = \mathcal{F}^{-1}[\psi(\omega)]$.

The steady states relation for complex field and power with:

$$\bar{E} = \frac{\theta\sqrt{P_{in}}}{\alpha - \Phi - i(\phi_0 + \gamma LP + \Psi\star)}, \tag{2.34}$$

$$\bar{P} = \frac{\theta^2 P_{in}}{(-\alpha + F(0))^2 + (\phi_0 + L\gamma\bar{P} + \psi(0))^2}. \tag{2.35}$$

The stability analysis is performed by considering the following perturbed state:

$$E(z,t) = E_0 + a(z)e^{-i\omega\tau} + b(z)e^{i\omega\tau},\ E_0 = \sqrt{\bar{P}}e^{i\zeta},\ |a,b| \ll |E_0| \tag{2.36}$$

where a, b is the amplitude of the small disturbances oscillating at $\mp\omega$ and ζ is the phase of the steady state. In order to better highlight the role of the filter, we have decomposed the loss profile and the phase function into their even and odd parts:

$$\begin{aligned} F_e(\omega) &= \frac{F(\omega) + F(-\omega)}{2}, \\ F_o(\omega) &= \frac{F(\omega) - F(-\omega)}{2}, \end{aligned} \tag{2.37}$$

$$\begin{aligned} \psi_e(\omega) &= \frac{\psi(\omega) + \psi(-\omega)}{2}, \\ \psi_o(\omega) &= \frac{\psi(\omega) - \psi(-\omega)}{2}. \end{aligned} \tag{2.38}$$

At this point, linearizing with respect to the small perturbation brings to the

following system (we omitted the dependency from ω for a better readability):

$$L\frac{\partial}{\partial z}\begin{pmatrix} a \\ b^* \end{pmatrix} = \begin{pmatrix} -\alpha + F_e + i\psi_o + i\mu + F_o & iE_0^2 L\gamma \\ -iE_0^2 L\gamma & -\alpha + F_e + i\psi_o - i\mu - F_o \end{pmatrix}\begin{pmatrix} a \\ b^* \end{pmatrix}, \tag{2.39}$$

with

$$\mu(\omega) = \phi_0 + \psi_e(\omega) + L\frac{\beta_2}{2}\omega^2 + 2\gamma LP \tag{2.40}$$

being a phase mismatch parameter. The eigenvalue of the system reads:

$$\lambda_{\pm} = -\alpha + F_e + i\psi_o \pm \sqrt{(\bar{P}\gamma L)^2 - (\mu(\omega) - iF_o)^2}, \tag{2.41}$$

from which we can define the gain as:

$$g_{LLE}(\omega) = 2\frac{\mathfrak{Re}(\lambda_+)}{L}. \tag{2.42}$$

Whenever $g_{LLE}(\omega) > 0$, the power of perturbation grows exponentially as $\exp[g_{LLE}(\omega)z]$.

2.2.4 Approximation of the Phase matching relation

In order to better understand the physical interpretation of the process, it's possible to derive an approximate phase-matching relation, valid when the MI process is mainly driven by the phase of the filter [60]. In Fig. 2.7 (a) we report a plot of the parametric gain, computed with the Ikeda model Eq. (2.30), for three different filters: a filter described by Eq. (2.21) in blue, a filter without the phase term in red, and a filter with unitary modulus in black. The exact parametric gain is the one given by the description of the "full" filter of Eq. (2.21), while the other two are only approximations.

Looking at Fig. 2.7 we can see that the gain obtained with the filter with no phase contribution, red trace, is always negative. In other words, it doesn't predict the amplification of any frequency. On the contrary, the gain relative to the filter with unitary modulus, even if it overestimate the real value, predict the formation of gain bands basically in the same position of the real model. Therefore, to approximate a phase matching relation, we can consider a filter

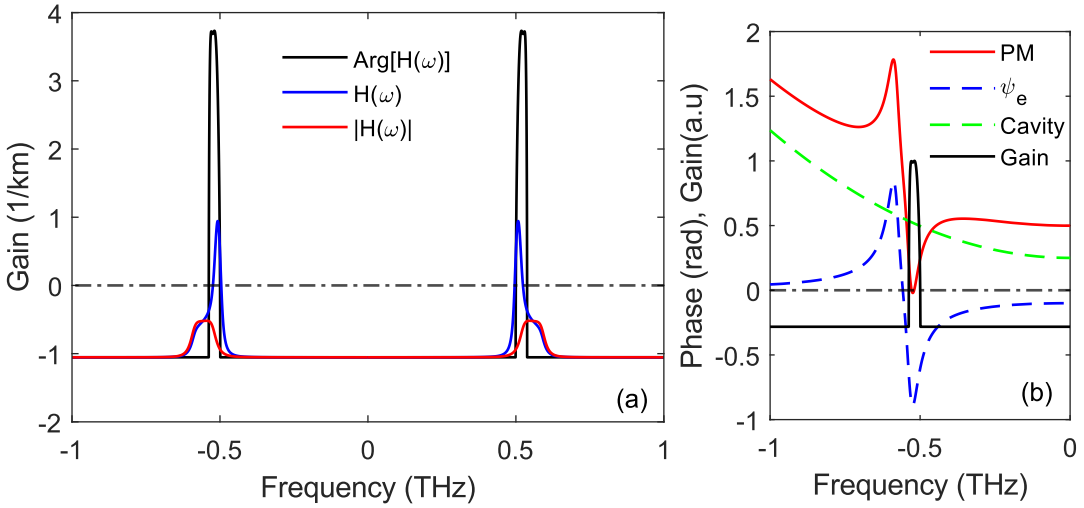

Figure 2.7 – (a) Example of the gain computed with Eq. (2.30) withe three different filter models: the blue trace has complete the filter of Eq. (2.21). For the red trace, the filter does not have the phase contribution; For the black trace, the filter has unitary modulus. (b) Plot phase matching of the phase matching function and its components: green trace is the contribution of the cavity, the blue trace is the even part of the phase of the filter, red trace is the total phase matching function and in black is the gain, normalized to its maximum value. The parameters are : $a = 200\,(rad/ns)$, $b = -2.45$, $L = 100\,m$, $\beta_2 = 0.5\,ps^2/m$, $\gamma = 2.5/W/Km$, $\rho = \sqrt{0.9}$, $\theta = \sqrt{0.1}$, $\phi_0 = 0\,rad$, $\omega_f = 193.48\text{x}2\pi\,(THz)$, $\lambda_p = 1545\,(nm)$.

with a unitary modulus, which allows us to simplify the calculation. In particular, by considering a filter as

$$H(\omega) = \exp i\psi(\omega) \tag{2.43}$$

the even and odd part of $H(\omega)$ becomes:

$$\begin{aligned} H_e(\omega) &= e^{i\psi_o(\omega)}\cos[\psi_e(\omega)], \\ H_o(\omega) &= e^{i\psi_o(\omega)}\sin[\psi_e(\omega)], \end{aligned} \tag{2.44}$$

where $\psi_{e,o}$ are defined in Eq.(2.38). That assumption allows to simplify the

Eqs.(2.31) as follows:

$$\begin{aligned} W =& \rho^2 e^{i2\psi_o}, \\ \Delta =& \rho e^{i\psi_o}\left[2\cos(kL)\cos(\phi+\psi_e) - \frac{\beta_2\omega^2+2\gamma P}{k}\sin(kL)\sin(\phi+\psi_e)\right] \triangleq e^{i\psi_o}\tilde{\Delta} \end{aligned} \tag{2.45}$$

that if one substitute in the eigenvalue formula Eq. (2.30), reads:

$$\lambda_{1,2} = e^{i\psi_o}\left[\frac{\tilde{\Delta}}{2} \pm \sqrt{\frac{\tilde{\Delta}^2}{4} - \rho^2}\right]. \tag{2.46}$$

Apart from the exponential term, the eigenvalue is identical to that obtained for the standard cavity equation (2.9). As for the filter-less case, we have that the instability is reached when $|\tilde{\Delta}| > 1 + \rho^2$ (note that the exponential factor doesn't modify the modulus of $\lambda_{1,2}$, so it has no effect on the gain). By expanding the wavenumber $k(\omega) = \sqrt{\frac{\beta_2\omega^2}{2}\left(\frac{\beta_2\omega^2}{2} + 2\gamma P\right)} \approx \frac{\beta_2\omega^2}{2} + \gamma P$, we obtain:

$$\tilde{\Delta} \approx 2\rho\cos[kL + \psi_e(\omega + \Phi)]. \tag{2.47}$$

The unstable frequencies that maximise $|\tilde{\Delta}|$, satisfy the following conditions:

$$k(\omega)L + \Phi + \psi_e(\omega) = m\pi \; m = 0, \pm 1, \ldots \tag{2.48}$$

Solutions for $m \neq 0$ corresponds to parametric resonances, as shown in the standard case [99]. The solution for $m = 0$, can be considered as the simple phase matching relation:

$$\frac{\beta_2\omega^2}{2}L + 2\gamma PL + \phi + \psi_e(\omega) = m\pi \; m = 0, \pm 1, \ldots \tag{2.49}$$

which, is identical to the phase mismatch term of the LLE Eqs. (2.40), and apart from the ψ_e term, is the same relation found in the standard cavity analysis [99].

The physical interpretation of GTF is quite simple at this point. Parametric amplification is achieved when the phase acquired by the perturbation during

propagation ($\frac{\beta_2\omega^2}{2}L+\gamma PL$), plus the total phase shift of the cavity ($\phi_0+\gamma PL$), plus the even part of the phase of the filter ($\psi_e(\omega)$) is equal to zero. This means that the filters represent an additional degree of freedom for triggering the MI process in cavities. We show an example in Fig. 2.7(b): in this graph we summarise the element of the phase matching condition, isolated by contribution. The green dashed lines are the contribution of the cavity with dispersion, non-linearity and linear phase detuning ($\frac{\beta_2\omega^2}{2}L+\phi_0+2\gamma PL$). Since in this case $\phi_0 = 0 rad$ and $\beta_2 > 0$, the cavity itself does not fulfil the conditions for modulation instability. The blue dashed line is the even part of the phase of the filter $\psi_e(\omega)$, and it is possible to see the characteristic shape of the phase at the frequency of the filter. By adding this contribution to the other parameter of the phase matching condition, we can see how the total phase matching reaches zero, in red, and gives rise to the parametric gain, in black. This is only an approximate formulation, but it gives a good physical interpretation of the phenomenon and relates to a gain that is reasonably close to the real case. It's important to note that the maximum gain does not coincide with the Bragg wavelength of the FBG. Looking at the phase matching if Fig. 2.7 (b), it is quite clear how the main contribution is given by the peaks of the phase function that lie to the sides of the Bragg frequency.

2.2.5 GTF Characterization

We now proceed to illustrate some of the characteristics and differences between the Ikeda map and LLE models, by studying the parametric gain as a function of several important parameters, focusing mainly on the filter parameters. Firstly, we illustrate the gain as a function of the input power, the depth of the loss and the width of the filter. For the depth and width, we use the b and a parameters described in the previous section.

In Fig. 2.8 we propose a comparison between the parametric gains computed with the Ikeda Map model and the LLE model. In Fig. 2.8 (a) and (b) we have plotted the gain as a function of input power for the Ikeda and LLE models, respectively. To give a better insight, in Fig. 2.8 (c) we have plotted an example of the gain at $P_{in} = 1\ W$ in blue (LLE) and red (Ikeda). The black dashed line, here and in all other plots, represents the central frequency of the filter. In both

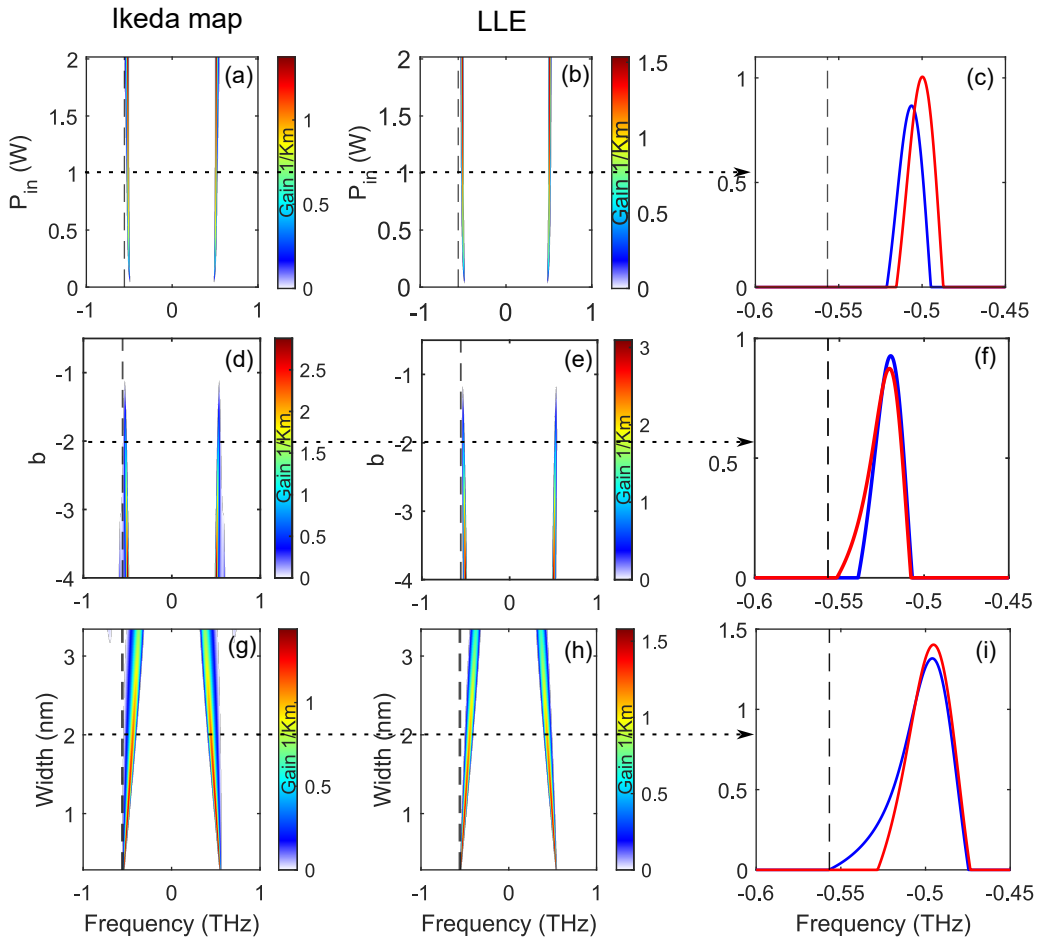

Figure 2.8 – Comparison between Ikeda and LLE parametric gain for different filter parameters: (a)-(b) is a plot as a function of P_{in}, (c) an example at $P_{in} = 1\ W$, red for Ikeda and blue for LLE (same color code in the following panels). (d)-(e) are plots as a function of loss depth b, (f) an example at $b = -2$. (g)-(h) is a plot as a function of width $a\,(rad/ns)$, (i) an example at $a = 2\,(rad/ns)$. The parameter used are: $\lambda_p = 1545\,(nm)$, $\omega_f = 193.48\,(THz)$, $L = 100\,(m)$, $\beta_2 = 0.5\,(ps^2/m)$, $\gamma = 2.5/W/m$, $\phi_0 = 0\,rad$, $\rho = \sqrt{0.9}$, $\theta = \sqrt{0.1}$, $\alpha = 1 - \rho$.

plots (a) and (b) the gain increases with power and the main gain bands rise close to the central frequency of the filter. In Fig. 2.8(c) we can see that there is a small difference in the maximum value of the two models, as well as in the position. Indeed the LLE is derived with a number of approximations, which can lead to small differences in the gain characteristics. In any case, the two description are basically identical.

In Fig. 2.8(d) and (e) we have plotted the gain for Ikeda and LLE by varying the b parameters of the filter, which control the maximum depth of the loss profile. The more negative the value of b, the greater the loss at the centre frequency of the filter ω_f. In the plot we can see that stronger losses are associated with stronger gain intensities, and this can be explained by knowing the relationship between the loss profile and the phase. As described in the section 2.2.1, phase and loss profile are related by KK relations. The greater the losses, the greater the phase detuning imposed by the filter. In the previous section we showed how the gain is mainly based on the even part of the phase of the filters, so that a stronger phase profile translates into a higher gain intensity. In the plot of Fig. 2.8 (f), we compare together two gains for the Ikeda, red, and LLE, blue, for $b = -2$, and again there is a small difference in intensity, but the two parametric gain profiles are equivalent.

Finally, in Figs. 2.8(g) and (h), we propose the plot of the parametric gain of the Ikeda and LLE models as a function of the width of the filter, modelled by the control parameter a. First of all, in both plots it is possible to see a shift in the unstable frequency. This is due to the fact that increasing the width of the filter changes the phase matching frequency. By looking at the 2D Map of Figs. 2.8(g), we can see that at higher "a" correspond the maximum gain becomes lower (see the color bar) at a fixed power. Finally in Fig. 2.8(i) the gain calculated with the two models is basically the same, except for a little difference in the maximum of the gain.

Another important parameter to analyse is the relative frequency shift between the pump and the the filter. Indeed, one of the main points of interest of GTF is that the position of the unstable band can be easily tuned by changing the frequency difference between the pump and filter [61]. The gain maps related to this behaviour are plotted in figure 2.9 (a) and (f) for Ikeda and LLE respectively. On the y-axis we report the difference between the wavelength of the filter λ_f and the wavelength of the pump λ_p, defined as $\Delta_\lambda = \lambda_f - \lambda_p\,(nm)$, while on x-axis we report the frequencies. The black dashed line shows the frequency shift between the pump and the filter for any given Δ_λ.

The first main feature we can describe is the peculiar X shape developed from the parametric gains for both Figs. 2.9 (a) and (f). This shape is given

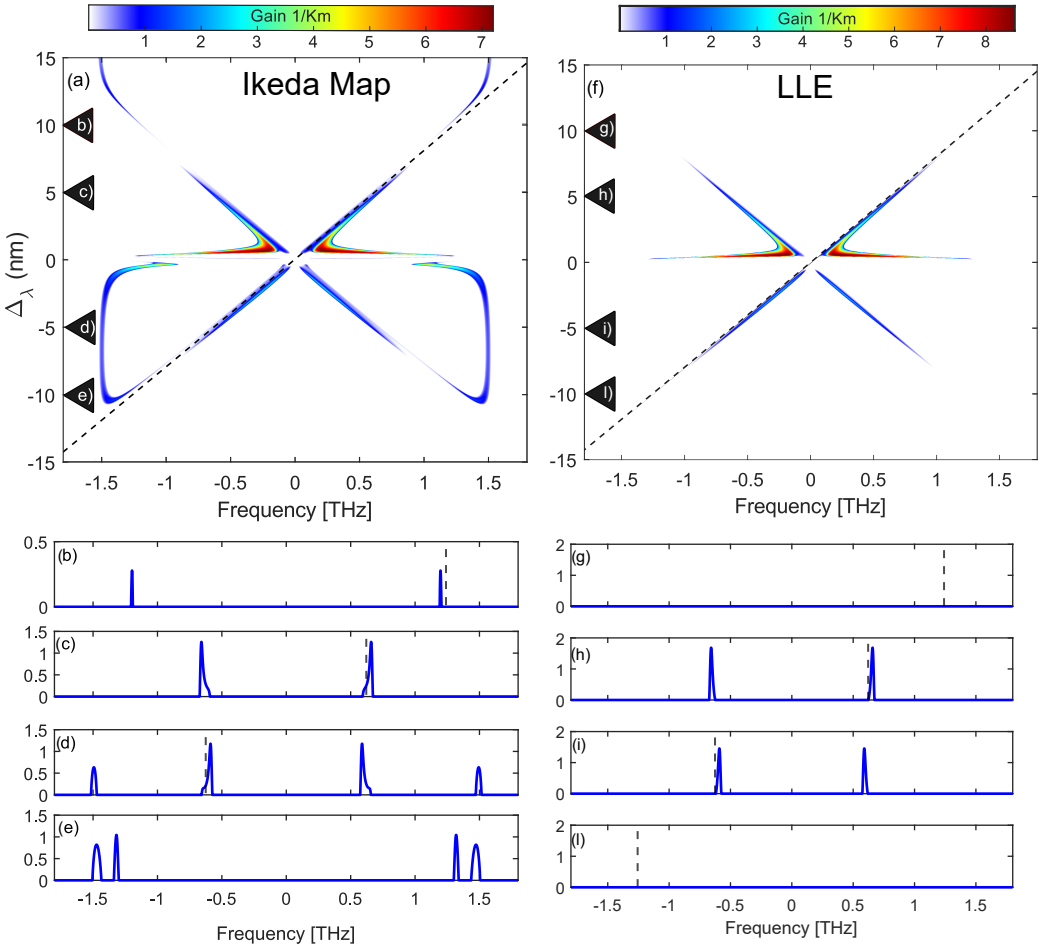

Figure 2.9 – Comparison between Ikeda and LLE parametric gain as functions of the $\Delta_\lambda = \lambda_f - \lambda_p$. (b)-(e) are four example at $\Delta_\lambda = [10, 5, -5, -10]\,(nm)$ for Ikeda Map model, respectively. (g)-(l) are four example at $\Delta_\lambda = [10, 5, -5, -10]\,(nm)$ for LLE model, respectively. The diagonal black dashed line represent the position of the central wavelength of the filter λ_f respect to the pump. The parameter used are: $\lambda_p = 1545\,(nm)$, $\omega_f = 193.48\,(THz)$, $L = 100\,(m)$, $\beta_2 = 0.5\,(ps^2/m)$, $\gamma = 2.5/W/m$, $\phi_0 = 0\,rad$, $\rho = \sqrt{0.9}$, $\theta = \sqrt{0.1}$, $\alpha = 1 - \rho$, $P_{in} = 5\,W$.

by the GTF gain bands whose position changes according to the Δ_λ shift. The closer the pump and filter are, the closer the bands are to the pump. The gain also becomes more intense as the bands get closer to the pump on the positive Δ_λ interval. This is because in this case the P_{in} is kept constant while the intracavity power P is free to change. The closer the filter and pump are, the more important the effect of the phase of the filter. This strongly changes

the intracavity power, which consequently changes the amplitude of the gain. To better illustrate the phenomenon, we have plotted four examples extracted for $\Delta_\lambda = [10, 5, -5, -10]\, nm$ (see corresponding arrows) in Figs. 2.9 (b)-(e) for the Ikeda model and (g)-(i) for the LLE.

The Ikeda map plots show some additional bands whose position remains fixed in the Δ_λ interval analysed, particularly visible in the negative interval plots (d) and (e). These bands can be interpreted as *parametric* instabilities that we have already encountered in the section 2.1.1.

Despite the nature of those bands is not linked to filter, but only due to the cavity itself, their amplitude changes with Δ_λ, and they actually completely vanish in the interval $\Delta_\lambda = [0, 10]\,(nm)$. This is due to the influence of the phase of the filter, which is not symmetric respect λ_f, thus modify the dispersion relation differently on $\Delta_\lambda > 0$ or $\Delta_\lambda < 0$.

As show in Fig. 2.9 (f) the LLE does not predicts parametric gain bands. This because the periodicity of the system, which is the physical cause of these parametric instabilities, is lost during the derivation of the model.In Figs. 2.9 (g)-(l) we show four examples at the same Δ_λ as the Ikeda map example: in particular, (h) and (i) show GTF bands, but (g) and (l) don't show any kind of parametric gain. The absence of the parametric bands is the biggest difference between the Ikeda map and LLE models.

2.3 Summary

- In the first part of this chapter, we described the general characteristic of MI in a uniform cavity with the most common models: Ikeda Map and LLE. We summarized the condition of instability, and highlighted the analogy and differences between the two models.

- We introduced the GTF phenomenon as trigger for MI. We performed the stability analysis, again for both Ikeda and LLE model, in order to get a compact description for the gain. We compared the parametric gain for the two models under various filter's parameters. The main difference between the two models, already encountered in the uniform cavity case, is that the

Ikeda Map allows to predict parametric instability, whose nature is linked to the periodicity of the system.

Chapter 3

Coexistence between GTF and parametric MI

The analysis of the parametric gain done in the previous chapter, suggest that a fiber cavity can sustain different kind of instability at the same time. In particular, there exists some situations in which bot GTF and parametric instability are predicted by the Ikeda map gain. The goal of this chapter is to theoretically and experimentally analyse the relation between this two kind of instability, and characterize their coexistence. In particular, the first part of this chapter is dedicated to the experimental setup, with a brief focus on the Pound-Drever-Hall (PDH) stabilization technique used. In the second part of this chapter, we will show the characterization of coexistence between GTF and parametric instability in a normal and anomalous dispersive cavity, analysing the evolution of the phenomenon as function ϕ_0 and P_{in}.

3.1 Experimental Setup

The experimental setup must meet two requirements: first, it must generate a strong pulsed signal synchronised with the cavity. Secondly, it must keep the cavity stable, with the possibility of determining the linear phase detuning, which is very important in our case of study. These constraints where firstly met by Coen *et.al.* [47, 80, 43, 48], when they first proposed a feedback stabilized

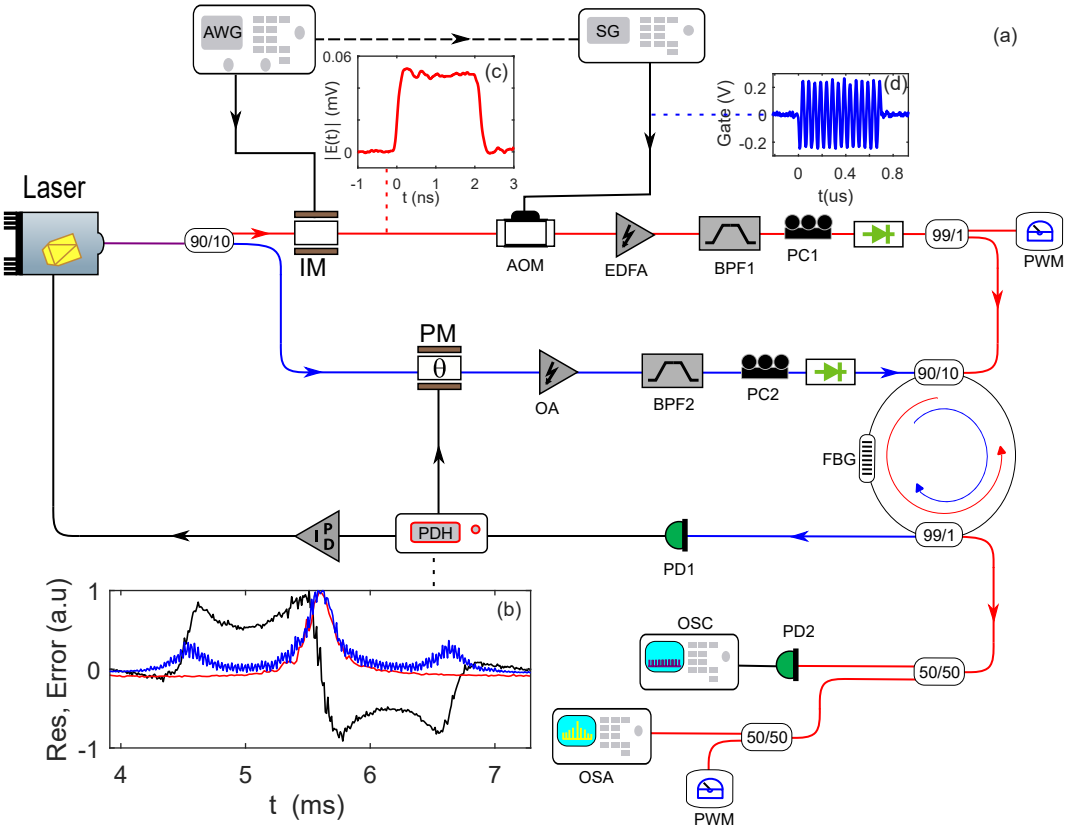

Figure 3.1 – (a) Illustration of the main experimental setup. IM: optical intensity modulator; AOM: acusto-optical modulator; EDFA: Erbium-Doped-Fiber Amplifier; BPF1,2: Optical Band pass filter; PC1,2: polarization controller paddles; PWM: power meter; PM: phase modulator; OA: optical amplifier; FBG: fiber Bragg grating; PD1: photodiode; PDH: Pound-Drever-Hall module; PID: proportional-integrative-derivative control module; OSC: oscilloscope; OSA: optical spectrum analyzer. (b) Example of a cavity resonance, in red, a modulated cavity resonance, in blue and the PDH error function in black. (c) A plot of a typical pulse and (d) example of the gating function that drive the AOM.

cavity, for the study of MI. Here we propose a modified version of those setup, with some improvements in the stabilization technique used, which proved to be very effective for the study of intracavity dynamics [101, 74, 75, 82, 61].

3.1.1 Fiber cavity

Before going into the detailed description of the experimental setup, we spend a few words about the fiber cavity. Given the nature of the phenomenon that we wanted to study, the cavity can not be simply a uniform fiber resonator. In particular, we wanted to characterize the GTF phenomenon in both normal and anomalous dispersion. To change the dispersion of a cavity the main approaches are, either to change the driving frequency of the pump, either to manage the average dispersion [99, 101] of the resonator, by splicing together different kind of fibers inside the cavity. The FBG used has been engraved into standard SMF-28 fibre, while the two tap couplers have been chosen to be normally dispersive at 1550nm. The main body of the cavity was made from 100 to 200 metres of dispersion-shift fibre, to which an additional piece of normally dispersive fibre was spliced in order to obtain the correct value of normal dispersion. All parameters are described in detail in the following sections.

3.1.2 Driving of the cavity

In the theoretical studies proposed in the previous chapter, all calculations are made under the assumption of a continuous wave laser. Even if for some kind of resonator, such as micro-resonators [63, 56], this assumption holds also at the experimental level, in fiber ring cavities this will bring to a critical problem, that is the Stimulated-Brillouin-Scattering (SBS) [102]. This phenomenon occurs when an incident photon is converted into a backscattered photon and an acoustic phonon, which deplete the pump. In addition, the interferometric nature of the cavity could lead to an increase in the intracavity power, further increasing the efficiency of SB and leading to Stimulated Brillouin Scattering [9, 13, 103], that results in a strong alteration of the pump. This non-linear dynamic is detrimental for our investigation, because, the threshold power of SBS is lower respect to the MI power threshold.

There are several approaches to limit or avoid the development of SBS in a cavity configuration. Among the most common are the inclusion of an isolator inside the cavity, which restricts the light to travelling in one direction only[61, 64]. This is not a good approach in our case because the isolators have high

insertion losses and we needed to circulate the light in both directions (see next section on stabilisation).

A different methods involves modulating the phase of the pump to reduce the Brillouin gain, or controlling the exact length of the cavity [103, 104]. One of the most effective ways of avoiding SBS is to modulate the amplitude of the CW laser into pulses. Indeed, by shortening the duration of the beam under a phonon lifetime ($\approx 10\,ns$), one can strongly increase the power threshold of SBS. In addition to that, by using a train of pulses, it is possible to reach high peak powers by maintaining the average intracavity power relatively low, which is particularly convenient for the study of nonlinear effects. For this reason, we have implemented a pulsed pump setup. The cavity can operate in a quasi-CW regime as long as the duration of the pulse is much longer than the period of the phenomena we want to study, a condition that will always be respected in this thesis. The disadvantage of this technique is the criticality of the synchronisation between the natural repetition rate of the cavity and the train of pulses. In fact, even a synchronisation mismatch of a few femto seconds can lead to significant changes in the behaviour of the MI [105].

Fig. 3.1 shows a scheme of the experimental setup. The laser pump is a CW tunable laser with a maximum output power of $44\,mW$ and a line width of less than $100Hz$. A small line width is essential for this application, especially when working with a fibre cavity where the FWHM of the resonance can easily be in the order of $100\,KHz$. The laser can be thermally tuned over an interval of $1\,nm$ with respect to its centre frequency and allows a fast tuning method via an externally controllable piezo.

The driving path is highlighted in red in the scheme: the pump is first divided into two via a 90/10 coupler, 90% used to generate the strong nonlinear beam (red path in Fig. 3.1), and 10% for the control beam (blue path in Fig. 3.1). Regarding the nonlinear beam: the wave is shaped into pulses, from 1 to 2 ns, using an intensity modulator (IM), the IM is driven by an arbitrary wave generator (AWG), which is used to generate the pulses and control their period. An example of a pulse is shown in Fig. 3.1(c) in the scheme.

The pulses are then frequency modulated by an acousto-optical modulator (AOM) driven by a signal generator (SG). We do this for two reasons: firstly, we

want to modulate the frequency of the pump ω_0, around $200\,MHz$, to control the phase detuning of the cavity (see relation in section 1.2.1). Secondly, it serves a *gating* function: AOM can reach an extinction ratio of up to 50 dB, further assuring the absence of SBS. By synchronising the SG with the AWG, it's possible to generate the sinusoidal signal corresponding to the pulse generated by the IM. Considering that the period of the pulses is of the order of $500\,\mu s$, and the gating sinusoidal signal has a typical width of $0.4\,\mu s$, we guarantee a 50 dB extinction ratio for this more than 90% of the period, minimising the possibility of any SBS insurgences between the pulses.

The use of the AOM to control the frequency, hence the phase detuning, of the driving signal is one of the main developments with respect to previous cavity setups [74, 61] and allows a very precise control of the phase at the cost of very little extra complexity.

The pulse train is then amplified by an erbium-doped amplifier (EDFA1) to reach power levels suitable for observing non-linear phenomena. To avoid traces of spontaneous emission from the EDFA1, the signal is filtered with a tunable bandpass filter (BPF1) before injection into the cavity. The signal then passes through a polarisation controller (PC1) to align it with one of the polarisation axes of the cavity, and an isolator to prevent any back reflection to the amplifier. Just before injection into the cavity, a small portion of the signal is diverted to an optical power meter (PM), which allows the P_{in} to be measured. The signal is then injected into the cavity via the 90/10 input coupler. The driving field travels inside the cavity and is extracted through a tap coupler, [90], and then processed with an oscilloscope and optical spectrum analyser. The use of the tap coupler is a convenient compromise in the design of the cavity. Although an additional coupler adds more losses to the fibre loop, it makes the separation of the control and drive signals trivial. Other approaches are either to lock the laser directly to a part of the driving field [64] or, to propagate the control and driving signals in the same direction, multiplexed in time and polarisation [61].

3.1.3 Stabilization of the cavity

One of the requirements of the experimental setup is to ensure the stability of the cavity. In this case, we are talking about the stability of the laser frequency with respect to one resonance of the cavity. In fact, when the cavity is made up of several metres of fibre, it becomes very sensitive to any small acoustic or mechanical vibration in the environment. The fact that the cavity acts as an interferometer is critical: the generation of the non-linear effects depends on the interference between the input and the intracavity fields, and therefore on the phase shift between the two, which must remain stable to obtain consistent results.

There are two main approaches to stabilising the phase of the system: locking the cavity to the laser, or vice versa, locking the laser to the cavity. In the first approach [80], the idea was to compensate for the phase perturbation by instantly changing the length of the cavity. This was achieved by rolling a certain amount of fibre from the cavity spool around a piezoelectric ring. The ring's electrodes were then connected to a proportional-integral-derivative (PID) controller, which provided the correction signal. The expansion or contraction of the piezo changed the total length of the cavity, hence the phase detuning. The error signal was simply the intracavity field extracted from the cavity, similar to what is done in our setup of Fig. 3.1, and this created a closed-loop system that was able to compensate for any perturbation of the laser directly at the cavity. This method worked, but it was not the best approach. In fact, the correction was made by a physical modification of the fibre, which itself induces some vibration inside the cavity. When the technology allows it, as in our case, it is more effective to lock the laser to the cavity, i.e. to let the laser frequency "follow" the phase perturbations of the cavity. The idea is to create a closed loop between the cavity and the laser, but this time the locking is done by changing the frequency of the laser. This method has been used in several cavity experiments [101, 74, 75, 82, 105], with good performances.

In our setup, the control loop is highlighted in the blue path in Fig. 3.1. A small percentage (10%) of the pump is sent to a phase modulator (PM). The modulated signal is amplified, to compensate for the any losses. The power level

of the control signal is kept relatively low to avoid unwanted effects such as SBS. The amplified signal is then filtered (BPF2) and its polarisation adjusted to one of the axes of the cavity. An isolator prevents any leakage of power from the drive fields, then the control signal is injected into the cavity. As for the drive field, the signal is collected from a port of the tap coupler and sent to a photodiode (PD1), which converts the optical signal into an electrical signal ready to be processed by the control system and fed to the laser's piezo.

For this work we decided to adapt a control technology usually used in precision laser interferometry, known as Pound-Drever-Hall (PDH) stabilization technique. There are three main block implied in this technique, that are the phase modulator (PM), the PDH and the PID modules as in Fig. 3.1. We provide a brief introduction of this technique in the following section.

Pound-Drever-Hall stabilization technique

This technique, named after its developers [106], is a powerful method for improving the frequency stability of lasers. It is mostly used in interferometry applications, such as gravitational wave detection [107], and in atomic physics for probing optical resonances [108]. A detailed description of this technique can be found in [109], and we suggest here a general overview to understand the system.

The concept of PDH is straightforward: to measure a laser frequency and eliminate any fluctuations using a cavity, (typically a Fabry-Perot cavity), regardless of the laser intensity changes. In our situation, we are utilising a fiber ring cavity, but the principle remains unchanged.

In Fig. 3.2 (a) we reported in red a typical reflected power of a Fabry-Perot cavity, which is equivalent to the output power of a fiber ring cavity as described in Chap. 1. When the incident field is resonant with the cavity, the reflected power is at its minimum because all the light is coupled inside the cavity (in the ideal case of zero losses). If the frequency of the field varies slightly, the reflected power changes. Intuitively, we can think of a system that allows us to compensate for the variation of the frequency of the laser in order to keep the laser exactly at resonance. Unfortunately, the reflected power alone does not

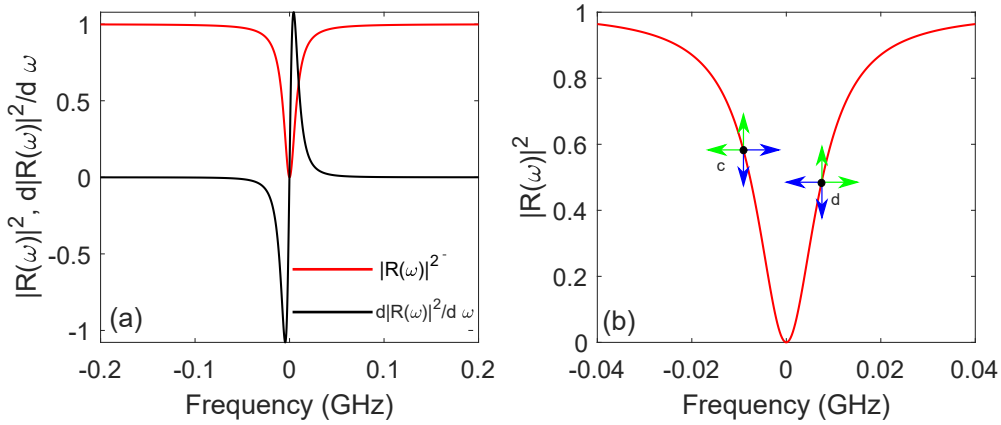

Figure 3.2 – (a) in red, plot of a typical profile of the reflected power of a Fabry-Perot cavity; In black it's a plot of its derivative. (b) approximation of the derivative mechanism operated by the PDH technique: for the point d, when the frequency increases, the relative power increases while when the frequency decreases the power decreases. Conversely, for the point c, when the frequency increases, the power decreases and vice-versa. This mechanism allows to approximate the asymmetric nature of the derivative of the reflected power.

provide sufficient information to determine whether the laser frequency needs to be increased or decreased, due to the symmetric nature of the resonant function with respect to its central value. Alternatively, the derivative of the reflected field, the black plot in Fig. 3.2(a), is asymmetric with respect to the resonance condition. This means that a variation of the frequency in the derivative of the reflected power gives a clear indication of how to adjust the laser frequency to return to resonance.

Basically, the PDH technique allows to calculate an error function that is proportional to the derivative of the reflected field, providing a correction that is independent of the intensity of the field itself. In practice, instead of calculating the derivative of the resonance, it's possible to apply a small frequency modulation to the incident field and see how the reflected beam responds. We offer a graphical representation of the process in Fig. 3.2 (b). If the reflected power is above the resonance, as for the point d, a positive frequency variation corresponds to an increase in reflected power, while a negative frequency variation corresponds to a decrease in reflected power. Conversely, if the field is below resonance, as for the point c, a positive variation in frequency corresponds to a

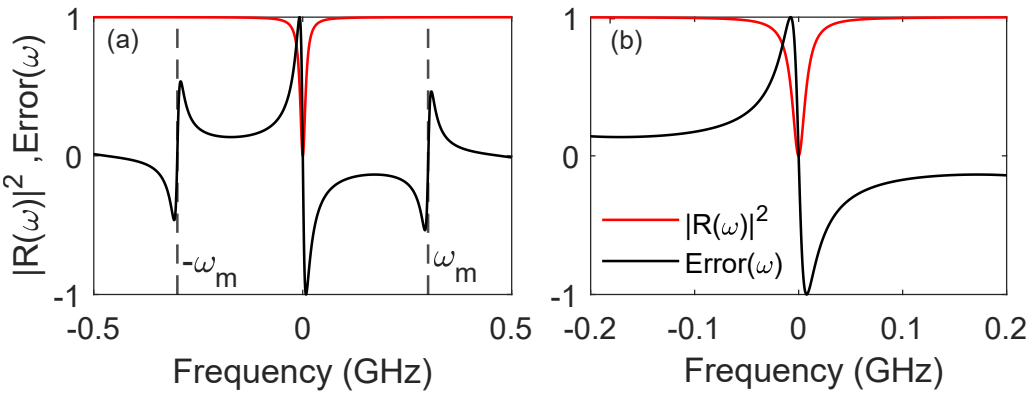

Figure 3.3 – (a) Plot of the reflected power, in red, and the error function computed by the PDH system, in black. Dashed vertical lines refers to the modulation sidebands at $\pm\omega_m = 0.35$ GHz from the resonance. (b) zoom in the center of the figure.

decrease in reflected power and vice versa for a negative variation in frequency. Thus, by comparing the modulation frequency sign with the reflected signal variation, it is possible to determine on which side of resonance the laser falls. This information can be processed and used to derive an error signal to correct the frequency of the laser.

In practice, this operation is achieved by modulating the phase of the signal (this is the role of the PM in the setup shown in Fig. 3.1). The modulation creates two sidebands, which contain a phase relation to the modulation signal and reflected beams of the cavity. By beating the modulated reflected signal with the local oscillation of the modulation, it's possible to extract an error function proportional to the derivative of the signal [109], which is plotted in black in Fig. 3.3 (a). Note that the slope of the error function is opposite to the slope of the derivative, as it gives an indication of the correction to be made to the frequency of the laser, see the zoom in Fig. 3.3 (b). To keep the laser locked on top of the resonance of the cavity, a PID module can be use to keep the error signal near its zero.

Apart from the phase modulation, all the operation are made internally the PDH module (Digilock 110, Feedback controlizer, Toptica), so this technique is particularly simple to implement. In Fig. 3.1 (b) we have plotted the typical profile of a resonance in red. The blue trace is the modulated reflected field,

showing the two sidebands of the phase modulation, and the black trace is the internally calculated error signal. It should be noted that for this experiment we used the PDH in transmission mode [110], i.e. we used the intracavity (transmitted) field instead of the reflected (output) field. In principle, this could be detrimental, since transmitting the modulated band within the cavity reduces the instantaneous phase noise obtained from the error signal. In our setup, we have experimentally tested both configurations (PDH in reflection and transmission mode) without noticeable differences. Therefore, since access to the intracavity field was necessary to characterise the nonlinear phenomenon, we stayed with the transmission mode as shown in Fig. 3.1. In addition to the improved stability, the other major advantage of using the PDH technique is that the laser is stabilised at the top of the cavity resonance, which means that the estimation of the detuning is easier compared to the "classical" side-of-fringe locking achievable with a simple PID controller.

3.2 Experimental investigation

In chapter 2 we gave a general description of the GTF phenomenon, showing its dependence on different filter parameters, such as bandwidth, loss depth and the relative wavelength shift between the pump and the Bragg frequency. The latter example is the one that shows one of the most interesting characteristics of this phenomenon, that is the possibility of *tuning* the position of the MI band, by changing the λ_p or λ_f [61]. In the first experimental demonstration, the cavity was kept in a state where only GTF instability was possible, but in Fig. 2.9 we have shown how, in the right configuration, the parametric gain predicts not only GTF but also parametric MI bands. Parameters such as β_2, P and ϕ_0 play a central role in the parametric process that governs the generation and characteristics of MI bands, so we decided to conduct a study of the dependence of GTF and parametric MI bands on these notable parameters.

3.2.1 GTF and parametric instabilities: Anomalous dispersion

Before going into the detailed explanation of the results, we will describe the structure of the cavity as it will change from the anomalous to the normal dispersion case. As previously mentioned, the dispersion of the cavity can be controlled by adding different fibres to the spool.

In this case, the cavity had a length of 114 metres, corresponding to a repetition rate of $1.766\,MHz$. In particular, the cavity was composed of two main types of fibre: 3.77 metres of SMF-28 fibre, (including the two couplers and the FBG filter), whose dispersion was estimated to $-21\,ps^2/km$, and approximately 110.23 metres of DSF, whose dispersion was about $0.44\,ps^2/km$. The resulting average dispersion was $\beta_2 = -0.26\,ps^2/km$.

The main objective of this investigation was to study the evolution of the parametric instability bands and the GTF in a state where both can be stimulated inside the cavity. In particular, we decided to study this behaviour focusing on ϕ_0, since it's a key parameter for intracavity MI, and this kind of characterisation was still lacking in the GTF domain. We note here that, for simplicity, we have always kept the cavity in a monostable regime.

To get an idea of what kind of behaviour we should expect from such an investigation, we analysed Eq. (2.32), which is the parametric gain for the Ikeda map model. The parameters used are listed in the caption of the figure 3.4, but we stress that the value of β_2 used is the averaged value obtained by fitting the parametric instability bands. Fig. 3.4(a), (c) and (e), are the 2D plots of the gain as a function of the input power P_{in}, for ϕ_0 =-0.1, 0 and 0.1 rad respectively. Plots (b),(d) and (f) are three snapshots of the parametric gain for $P_{in} = 2\,W$. In all 2D plots, we have marked the power threshold of the parametric instability with a horizontal blue dashed line, and the power threshold of the GTF with a dashed red line. The vertical black dashed line represents the central frequency of the filter. The two types of bands can be easily identified by their position: in all plots, the bands around 1 THz are the parametric MI bands, and they follow the typical outward trajectory as the power increases, while the GTF bands always grow next to the central position of the filter.

Looking at the thresholds of the two instabilities in Fig. 3.4, one can see

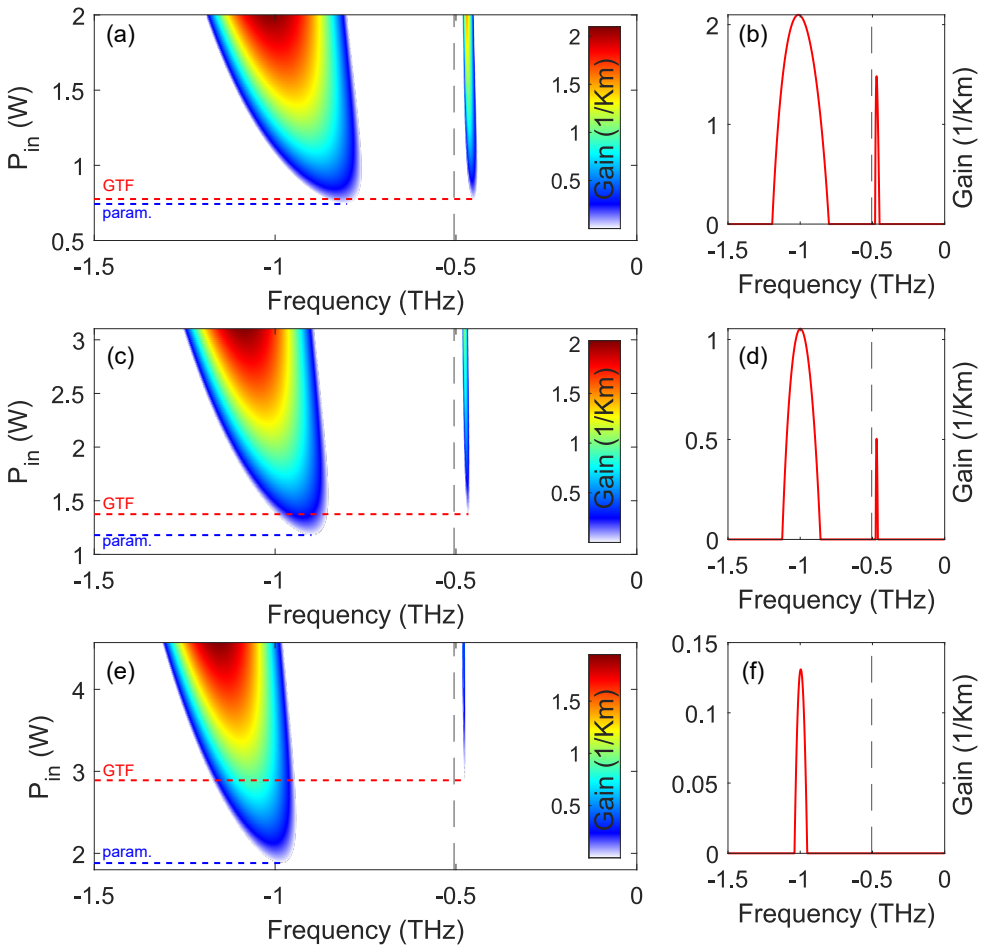

Figure 3.4 – Parametric gain as a function of P_{in} for three different cavity detunings. Only the negative frequencies are shown do to the symmetry of the gain. Plot (a) is the gain computed for $\phi_0 = -0.1$ (rad), and (b) is the plot of the gain for $P_{in} = 2$ W. Plot (c) is the gain computed for $\phi_0 = 0$ (rad), and (d) is the plot of the gain for $P_{in} = 2$ W and, finally, plot (e) is the gain computed for $\phi_0 = 0.1$ (rad), and (b) is the plot of the gain for $P_{in} = 2$ W. The black dashed line indicates the central frequency position of the filter. The parameter used in the computation of the gain are: $\rho = \sqrt{0.65}, \theta = \sqrt{0.05}$, $\gamma = 2.5/W/mm$, $L = 113$ m, $\beta_2 = -0.28\, ps^2/km$, $\lambda_p = 1545.4\, nm$, $\lambda_f = 1549.4\, nm$.

how they change with the detuning ϕ_0. In particular, the thresholds of the two instabilities changes differently with the detuning. Indeed, it's possible to see that as the detuning increases, so does the thresholds value. In particular from $P_{in} = 0.75$ W for $\phi_0 = -0.1$ rad, to $P_{in} = 1.93$ W for $\phi_0 = 0.1$ rad. But if you look

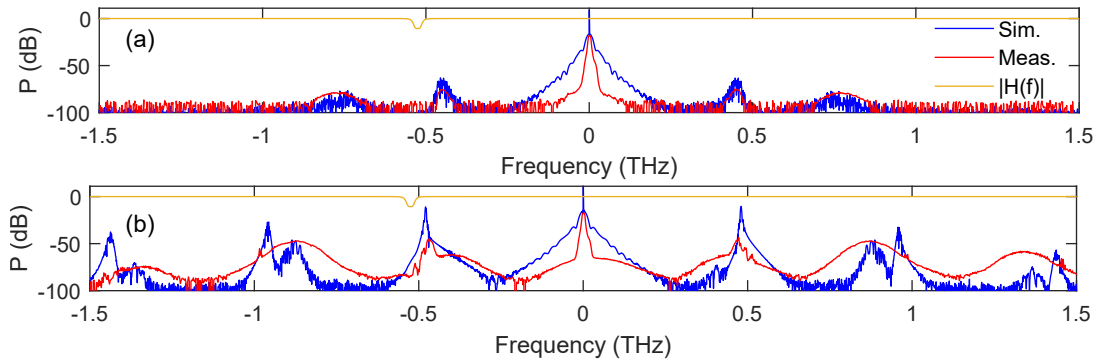

Figure 3.5 – Plot of measured spectra, in red, compared to numerical simulations, in blue, for a detuning $\phi_0 = -0.1$ rad. (a) spectra corresponding to $P_{in} = 1.785$ W, (b) spectra corresponding to $P_{in} = 1.95$ W. The parameters used for the numerical simulations are: $L_{SMF} = 3.77$ m,$\beta_{2SMF} = -21\ ps^2/km$, $L_{DSF} = 110.23$ m, $\beta_{2DSF} = 0.44\ ps^2/km$,$\gamma = 2.5/W/km$, $\rho = \sqrt{0.65}, \theta = \sqrt{0.05}$, $\lambda_p = 1545.4\ nm$, $\lambda_f = 1549.4\ nm$.

at the variation of the GTF bands, the difference in the thresholds is steeper: $P_{in} = 0.80$ W for $\phi_0 = -0.1$ rad, to $P_{in} = 3.11$ W for $\phi_0 = 0.1$ rad.

This feature can be better appreciated by looking at the snapshots plots of Fig. 3.4 (b)-(d) and (f), which show the gain at a fixed $P_{in} = 2$ W. In Fig. 3.4 (b), where $\phi_0 = -0.1$ rad, the two instabilities have almost the same gain,$2\ km^{-1}$, for the parametric bands and about $1.5\ km^{-1}$ for the GTF bands. In Fig. 3.4 (d), the intensity of the parametric bands is more than twice that of the GTF bands, and finally in Fig. 3.4 (f), only the parametric bands are visible. This dynamic shows that by increasing the detuning, the bands become less intense at the same power level and, more importantly, the two instabilities behave differently, with the threshold of the GTF bands growing faster than the threshold of the parametric MI.

This simple analysis of the parametric gain shows an interesting behaviour of the two instabilities, so we decided to proceed with an experimental and numerical study of the spectra generated inside the cavity. Our setup allows an easy way to control the detuning by acting on the modulation frequency of the AOM, while the input power is controlled with the EDFA 1 (see Fig. 3.1). Fig. 3.5 shows the results for $\phi_0 = -0.1$ rad and in particular in plot (a) $Pin = 1.785$ W and in plot (b) $Pin = 1.95$ W. The red traces are the measurements, the blue are

numerical simulations and the yellow trace is the loss profile of the filter. The numerical simulations are obtained by integrating the Ikeda Map model of Eqs. (2.1) with a split-step Fourier method [111] and are performed by adiabatically increasing the power, starting from a state where the system is stable. In Fig.

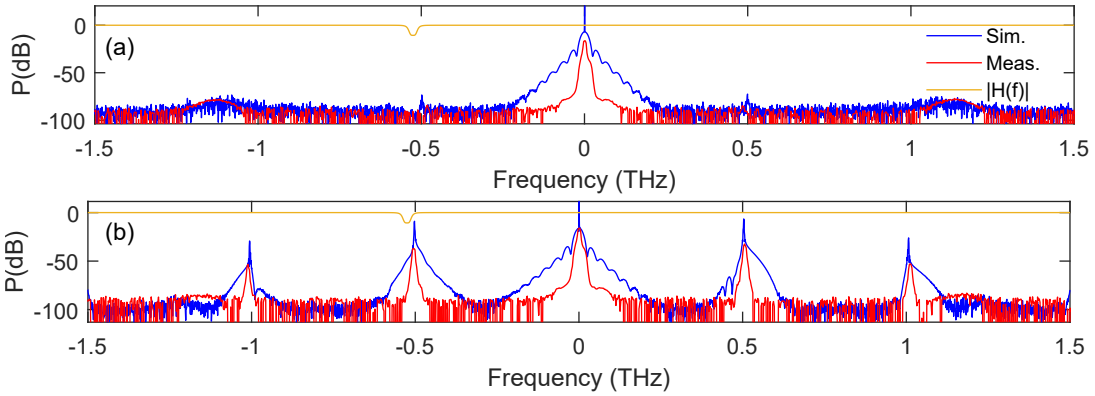

Figure 3.6 – Plot of measured spectra, in red, compared to numerical simulations, in blue, for a detuning $\phi_0 = 0.1$ rad. (a) spectra corresponding to $P_{in} = 0.95$ W , (b) spectra corresponding to $P_{in} = 1.05$ W . The parameters used for the numerical simulations are: $L_{SMF} = 3.77$ m,$\beta_{2SMF} = -21\, ps^2/km$, $L_{DSF} = 110.23$ m, $\beta_{2DSF} = 0.44\, ps^2/km$,$\gamma = 2.5/W/km$, $\rho = \sqrt{0.65}, \theta = \sqrt{0.05}$, $\lambda_p = 1545.4\, nm$, $\lambda_f = 1549.4\, nm$.

3.5(a), as predicted by the previous theoretical study, it can be seen that the GTF bands, positioned at about ±0.5 THz from the pump, and the parametric bands, positioned at about ±0.8 THz from the pump, coexist with almost the same intensity. By increasing the power, as in the case of Fig. 3.5 (b), the GTF gain bands become more intense, especially close to the pump, and almost merge with the parametric gain MI bands. The numerical simulation agrees quite well with the measurements and it can be seen that the position of the bands is well respected. In order to obtain such an agreement, the Ikeda map integration includes the different type of fibre used in the experiment. The position of the bands fits quite well with the values given by the theoretical gain, calculated with an averaged value of β_2, but the dynamic growth of the band with the input power was not well predicted by modelling the system with a single piece of fibre with averaged dispersion. In Fig. 3.6 we show the result at $\phi_0 = +0.1$ rad, for $Pin = 0.95$ W in the panel (a) and $Pin = 1.05$ W in panel (b). In this

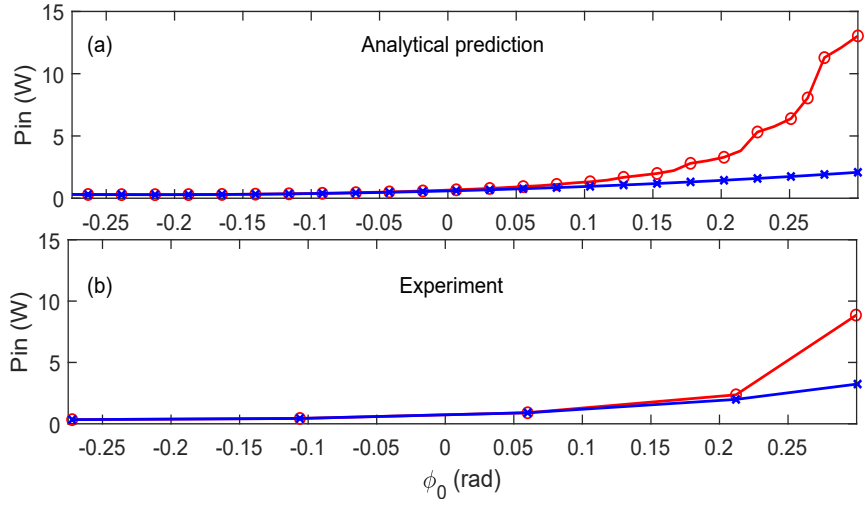

Figure 3.7 – Theoretical (a) and measured (b) thresholds of parametric (blue) and GTF instabilities (red). The numerical calculation of the threshold has been done with the same parameters found in the caption of Fig. 3.6.

example, we can see that the parametric instability, situated at about ±1.1 THz from the pump, rises alone, as predicted by the theoretical gain of Fig. 3.4 (e). Interestingly, at an higher power, plot of Fig. 3.6 (b), the GTF instability bands seems to almost completely overcome the parametric instabilities. The numerical simulations fits quite well with the measurements, even if a perfect separation of the two instabilities was very hard to get at low power. Indeed it is possible to see a residue of the GTF bands in the blue trace of plot (a), even if the bands doesn't grows in space, differently from the parametric band.

As final result for the anomalous dispersion case, we measured the power threshold of the two instability as function of ϕ_0. In Fig. 3.7 (a) we plotted the theoretical thresholds, and in Fig. 3.7 (b) is the measured thresholds. As shown in the plots, the dynamic is well respected but the value of the power shows a discrepancy. Once again, the difficulty of perfectly matching the values of the thresholds could be linked to the different kind of fiber used.

In conclusion, we have been able to characterise theoretically, numerically and experimentally the GTF and parametric instabilities dynamics in an anomalous dispersive cavity. In particular, we have highlighted the difference in the thresholds power of the two instabilities as a function of the phase detuning.

3.2.2 GTF and parametric instabilities: Normal Dispersion

We now analyse this dynamics in a normal dispersion fiber cavity. To reach the right dispersion we followed several steps: first we first doubled length of the DSF, for a total of about 203 metres. Then we added piece of about 1.8 metres of normally dispersive fibre with a dispersion of $\beta_{2DSF} = 6\, ps^2/km$. The input and tap couplers were also replaced with DSF couplers to be as homogeneous as possible with the rest of the cavity. With this structure, the only SMF left was that of the FBG filter, with a length of $L_{SMF} = 0.5$ m and the typical value of $\beta_{2SMF} = -20\, ps^2/km$. The result of the dispersion management was an average value of $\beta_2 = 0.43 ps^2/km$, at the cost of slightly higher losses due to the increased number of splices within the cavity.

To have an idea of the behaviour of the thresholds, we first look at the MI gain as a function of the input power and the phase detuning ϕ_0. In Fig. 3.8 we plot three examples of gain as a function of P_{in}, with $\phi_0 = -0.3$ rad for plot (a), $\phi_0 = 0$ rad in (c) and $\phi_0 = 0.3$ rad in (e). Subplots (b), (d) and (f) are examples of the relative gains for $P_{in} = 15.3$ W. We have highlighted the threshold of the GTF with red dashed lines, the threshold of the parametric instabilities with a blue dashed line and the vertical black dashed line represents the centre frequency of the filter. We remark the presence of both the GTF and the parametric MI bands in the gain plots.

Looking at the thresholds, we can see a significant difference with respect to the anomalous case. In fact, looking at Fig. 3.8(a), we can see that GTF has a much lower power threshold than its parametric counterpart, which are $P_{in} = 9$ W and $P_{in} = 11$ W respectively. By increasing the detuning, as in Fig. 3.8(c) and (d), the thresholds of the GTF and parametric instabilities come closer together, $P_{in} = 13.6$ W parametric and $P_{in} = 13.7$ W for the GTF, to finally reverse their position, as shown in Fig. 3.8 (e), where the parametric instability starts at $P_{in} = 14.8$ W, while the GTF starts at $P_{in} = 18$ W. If the different evolution of the threshold of the two instabilities was already observed in the anomalous case, the inversion of the threshold is a completely peculiar characteristic of the normal dispersion regime.

In order to better analyse this behaviour, we have carried out some mea-

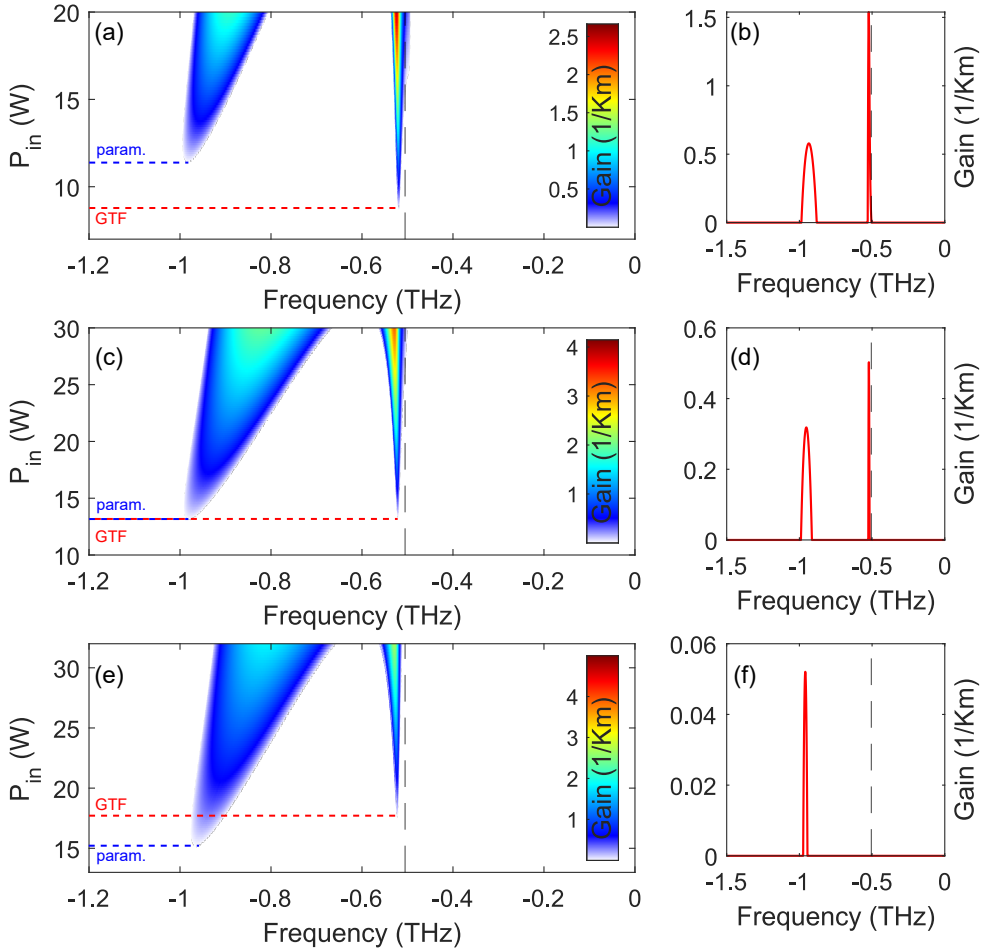

Figure 3.8 – Three examples of parametric gain as function of different phase ϕ_0. Only the negative frequencies are shown do to the symmetry of the gain. Plot (a) is the gain computed for $\phi_0 = -0.3$ (rad), and (b) is the plot of the gain for $P_{in} = 15.3$ W. Plot (c) is the gain computed for $\phi_0 = 0$ (rad), and (d) is the plot of the gain for $P_{in} = 15.3$ W and, finally, plot (e) is the gain computed for $\phi_0 = 0.3$ (rad), and (f) is the plot of the gain for $P_{in} = 15.3$ W. The black dashed line indicates the central frequency position of the filter. The parameter are: $\rho = \sqrt{0.635}, \theta = \sqrt{0.05}$, $\gamma = 2.5/W/km$, $L = 205.3$ m, $\beta_2 = 0.43\, ps^2/km$, $\lambda_p = 1545.4\, nm$, $\lambda_f = 1549.4\, nm$.

surements and numerical simulations of the spectrum. In Fig. 3.9 we show an example of two different spectra taken with a detuning of $\phi_0 = -0.26$ rad. In Fig. 3.9 (a) $P_{in} = 14.1$ W, while in Fig. 3.9 (b) $P_{in} = 18$ W. The red traces are the measurements, while the blue traces are the simulations. The yellow trace is the

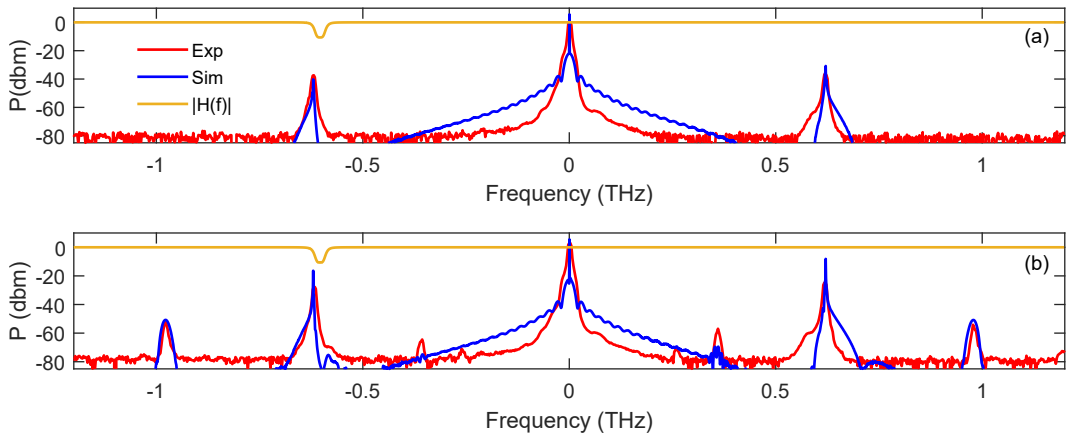

Figure 3.9 – Plot of measured spectra, in red, compared to numerical simulations, in blue, for a detuning $\phi_0 = -0.26$ rad. (a) spectra corresponding to $P_{in} = 14.1$W , (b) spectra corresponding to $P_{in} = 18$ W. The parameters used for the numerical simulations are: $L_{NORM} = \beta_{2NORM} = 6\,ps^2/km$ $L_{SMF} = 3.77$ m,$\beta_{2SMF} = -21\,ps^2/km$, $L_{DSF} = 110.23$ m, $\beta_{2DSF} = 0.44 ps^2/km$,$\gamma = 2.5/W/km$, $\rho = \sqrt{0.65}$,$\theta = \sqrt{0.05}$, $\lambda_p = 1545.4\,nm$, $\lambda_f = 1549.4\,nm$.

power loss profile of the filter. It's already visible how, at the lower power, only GTF bands are visible at ±0.61 THz from the pump. By increasing the power, as shown in Fig. 3.9 (b), parametric MI bands begin to appear at ±0.97 THz from the pump, and also generate spurious components at ±0.36 THz from the pump. This coexistence is similar to the one observed in the anomalous case, but unlike before, there is a condition where the GTF exists without any other instability. The numerical simulations are obtained by integrating the complete Ikeda Map model of Eq. (2.24) are in good agreement with the measurements. Similarly, in Fig. 3.10 we report two plot, measured with $\phi_0 = 0.26$ rad, an $P_{in} = 21$ W in plot (a) and $P_{in} = 26$ W in plot (b). The color coding of the traces is the same as before. As suggested by the theoretical results, for this value of detuning, parametric instabilities rises first, as depicted in plot (a), at about ±0.95 THz from the pump, and by raising the power some GTF instability bands arises at around ±0.57 THz from the pump, creating once again some spurious components at ±0.38 THz.

Interestingly, we note that it's possible to get different spectra, and switch from one to another by changing the linear detuning. This behaviour was not obvious in the anomalous case analysed in this work, and it was never analysed

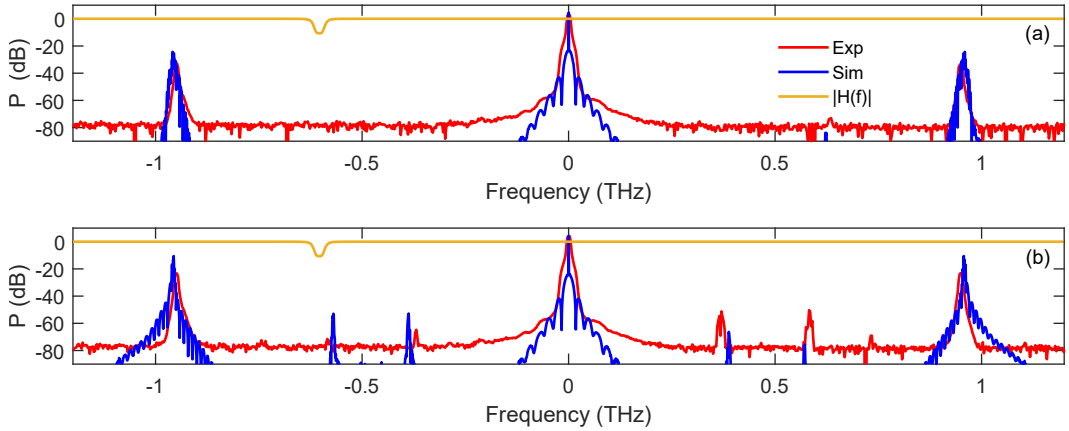

Figure 3.10 – Plot of measured spectra, in red, compared to numerical simulations, in blue, for a detuning $\phi_0 = 0.26$ rad. (a) spectra corresponding to $P_{in} = 21$ W, (b) spectra corresponding to $P_{in} = 26$ W. The parameters used for the numerical simulations are: $L_{NORM} = \beta_{2NORM} = 6\, ps^2/km$ $L_{SMF} = 3.77$ m,$\beta_{2SMF} = -21\, ps^2/km$, $L_{DSF} = 110.23$ m, $\beta_{2DSF} = 0.44\, ps^2/km$,$\gamma = 2.5/W/km$, $\rho = \sqrt{0.65}, \theta = \sqrt{0.05}$, $\lambda_p = 1545.4\, nm$, $\lambda_f = 1549.4\, nm$.

in previous work about GTF [61, 60, 59]. To conclude this study, we performed a measurement of the thresholds of the two instabilities as a function of detuning. Figures 3.11 show the parametric (blue) and GTF (red) thresholds from the analytical (Eq. (2.32), Fig. 3.11 (a)) and numerical (Eq. (2.24), Fig. 3.11 (b)) predictions, compared to experiments (Fig. 3.11 (c)). First of all, we have a fairly good qualitative agreement between the theoretical predictions (Fig. 3.11 (a) and (b)) and the experimental results (Fig. 3.11 (c)). For small values of cavity detuning, GTF instabilities appear first, while for large values the situation is reversed.

The agreement between numerical simulations and experiments is quite good, considering that the threshold can be affected by noise, slight fluctuations of the stabilisation system or drifts of the synchronisation mismatch. The analytical model, assuming a uniform cavity, gives a very good qualitative description of the dynamics of the system and can be used to get a quick physical insight into the process.

In conclusion, we have theoretically and experimentally characterised the coexistence of GTF and parametric instabilities in a fiber ring cavity, for both

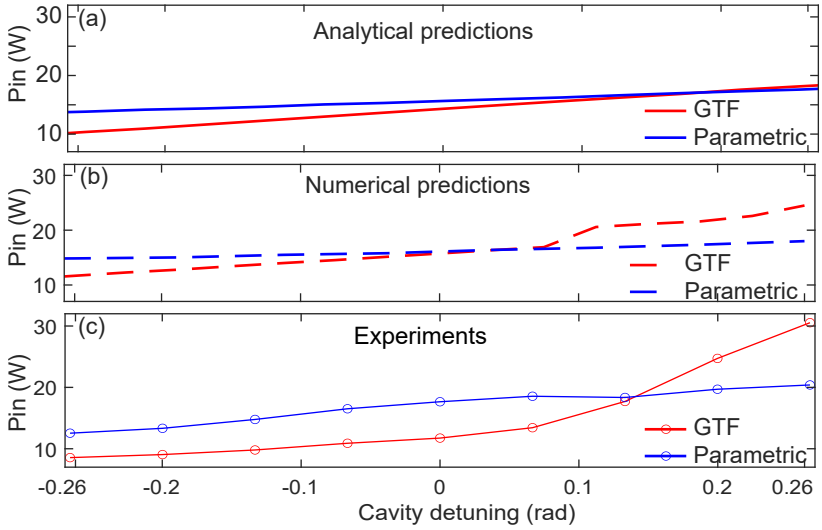

Figure 3.11 – The theoretical (a), numerical (b) and measured (c) thresholds of parametric (blue) and GTF instabilities (red). The numerical calculation of the threshold has been done with the same parameters found in the caption of Fig. 3.6.

anomalous and normal dispersion regimes. In particular, we analysed and measured the behavior of the power thresholds of GTF and parametric instability, and demonstrated how it is possible, in case of normal dispersion, to modify the type of spectra by simply changing the linear phase detuning. In both cases we obtained a good agreement between experimental results and numerical simulations. This study helps to complete the analysis on GTF phenomenon, and gives a more in-depth analysis on how it can interact with other instabilities, extending the knowledge of previous studies on the topic [61].

3.3 Summary

- We described the main structure of the experimental setup used in the experiment. In particular, we described the driving and the stabilization of the cavity, with a focus on the PDH technique.

- Using the theory developed in the previous chapter, we show analytically how the GTF phenomenon can coexist with parametric instability in fibre

cavities. In particular, we have studied the phenomenon on two different cavities, in the anomalous and the normal dispersion regimes. In both cases, we show how the power thresholds of the two instabilities depend on the linear phase detuning of the cavity. In the case of normal dispersion, we observe the inversion of the order of appearance of the instability type, which depends on the phase detuning. We also obtained a good overall agreement between the measurements, the numerical results and the theoretical results.

Chapter 4

Polarization Maintaining GTF

4.1 GTF in Polarization Maintaining Fibers

In this chapter, we will derive a model to study GTF in polarisation-maintaining (PM) fibers, along with a theoretical and numerical investigation of the phenomenon. Several studies have been carried out on MI in optical fibres and resonators [112, 113, 114]. Often the idea is to obtain an additional degree of freedom in the phase matching relation by exploiting the different phase detuning in the two polarisation axes, mostly when the balance between chromatic dispersion and nonlinearities is not sufficient to obtain MI [115, 32, 116, 117].

With this work, we wanted to combine the different degrees of freedom offered by the GTF [60, 61] with those offered by the PM fibres. In particular, the idea is to exploit the characteristic of PM fibers, such as the difference in the refractive index of the two polarisation axes, to generate optical spectra with different FSR, as is done in some dual-frequency comb laser architectures [118, 119]. First, we will describe the particular type of filter we will use in GTF generation, then we will derive the Ikeda map and LLE equations to describe the parametric gain. After that, we will propose a theoretical study of the two models to determine the parametric gain. In the final section, we will present the numerical simulation of dual-frequency comb-like MI spectra, in a PM fibre with PM FBG as a filter with realistic parameters.

4.1.1 PM Fiber Bragg Grating

In this section we introduce a model for a PM fiber Bragg grating that, due to the difference in the refractive index of the two polarisation axes, manifests two different loss profiles with slightly different Bragg wavelength, one for each polarisation axis [120, 121]. The model of the filter previously derived for the GTF analysis can be easily adapted to this new form: in fact, it is enough to define the FBG with two independent components, x and y, which will have the same shapes (i.e. the same a and b parameters [60]) but slightly different central frequencies. We will therefore use the following definition for the filter's transfer function:

$$H_{x,y}(\omega) = e^{F_{x,y}(\omega)+i\psi_{x,y}(\omega)} = \mathbb{F}[h_{x,y}(t)], \tag{4.1}$$

with $\mathbb{F}$ representing the Fourier transform, and $h_{x,y}(t)$ the impulse response of the filter, where the amplitude and phase are defined as:

$$F_{x,y}(\omega) = b\frac{a^4}{(\omega-\omega_{f_{x,y}})^4 + a^4} \tag{4.2}$$

$$\psi_{x,y}(\omega) = ba\frac{(\omega-\omega_{f_{x,y}})[(\omega-\omega_{f_{x,y}})^2 + a^2]}{\sqrt{(2)}[(\omega-\omega_{f_{x,y}})^4 + a^4]} \tag{4.3}$$

This description is identical to the one used for the single polarisation case, but the subscript x, y defines the different polarisation angles. In the following analysis, whenever these subscripts are given, we consider the effect of the two separate polarisation axes.

4.2 Ikeda map

In the following, we introduce a vectorial Ikeda map, taking into account the two polarisation axes of the fibre and the interaction between them.

The propagation of the orthogonal linearly polarised field can be described

by the following system of coupled NLSEs:

$$\begin{cases} \dfrac{\partial E_x}{\partial z} = \Delta\beta_1 \dfrac{\partial E_x}{\partial t} - i\dfrac{\beta_2}{2}\dfrac{\partial^2 E_x}{\partial t^2} + i\gamma(|E_x|^2 + \sigma|E_y|^2)E_x \\ \dfrac{\partial E_y}{\partial z} = -\Delta\beta_1 \dfrac{\partial E_y}{\partial t} - i\dfrac{\beta_2}{2}\dfrac{\partial^2 E_y}{\partial t^2} + i\gamma(|E_y|^2 + \sigma|E_x|^2)E_y \end{cases} \tag{4.4}$$

Where $E_{x,y}$ are the envelopes of the signal propagating in the slow and fast polarisation axesy, $\Delta\beta_1 = (\beta_{1x} - \beta_{1y})/2$ is the group velocity mismatch between the two axes, β_2 is the group velocity dispersion parameter and γ is the Kerr nonlinear parameter. The parameter $\sigma = 2/3$ [122] describes the cross-polarisation interaction.

The birefringence introduced by the PM structure leads to the appearance of the first order dispersion term $\Delta\beta_1$ in the equations, due to the difference in the speed of propagation of the light in the two polarisation axes. The two polarisation components $E_{x,y}$ are coupled by a cross-polarisation factor σ.

Since we are describing a ring cavity, we need to add the boundary condition term to complete the description of the system. As in the previous description of the GTF in section 2.2.5, we consider all losses, except those induced by the filter, combined in the loss factor ρ. Given this, the boundary conditions connecting the fields at the end of the round trip n, $E^n_{x,y}(L,t)$, to those at the beginning of the following round trip $n+1$, $E^{n+1}_{x,y}(0,t)$, can be described as follows:

$$\begin{cases} E^{n+1}_x(0,t) &= \theta E_{inx} + \rho e^{i\phi_{0x}} h_x(t) \star E^n_x(L,t), \\ E^{n+1}_y(0,t) &= \theta E_{iny} + \rho e^{i\phi_{0y}} h_y(t) \star E^n_y(L,t). \end{cases} \tag{4.5}$$

where $E_{inx} = E_{in}\cos(\chi)$ and $E_{iny} = E_{in}\sin(\chi)$ are the input fields distributed along the two polarisation axes depending on the injection angle χ, and L is the total length of the cavity. For simplicity, we assume that the coupler characteristic is the same on both polarisation axes, so we keep $\theta = \theta_x = \theta_y$ and $\rho = \rho_x = \rho_y$. The conditions can be formulated in the frequency domain:

$$\begin{cases} \hat{E}^{n+1}_x(0,\omega) &= \theta E_{inx}\delta(\omega) + \rho e^{i\phi_{0x}} H_x(\omega)\hat{E}^n_x(L,\omega), \\ \hat{E}^{n+1}_y(0,\omega) &= \theta E_{iny}\delta(\omega) + \rho e^{i\phi_{0y}} H_y(\omega)\hat{E}^n_y(L,\omega). \end{cases} \tag{4.6}$$

4.2.1 Stationary solutions of the Ikeda Map

It's possible to compute the CW steady state inside the fiber as:

$$\begin{cases} E_x^n(z,t) = E_{0x}^{i\gamma(P_x+\sigma P_y)z},\ E_{0x} = E_{0x}e^{i\zeta_x} = \sqrt{P_x}e^{i\zeta_x}, \\ E_y^n(z,t) = E_{0y}^{i\gamma(P_y+\sigma P_x)z},\ E_{0y} = E_{0y}e^{i\zeta_y} = \sqrt{P_y}e^{i\zeta_y}. \end{cases} \tag{4.7}$$

where $\zeta_{x,y}$ are the steady state phases of the fast and slow axes, respectively. With these relations we can calculate the relation between the input and intracavity fields and powers:

$$\begin{cases} E_{0x} = \frac{\theta E_{inx}}{1-\rho H_x(0)e^{i\phi_x}}, \\ E_{0y} = \frac{\theta E_{iny}}{1-\rho H_y(0)e^{i\phi_y}}. \end{cases} \tag{4.8}$$

$$\begin{cases} P_x = \frac{\theta^2 P_x}{1+\rho^2|H_x(0)|^2-2\rho|H_x(0)|cos(\phi_x+\psi_x(0))}, \\ P_y = \frac{\theta^2 P_y}{1+\rho^2|H_y(0)|^2-2\rho|H_y(0)|cos(\phi_y+\psi_y(0))}. \end{cases} \tag{4.9}$$

where the total phases accumulated during the propagation on the fast and slow axes are $\phi_x = \gamma(P_x + \sigma P_y)L + \phi_{0x} + \zeta_x$ and , $\phi_y = \gamma(P_y + \sigma P_x)L + \phi_{0y} + \zeta_y$.

Except for the case where the injection angle is a multiple of $\pi/2$, the two states are always coupled, so the computation of P_x and P_y is done numerically. From this solution it's possible to calculate the phase of the steady states, according to the definition $\bar{E}_{x,y} = \sqrt{P_{x,y}}e^{i\zeta_{x,y}}$.

The evolution of the steady state allows to characterise the usual features of the cavity, such as the typical *S-shaped* function $P(P_{in})$. A particularly interesting analysis can be made by studying the dependence of the steady states on the injection angle of the pump.

Assuming that P_{in} linearly polarized, by changing its injection angle the two polarisations perceive a fraction of the input power equal to $P_{inx} = P_{in}\cos^2(\chi)$ and $P_{iny} = P_{in}\sin^2(\chi)$. This is illustrated in Fig. (4.1), in which we plot the steady states for the two polarisation intracavity power $P_{x,y}$ as function of the input power P_{in}, for three different injection angles χ in a monostable case $\phi_{0x} = -arg(H_x(0))$ and $\phi_{0y} = -arg(H_y(0))$. In Fig. (4.1) (a) $\chi = \pi/6$ (rad), meaning that the x axes receive more power that the y axes, and its steady states is indeed

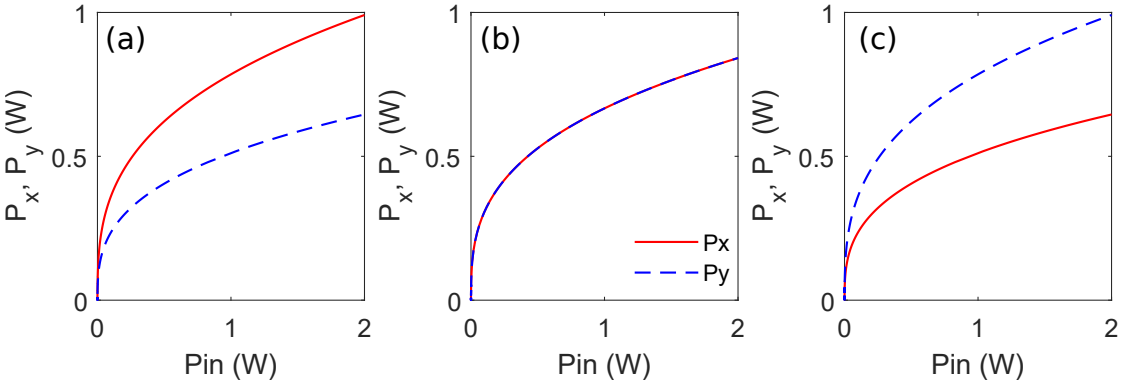

Figure 4.1 – Three examples of steady states in the monostable regime for the two axis of polarization. For all figures, the red traces are P_x and the blue dotted traces are P_y. In plot (a) the injection angle is $\chi = \pi/6$ (rad), in (b) is $\chi = \pi/4$ (rad) and in (c) $\chi = \pi/3$ (rad). The other parameters are: $L = 100\,m$, $\rho = \sqrt{0.95}$, $\theta = \sqrt{0.05}$, $\gamma = 2.5e^{-3}\,/W/m$, $\beta_2 = 0.5\,ps^2/Km$, $\phi_{0x,y} = -arg(H_{x,y}(0))$, $a = 85e9\,ns/rad$, $b = -2.45$, $f_{pump} = 194.12\,THz$ $f_{cx} = f_{cy} = 193.49\,THz$.

higher. In Fig. (4.1) (b) $\chi = \pi/4$ rad, the input power are exactly the same, and since all the other parameter are equals, the steady states are also equals. Finally, in Fig. (4.1) (b) $\chi = \pi/3$ rad, and it's possible to see that $P_y > P_x$.

By varying the linear phase detuning $\phi_{0x,y}$ of the two polarisations, one obtains the typical S-shaped bistable function. Fig. (4.2) (a) is an example of the steady states for $\chi = \pi/4$ rad and $\phi_{0x} = \phi_{0y} = -0.1$ rad. Given the injection angle, the power of the two steady states is the same. Fig. (4.2) (b), $\chi = \pi/4$ rad, but this time $\phi_{0x} = -0.1$ rad while $\phi_{0y} = 0.0$ rad. Clearly, the evolution no longer resembles the classical S-shaped function, because the two polarisations perceive two different detunings. In the next section, we will describe the stability analysis which allows to calculate the parametric gain.

4.2.2 Stability Analysis: Ikeda Map

Here we perform a stability analysis the system described by Eqs. (4.4) (4.5). First of all, we can define the following perturbed steady state at the n_{th} rountrip

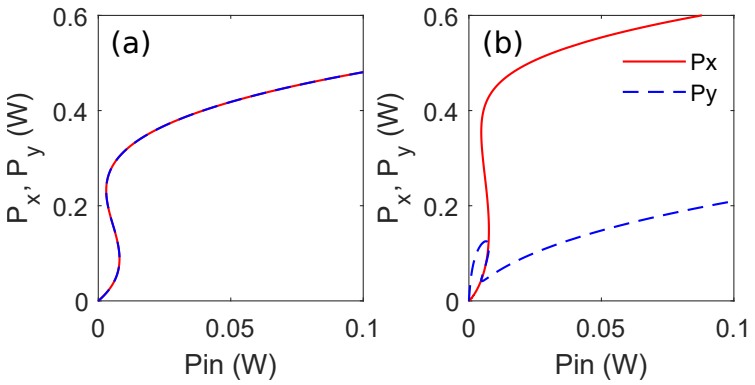

Figure 4.2 – Two example of bistable steady states. For all figures, the red trace is P_x and the blue dotted trace is P_y. In plot (a) the injection angle is $\chi = \pi/4$ (rad) and $\phi_{0x} = \phi_{0y} = -0.1$ (rad), in (b) is $\chi = \pi/4$ (rad) $\phi_{0x} = -0.1$(rad) while $\phi_{0y} = 0.0$ (rad). The other parameters are listed in the caption of Fig. 4.1

as:

$$E_x^n = (\sqrt{P_x}e^{i\zeta_x} + \eta_x^n(z,t))e^{\gamma P_1 z},\ |\eta_x^n| \ll \sqrt{P_x},$$
$$E_y^n = (\sqrt{P_y}e^{i\zeta_y} + \eta_y^n(z,t))e^{\gamma P_2 z},\ |\eta_y^n| \ll \sqrt{P_y}.$$

where we have defined $P_1 = (P_x + \sigma P_y)$ and $P_2 = (P_y + \sigma P_x)$, where $P_{x,y}$ and $\zeta_{x,y}$ are the powers of the steady state phases, respectively. By linearising, we find the following system that describes the evolution of the perturbations for each roundtrip n:

$$\frac{\partial \eta_x^n}{\partial z} = \Delta\beta_1 \frac{\partial \eta_x^n}{\partial t} - i\frac{\beta_2}{2}\frac{\partial^2 \eta_x^n}{\partial t^2} + i\gamma P_x(\eta_x^n + \eta_x^{*n} e^{i2\zeta_x}) + i\gamma\sigma\sqrt{PxP_y}(\eta_y^n e^{i(\zeta_x-\zeta_y)} + \eta_y^{*n} e^{i(\zeta_x+\zeta_y)}) \tag{4.10}$$

$$\frac{\partial \eta_y^n}{\partial z} = -\Delta\beta_1 \frac{\partial \eta_y^n}{\partial t} - i\frac{\beta_2}{2}\frac{\partial^2 \eta_y^n}{\partial t^2} + i\gamma P_y(\eta_y^n + \eta_y^{*n} e^{i2\zeta_y}) + i\gamma\sigma\sqrt{PxP_y}(\eta_x^n e^{i(\zeta_y-\zeta_x)} + \eta_x^{*n} e^{i(\zeta_y+\zeta_x)}). \tag{4.11}$$

By splitting the real and imaginary part of the two perturbations as $\eta_{x,y}(z,t) = a_{x,y}(z,t) + ib_{x,y}(z,t)$, and transform the result in the frequency domain $\hat{\eta}_{x,y}(z,\omega) =$

$\hat{a}_{x,y}(z,\omega) + i\hat{b}_{x,y}(z,\omega)$, the system can be rewritten in matrix form as:

$$\frac{\partial}{\partial z}\begin{pmatrix}\hat{a}_x^n(z,\omega)\\ \hat{b}_x^n(z,\omega)\\ \hat{a}_y^n(z,\omega)\\ \hat{b}_y^n(z,\omega)\end{pmatrix} = M\begin{pmatrix}\hat{a}_x^n(z,\omega)\\ \hat{b}_x^n(z,\omega)\\ \hat{a}_y^n(z,\omega)\\ \hat{b}_y^n(z,\omega)\end{pmatrix} \tag{4.12}$$

The components of the matrix are listed below. The notation $M_{i,j}$ element on the i_{th} row and j_{th} column:

$$\begin{aligned}
M_{1,1} &= i\Delta\beta_1 - \gamma P_x \sin(2\zeta_x) & M_{1,2} &= -\beta_2/2\omega^2 - \gamma P_x(1-\cos(2\zeta_x))\\
M_{1,3} &= -2\gamma\sigma\sqrt{P_x P_y}\sin(\zeta_x)\cos(\zeta_y) & M_{1,4} &= -2\gamma\sigma\sqrt{P_x P_y}\cos(\zeta_x)\cos(\zeta_y)\\
M_{2,1} &= \beta_2/2\omega^2 + \gamma P_x(1+\cos(2\zeta_x)) & M_{2,2} &= i\Delta\beta_1 + \gamma P_x \sin(2\zeta_x)\\
M_{2,3} &= 2\gamma\sigma\sqrt{P_x P_y}\cos(\zeta_x)\sin(\zeta_y) & M_{2,4} &= -M_{1,4}
\end{aligned}$$

$$\begin{aligned}
M_{3,1} &= -2\gamma\sigma\sqrt{P_x P_y}\sin(\zeta_y)\cos(\zeta_x) & M_{3,2} &= -2\gamma\sigma\sqrt{P_x P_y}\sin(\zeta_y)\sin(\zeta_x)\\
M_{3,3} &= -i\Delta\beta_1 - \gamma P_y \sin(2\zeta_x) & M_{3,4} &= -\beta_2/2\omega^2 + \gamma P_y(-1+\cos(2\zeta_y))\\
M_{4,1} &= -M_{1,4} & M_{4,2} &= -M_{1,3}\\
M_{4,3} &= \beta_2/2\omega^2 + \gamma P_y(1+\cos(2\zeta_y)) & M_{4,4} &= -i\Delta\beta_1 + \gamma P_y \sin(2\zeta_x)
\end{aligned}$$

By computing the exponential matrix of $M \times L$, with L the cavity length, one gets the *propagation matrix* $M_p = e^{M\times L}$, which contains the coefficients of the system that describes the evolution of the perturbed signal over one roundtrip. For clarity, we hide the dependency from the frequency, thus the system takes the

following form:

$$\begin{pmatrix} \hat{a}_x^n(L) \\ \hat{b}_x^n(L) \\ \hat{a}_y^n(L) \\ \hat{b}_y^n(L) \end{pmatrix} = M_p \begin{pmatrix} \hat{a}_x^n(0) \\ \hat{b}_x^n(0) \\ \hat{a}_y^n(0) \\ \hat{b}_y^n(0) \end{pmatrix}. \tag{4.13}$$

To complete the analysis, the system must be supplemented by the coupler matrix M_c and the filter matrix $M_f(\omega)$, as done for the single polarization case. In our model, filter and coupler does not couple the x and y components of the filter, they are described by two block-diagonal matrix that reads:

$$M_c = \rho \begin{pmatrix} \cos(\Phi_x) & -\sin(\Phi_x) & 0 & 0 \\ \sin(\Phi_x) & \cos(\Phi_x) & 0 & 0 \\ 0 & 0 & \cos(\Phi_y) & -\sin(\Phi_y) \\ 0 & 0 & \sin(\Phi_y) & \cos(\Phi_y) \end{pmatrix}, \tag{4.14}$$

$$M_f(\omega) = \begin{pmatrix} H_{ex}(\omega) & -H_{ox}(\omega) & 0 & 0 \\ H_{ox}(\omega) & H_{ex}(\omega) & 0 & 0 \\ 0 & 0 & H_{ey}(\omega) & -H_{0y}(\omega) \\ 0 & 0 & H_{0y}(\omega) & H_{ey}(\omega) \end{pmatrix}. \tag{4.15}$$

where $\Phi_x = \phi_{0x} + (P_x + \sigma P_y)\gamma L$, $\Phi_y = \phi_{0y} + (P_y + \sigma P_x)\gamma L$ accounts for the total phase accumulated over a roundtrip (excluding the filter phase shift), and $H_{ex,y}(\omega) = (H_{x,y}(\omega) + H^*_{x,y}(-\omega))/2$ and $H_{x,y}(\omega) = (H_{x,y}(\omega) + H^*_{x,y}(-\omega))/2i$ are the even and odd parts of the two polarisation components of the filter. The perturbation at round trip $n+1$ can be described by

$$\begin{pmatrix} \hat{a}_x^{n+1}(0) \\ \hat{b}_x^{n+1}(0) \\ \hat{a}_y^{n+1}(0) \\ \hat{b}_y^{n+1}(0) \end{pmatrix} = M_c \times M_f(\omega) \begin{pmatrix} \hat{a}_x^n(L) \\ \hat{b}_x^n(L) \\ \hat{a}_y^n(L) \\ \hat{b}_y^n(L) \end{pmatrix}. \tag{4.16}$$

By combining Eqs.(4.13) and Eqs. (4.16), one gets the complete model that allows to describe the propagation of the perturbed signal at the roundtrip $n+1$ as

function of the perturbation at the roundtrip n:

$$\begin{pmatrix} \hat{a}_x^{n+1}(0) \\ \hat{b}_x^{n+1}(0) \\ \hat{a}_y^{n+1}(0) \\ \hat{b}_y^{n+1}(0) \end{pmatrix} = M_p \times M_c \times M_f(\omega) \begin{pmatrix} \hat{a}_x^{n}(0) \\ \hat{b}_x^{n}(0) \\ \hat{a}_y^{n}(0) \\ \hat{b}_y^{n}(0) \end{pmatrix}. \tag{4.17}$$

The parametric gain is finally obtained by computing the four *eigenvalues* of the total matrix $M_p \times M_c \times M_f$. As for the simple MI cases, whenever $|\lambda_{1,2,3,4}| > 1$, the CW solution of the system is unstable and the power of the perturbations grows as $\exp(g_{MAP}(\omega)z)$, where the parametric gain is defined as

$$g_{MAP}(\omega) = \frac{2}{L} \ln \max |\lambda_{1,2,3,4}|. \tag{4.18}$$

Since the matrix is 4x4, it is possible in principle to obtain closed formulas for $g_{MAP}(\omega)$. However, the result will be very cumbersome, so we decided to compute the eigenvalue numerically.

We completed this semi analytical calculation of the parametric gain, by comparing it with the numerical simulation of full Ikeda map of Eq. (4.4) and (4.5).

The parametric gain express the growth rate of the power of the spectrum of the intracavity field, such that when $g(\omega) > 0$ the spectral component ω grows as $\exp(g(\omega)z)$. For small a propagation length $z = L_s$, when the perturbation are small enough, the ratio between the intracavity power at the length $z = L_s$ and the initial intracavity power at $z = 0$, corresponds to the growth rate of the spectrum. By computing the natural logarithm one basically obtain the parametric gain $g(\omega)$. This is a simple check that can be done to verify that the theoretical result of the gain correspond to the numerical solution of the model (Ikeda map or LLE).

Fig. 4.3 (a) and (b) are two plots of the ratio $\ln \frac{P_{x,y}(\omega,L_s)}{P_{x,y}(\omega,0)}/L_s$, compared to the parametric gain calculated with Eq. 4.18. Fig 4.3 (a) is for the negative frequencies, and (b) for the positive frequencies. The red trace is the growth rate of the x axes, the blue is growth rate for the y axes, while the green is the parametric gain trace. The $P_{x,y}$ are computed by numerical integration of Eq.

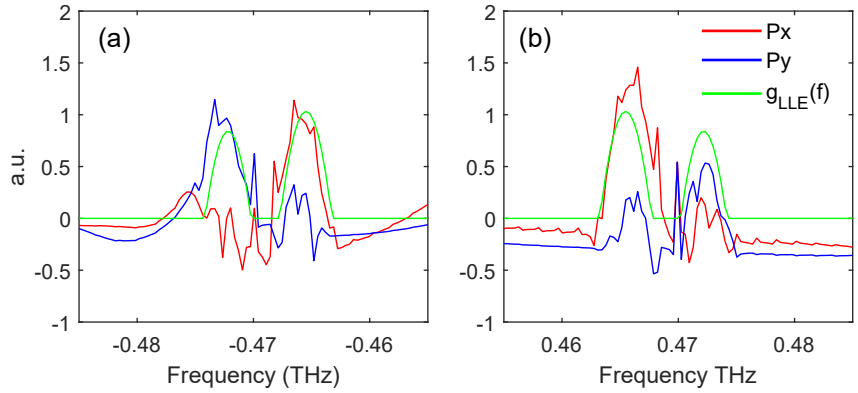

Figure 4.3 – Plot of the growth rate for the Ikeda map model. (a) plot of the negative frequencies; (b) plot of the positive frequencies. Blue traces are the y polarization axis, red are the x polarization axis. The green trace is the parametric gain. The parameter used are:$\rho = \sqrt{0.95}$, $\theta = \sqrt{0.05}$, $\gamma = 2.5\,/W/km$, $\beta_2 = 0.5\,ps^2/Km$, $\Delta\beta_1 = 0.5\,ps/Km$, $\chi = \pi/4\,rad$, $a = 85e9\,ns/rad$, $b = -2.45$, $f_{cx} = 193.49\,THz$, $f_{cy} = 193.4837\,THz$, round-trip number=300.

4.10 corresponding to 300 rountrips, and the parametric gain is computed with Eq.4.18. The red and blue traces, although slightly noisy, are very similar to the green trace. This suggests that the parametric gain correctly predicts the growth rate of the spectrum.

4.3 Lugiato Lefever Equations

The LLE approach can be useful to simplify the theoretical description and, most importantly, to speed up the numerical computation. Under the usual scope of the mean-field model [60, 116, 115], it's possible to obtain the following coupled LLE equations for the fast and slow axis:

$$\begin{aligned} L\frac{\partial E_x}{\partial z} =& [-\alpha + i\phi_{0x} + \Phi_x \star + i\Psi_x \star]E_x + \\ & \left[L\Delta\beta_1 \frac{\partial}{\partial t} - \frac{iL\beta_2}{2}\frac{\partial^2}{\partial t^2} + iL\gamma(|E_x|^2 + \sigma|E_y|^2)\right]E_x + \theta E_{inx}, \end{aligned} \tag{4.19}$$

$$
\begin{aligned}
L\frac{\partial E_y}{\partial z} =& [-\alpha + i\phi_{0y} + \Phi_y \star + i\Psi_y \star]E_y + \\
& \left[-L\Delta\beta_1 \frac{\partial}{\partial t} - \frac{iL\beta_2}{2}\frac{\partial^2}{\partial t^2} + iL\gamma(|E_y|^2 + \sigma|E_x|^2)\right]E_y + \theta E_{iny}.
\end{aligned} \tag{4.20}
$$

The losses are $\alpha = 1 - \rho$, and we assumed to be the same for both axes, as well as θ. $\phi_{0x,y}$ is the linear detuning of the two polarisation axes, $\Phi_{x,y}$ and $\Psi_{x,y}$ are the Fourier transform of the loss profile and phase of the filter, respectively. All other parameters are the same as described for the Ikeda map model.

4.3.1 Stationary Solution of the LLE

The steady CW solutions ($\frac{\partial}{\partial z} = 0$, $\frac{\partial}{\partial t} = 0$) of Eq.(4.19) and Eq.(4.20) to get the relation between the intracavity field and the power in the frequency domain:

$$E_{0x} = \frac{\theta E_{inx}}{(\alpha - i\phi_{0x} - F_x(0) - i\psi_x(0)) - iL\gamma(\bar{P_x} + \sigma\bar{P_y})} \tag{4.21}$$

$$E_{0y} = \frac{\theta E_{iny}}{(\alpha - i\phi_{0y} - F_y(0) - i\psi_y(0)) - iL\gamma(\bar{P_y} + \sigma\bar{P_x})} \tag{4.22}$$

$$\bar{P_x} = \frac{\theta^2 P_{inx}}{(-\alpha + F_x(0))^2 + (\phi_{0x} + \psi_x(0) + \gamma L(\bar{P_x} + \sigma\bar{P_y}))^2}, \tag{4.23}$$

$$\bar{P_y} = \frac{\theta^2 P_{iny}}{(-\alpha + F_y(0))^2 + (\phi_{0y} + \psi_y(0) + \gamma L(\bar{P_y} + \sigma\bar{P_x}))^2}. \tag{4.24}$$

The steady states solution are defined as $E_{0x,y} = \sqrt{\bar{P}_{x,y}}e^{i\zeta_{x,y}}$, with $\zeta_{x,y}$ being the phase of the steady states.

We show the dependency of the stable states of the two polarization axes as function of the injection angle in Fig. 4.4 for a monostable case and in Fig. 4.5 for a bistable case. As expected, in the monostable case, the angle of injection influences the amount of power that each polarization receive. In particular in Fig. 4.4 (a), for $\chi = \pi/6$, $P_x > P_y$, in Fig. 4.4 (b) $\chi = \pi/4$, $P_x = P_y$ and, finally in Fig. 4.4 (c), for $\chi = \pi/3$, $P_x < P_y$. The bistable case is characterized by the typical S-shaped in Fig. 4.5 (a), where $\chi = \pi/4$ and $P_x = P_y$ and the phase detuning is the same for both polarizations. In Fig. 4.5 (b), $\chi = \pi/4$ but the detuning is

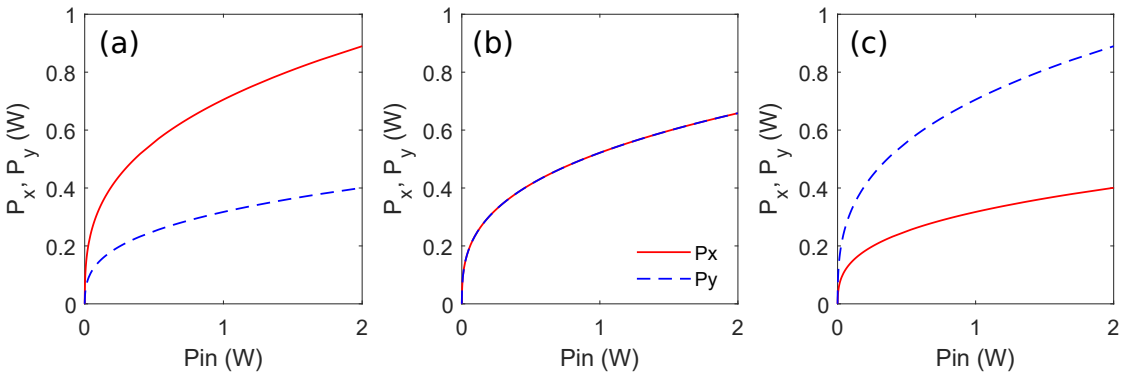

Figure 4.4 – Three examples of monostable steady states for the two axis of polarization, for the LLE model. Red traces are P_x and the blue dotted traces are P_y. In plot (a) the injection angle is $\chi = \pi/6$ (rad), in (b) is $\chi = \pi/4$ (rad) and in (c) $\chi = \pi/3$ (rad). The other parameters are: $L = 100\,m$, $\rho = \sqrt{0.95}$, $\theta = \sqrt{0.05}$, $\gamma = 2.5e^{-3}\,/W/m$, $\beta_2 = 0.5\,ps^2/Km$, $\phi_{0x,y} = -arg(H_{x,y}(0))$, $a = 85e9\,ns/rad$, $b = -2.45$, $f_{pump} = 194.12\,THz$ $f_{cx} = f_{cy} = 193.49\,THz$.

$\phi_{0x} = -0.1$ rad and $\phi_{0y} = 0$ rad, resulting in the odd shaped of P_x and P_y curves.

4.3.2 Stability Analysis of the LLE

The stability analysis is performed by considering the following perturbed steady states:

$$\begin{aligned} E_x(z,t) &= E_{0x} + E_x^+(z)e^{-i\omega t} + E_x^-(z)e^{i\omega t}, |E_x^\pm| << |E_{0x}|, \\ E_y(z,t) &= E_{0y} + E_y^+(z)e^{-i\omega t} + E_y^-(z)e^{i\omega t}, |E_y^\pm| << |E_{0y}|. \end{aligned} \tag{4.25}$$

In this case, we describe the additive perturbation as two space-dependent signals at $\pm\omega$, with a small amplitude $E_{x,y}^\pm$. By linearizing Eqs. (4.19) and (4.20) in the frequency domain, and separate the elements oscillating at $\pm\omega$, one gets the following matrix description:

$$\frac{\partial}{\partial z}\begin{pmatrix} E_x^+ \\ E_x^{*-} \\ E_y^+ \\ E_y^{*-} \end{pmatrix} = \begin{pmatrix} M_{1,1} & i\gamma L E_{0x}^2 & i\sigma\gamma L E_{0x}E_{0y}^* & i\sigma\gamma L E_{0x}E_{0y} \\ -i\gamma L E_{0x}^{2*} & M_{2,2} & -i\sigma\gamma L E_{0x}^* E_{0y}^* & -i\sigma\gamma L E_{0x}^* E_{0y} \\ i\sigma\gamma L E_{0x}^* E_{0y} & i\sigma\gamma L E_{0x}E_{0y} & M_{3,3} & i\sigma\gamma L E_{0y}^2 \\ -i\sigma\gamma L E_{0x}^* E_{0y}^* & -i\sigma\gamma L E_{0x}E_{0y}^* & -i\sigma\gamma L E_{0y}^{*2} & M_{4,4} \end{pmatrix}\begin{pmatrix} E_x^+ \\ E_x^{*-} \\ E_y^+ \\ E_y^{*-} \end{pmatrix}. \tag{4.26}$$

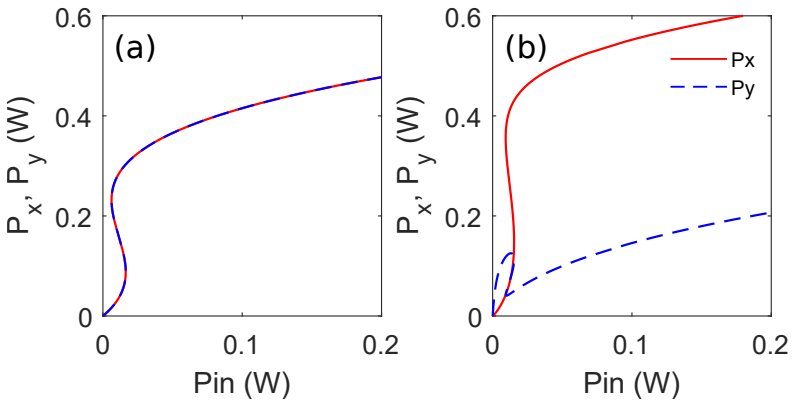

Figure 4.5 – Two example of bistable steady states for the LLE model.Red traces are P_x and the blue dotted traces are P_y. In plot (a) the injection angle is $\chi = \pi/4$ (rad) and $\phi_{0x} = \phi_{0y} = -0.1$ (rad), in (b) is $\chi = \pi/4$ (rad) $\phi_{0x} = -0.1$(rad) while $\phi_{0y} = 0.0$ (rad). For the other parameters see caption of Fig.4.4.

For sake of clarity, we define the elements of the diagonal of the matrix M below:

$$\begin{aligned}
M_{1,1} =& C_x(\omega)L - i\omega\beta_1 L + Li\omega^2\beta_2/2 + i\gamma L(2P_x + \sigma Py)\\
M_{2,2} =& C_x^*(-\omega)L - i\omega\beta_1 - Li\omega^2\beta_2/2 - i\gamma L(2P_x + \sigma Py)\\
M_{3,3} =& C_y(\omega)L + i\omega\beta_1 L + Li\omega^2\beta_2/2 + i\gamma L(2P_y + \sigma Px)\\
M_{4,4} =& C_y^*(-\omega)L + i\omega\beta_1 - Li\omega^2\beta_2/2 - i\gamma L(2P_x + \sigma Py)
\end{aligned}$$

where we have lumped together the following:

$$\begin{aligned}
C_x(\omega) =& [-\alpha + i\phi_{0x} + F_x(\omega) + i\psi_x(\omega))]/L;\\
C_y(\omega) =& [-\alpha + i\phi_{0y} + F_y(\omega) + i\psi_y(\omega))]/L;
\end{aligned}$$

The eigenvalues of the 4x4 matrix M can be efficiently calculated for each ω. Whenever one of the eigenvalues is positive, the respective frequency ω is unstable, and the amplitude of the oscillation will grows in spaces as:

$$g_{LLE}(\omega) = 2\max Re[\lambda_{1,2,3,4}(\omega)]/L \tag{4.27}$$

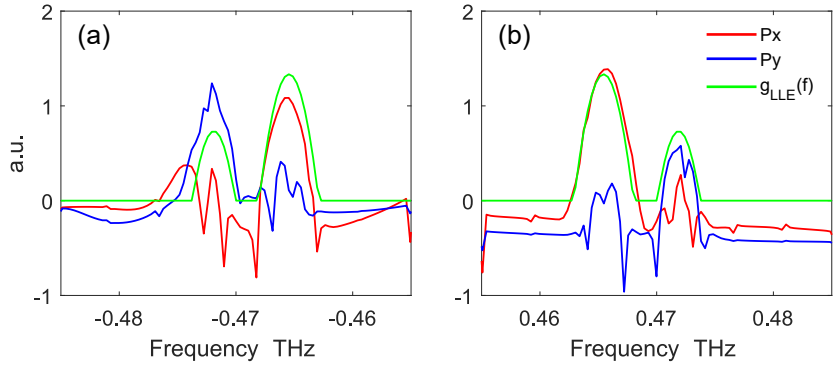

Figure 4.6 – Plot of the growth rate for the LLE model. (a) plot of the negative frequencies; (b) plot of the positive frequencies. Blue traces are the y polarization axis, red are the x polarization axis. The green trace is the parametric gain. The parameter used are:$\rho = \sqrt{0.95}$, $\theta = \sqrt{0.05}$, $\gamma = 2.5\,/W/km$, $\beta_2 = 0.5\,ps^2/Km$, $\Delta\beta_1 = 0.5\,ps/Km$, $\chi = \pi/4\,rad$, $a = 85e9\,ns/rad$, $b = -2.45$, $f_{cx} = 193.49\,THz$, $f_{cy} = 193.4837\,THz$, round-trip number=300.

To validate these theoretical results, we compare the parametric gain obtained with Eq. (4.27), with the growth rate of the integrated PM-LLE model. The results are shown in Fig. 4.3. Here, plots (a) and (b) refer to the negative and positive frequencies of the spectrum, respectively. The red traces is the growth rate for the x-polarisation axes while the blue traces are for the y-polarisation axes. The green trace is the gain calculated with Eq. (4.27). The agreement between the integrated growth rate and the theoretical gain is good, which means that the parametric gain correctly predicts the growth rate of the intracavity power.

4.3.3 Gain characterization: Ikeda and LLE models

In this section we characterise the parametric gain as a function of several parameters: the input power P_{in}, the injection angle χ, the relative frequency shift between the x and y filter components and the group velocity difference $\Delta\beta_1$. To keep the analysis as simple as possible, ρ and θ, γ, β_2, are kept identical for both polarisations. The linear phase detuning is defined as $\phi_{0x,y} = -arg(H_{x,y}(0))$ to compensate for the phase detuning imposed by the filters in the two polarisations. Only monostable cases are considered.

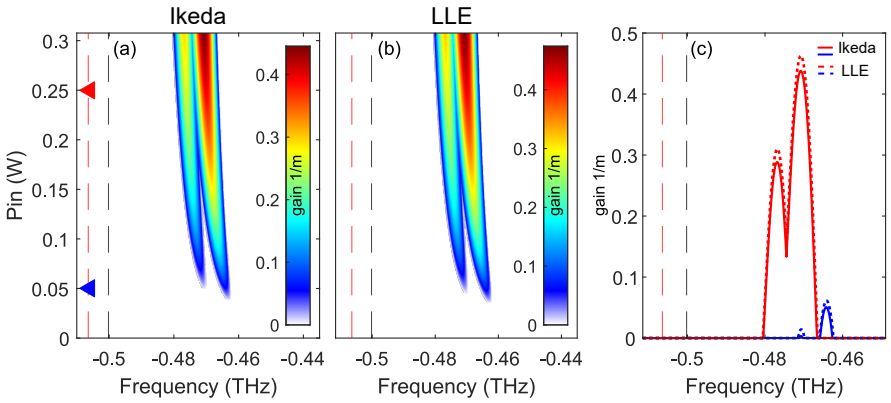

Figure 4.7 – (a)-(b) 2D plots of the evolution of the parametric gain as function of input power. (c) Examples of gains taken for $P_{in} = 0.05\ W$ (blue maker) and $P_{in} = 0.25\ W$ (red marker). The black and red dashed lines refer to the central frequency of the x and y components of the FBG respectively. The parameter used are: $L = 100\ m$, $\rho = \sqrt{0.95}$, $\theta = \sqrt{0.05}$, $\gamma = 2.5e^{-3}\ /W/m$, $\beta_2 = 0.5\ ps^2/Km$, $\phi_{0x,y} = -arg(H_{x,y}(0))$, $\Delta\beta_1 = 0.5\ ps/Km$, $a = 85e9\ ns/rad$, $b = -2.45$, $f_{cx} = 193.49\ THz$, $f_{cy} = 193.4837\ THz$. For the LLE model, $\alpha = 1 - \rho$.

We analyse here the parametric gain as function of the input power P_{in}, with the result shown in Fig. 4.7. In particular Fig. 4.7 (a) and (b) are 2D plots of the evolution of the gain bands for the negative frequencies for the Ikeda and LLE models, respectively (the positive side is symmetric). The dashed lines are the two central frequencies of the filter, red for the x polarization and black for the y.

For both models, we can clearly see two different sidebands, the position of which can be related to the two filter components. The sideband closer to the pump is slightly more pronounced than the other, and it can be seen that the LLE and Ikeda maps give the same qualitative results.

To better appreciate the difference between the two models, in Fig. 4.7 (c) we report two examples of gains taken at $P_{in} = 0.05\ W$ (blue curve) and $P_{in} = 0.25\ W$ (red curve), both for the Ikeda model in the solid line and the LLE model in the dashed lines. The LLE model predicts a gain that is slightly higher pronounced than the Ikeda Map model but, most importantly, the frequency corresponding to the peaks of the gain are the same for both models.

We continue this analysis, with the study of the gain as function of χ angle.

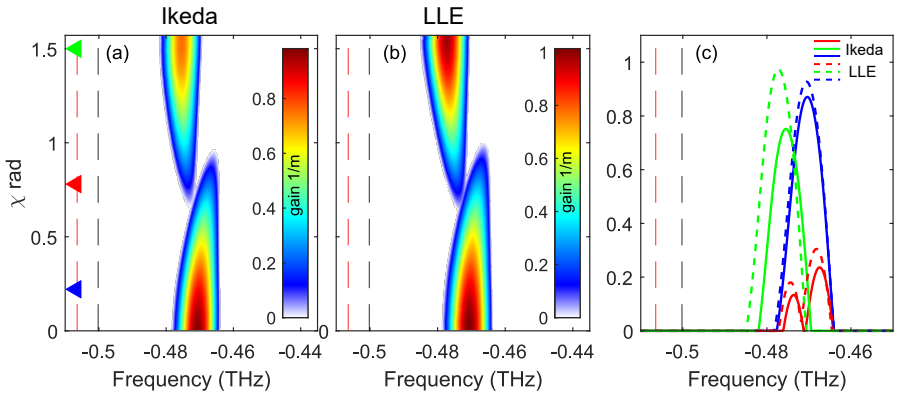

Figure 4.8 – (a)-(b) 2D plot of the evolution of the parametric gain band as function of the injection angle χ. (c) three examples of gain for $\chi = [0.2, \pi/4, 1.5]$ rad (blue, green and red trace respectively). The parameters used are: $L = 100\,m$, $\rho = \sqrt{0.95}$, $\theta = \sqrt{0.05}$, $\gamma = 2.5e^{-3}/W/m$, $\beta_2 = 0.5ps^2/Km$, $\phi_{0x,y} = -arg(H_{x,y}(0))$, $\Delta\beta_1 = 0.5\,ps/Km$, $a = 85e9\,ns/rad$, $b = -2.45$, $f_{cx} = 193.49\,THz$, $f_{cy} = 193.4837\,THz$ and a total input power $P_{in} = 0.15$ W. For the LLE $\alpha = 1 - \rho$.

Fig 4.8 (a) and (b) are 2D plots of the PM GTF gain for $\chi \in [0, \pi/2]$. The plots clearly show two distinct "tongues" that merge in the middle as the injection angle approaches $\chi = \pi/4\,rad$. This behaviour is quite intuitive: for example, at $\chi = 0$ rad, only the x axis are pumped, so only the x components of the fibre and filter receive power. As the χ angle increases, the y components start to become more important, up to the point where in the centre, for $\chi \approx \pi/4\,rad$, the gain manifests a "dual peak" feature. As χ approaches $\pi/2$, the y components become dominant and the parametric gain collapse on a single band, relative to the y axes of the filter. In Fig 4.8 (c) there are three examples of gains for both the Ikeda and LLE model, the latter corresponding to the dotted lines. The injection angles $\chi = [0.2, \pi/4, 1.5]$ rad correspond to the blue, red and green lines, respectively. The blue and green traces, are composed by singles parametric bands, while the red traces, relatives to $\chi = \pi/4$ rad, show a dual-peak feature.

The next case is the study of the gain as a function of the distance between the central wavelengths of the filters. Fig. 4.9 (a) and (b) are 2D plots of the gain as a function relative shift $\Delta_{\lambda c} = \lambda_{cx} - \lambda_{cy}$ within the interval $[-0.15, +0.15]\,nm$, for the Ikeda map and LLE model, respectively. In the calculation of the gain the central wavelength of the x-component of the filter λ_{cx} is fixed, while the

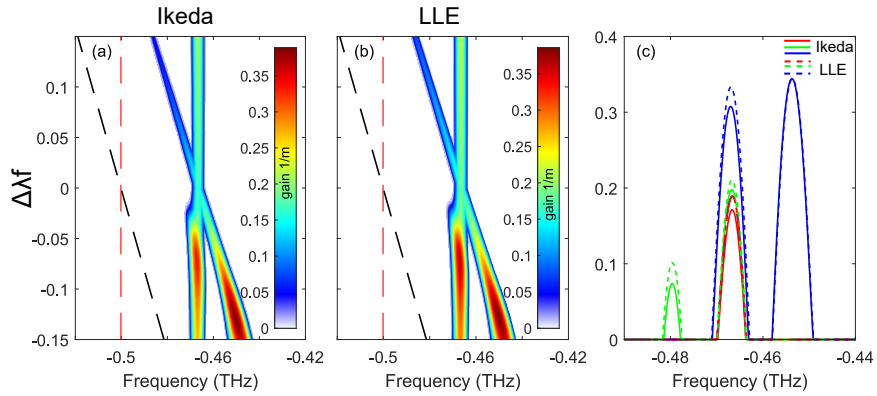

Figure 4.9 – (a)-(b) 2D plots of the parametric gain as a function of the shift between the central wavelengths of the filters, defined as Δ_{λ_c}. The black and red dashed lines represent the central position of the y and x components of the filter. (c) three examples of gain with $\Delta_{\lambda c} = [-0.1, 0, 0.1]\, nm$ for the blue, red and green trace respectively.The parameters are : $L = 100\, m$, $\rho = \sqrt{0.95}$, $\theta = \sqrt{0.05}$, $\gamma = 2.5e^{-3}\, /W/m$, $\beta_2 = 0.5\, ps^2/Km$, $\Delta\beta_1 = 0.5\, ps/Km$, $\phi_{0x,y} = -arg(H_{x,y}(0))$, $\chi = \pi/4\, rad$, $a = 85e9\, ns/rad$, $b = -2.45$, $f_{cx} = 193.49\, THz$, $f_{cy} = f_{cx} + \Delta\lambda_{fc}\, THz$ and $P_{in} = 0.1$ W.

y-component λ_{cy} is shifted. For reference, the red dashed line represents the x central wavelength, while the black dashed line represents the y central wavelength. As can be clearly seen from the 2D plots in Fig. 4.9 (a) and (b), the trajectory of the Ikeda and LLE gains follows the trajectory of the filter components. In Fig. 4.9 (c) we show three snapshots (solid lines for Ikeda and dotted lines for LLE) where $\Delta_{\gamma_c} = [-0.1, 0, 0.1]\, nm$ for the blue, red and green traces respectively. Again, the main difference between the LLE and Ikeda traces is the intensity of the bands. The position of the band is exactly the same for both models. This kind of dynamics is interesting because it is the PM equivalent of the tunability effect already described for GTF in [61]. In a real world scenario, this type of tunability effect can be achieved by applying physical stress to the FBG fibre, which results in a modification of the refractive characteristic and thus the relative frequency shift [120].

As last example, we study the gain as function of the group velocity mismatch $\Delta\beta_1$. Fig 4.10 (a) and (b) are a 2D plot of the parametric gain as a function of $\Delta\beta_1$ for the Ikeda and LLE model, respectively. Rather surprisingly, the GTF bands are not extremely effected by the value of the group velocity mismatch,

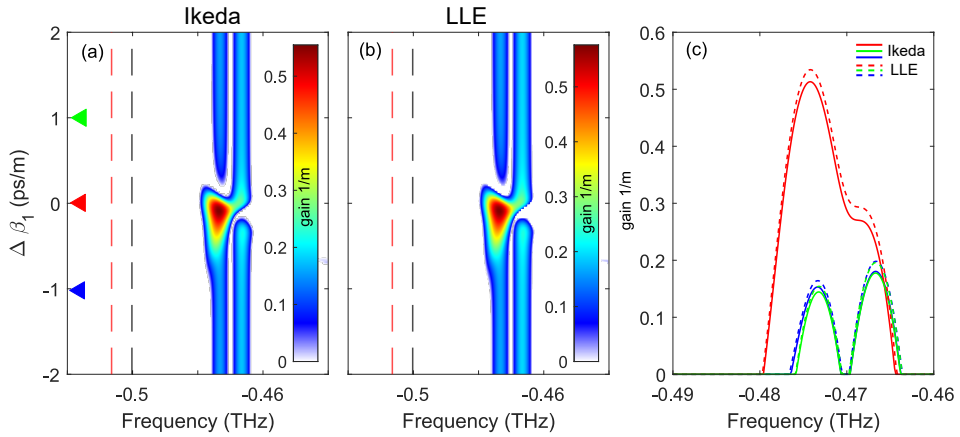

Figure 4.10 – (a) 2D plots of the GTF parametric gain as a function of the group velocity mismatch $\Delta\beta_1$. (b) Three examples of gain with $\Delta\beta_1 = [-1.5, 0, 1.5] ps/km$, for the blue, red and green traces respectively. The parameter are:$L = 100\, m$, $\rho = \sqrt{0.95}$, $\theta = \sqrt{0.05}$, $\gamma = 2.5e^{-3}\, /W/m$, $\beta_2 = 0.5\, ps^2/Km$, $\chi = \pi/4\, rad$, $a = 85e9\, ns/rad$, $b = -2.45$, $f_{cx} = 193.49\, THz$, $f_{cy} = f_{cx} + \Delta\lambda_f\, THz$ and a total input power $P_{in} = 0.1$ W.

once it get over a certain threshold. The plot 4.10 (c) are three example at $\Delta\beta_1 = [-1.5, 0, 1.5]\, ps/km$ for the blue, red and green trace, respectively. It's clearly visible how at the extremities, for opposite value of mismatch, the gain is actually symmetrical, while in the center, only a single and more intense band is present.

4.4 Passive dual frequency combs with PM GTF

In this section we characterise the PM GTF with a series of numerical simulations that show how it's possible to generate dual-frequency comb spectra. The simulations are performed by integrating the PM LLE of Eq. (4.19) and (4.20), which is as valid as the full Ikeda map under appropriate working conditions, but much faster to integrate with a split-step Fourier method.

The aim of this part of the study is to identify a set of conditions under which the spectra of the two polarisations develop sidebands with slightly different spectral positions. In particular, we will focus on three parameters: the injection angle χ, the relative frequency shift between the two components of the filter

Δ_{λ_f} and the group velocity mismatch $\Delta\beta_1$.

4.4.1 Numerical simulations: injection angle

The first case considered is the evolution of the spectra for different injection angle χ. The semi-analytical analysis performed in the previous section showed that the parametric gain develops a dual-peak structure depending on χ. It is therefore worth investigating how the actual spectrum evolves under these conditions. The results are summarised in Fig. 4.11. In particular, Fig. 4.11(a) shows the parametric gain as a function of χ computed with Eq. (4.27).

At the extremes of the interval analysed, $\chi = 0.7$ rad and $\chi = 1$ rad, the gain is characterised by a single band. In the interval $0.77 < \chi < 0.93$ rad, the gain bands overlap, producing the dual-peak profile.

In Fig. 4.11 (b) we superimposed the peak frequencies of the gain calculated for the 2D plot (a) (coloured 'x' and 'o' symbols) with the peak frequencies of the numerical simulation of PM LLE of Eq. (4.19) and Eq. (4.20) (blue solid lines for the y component and red solid line for the x component). For illustrate the effects of the injection angle, the plots in Figs. (c), (d), (e) and (f) show the spectral bands relative to the black markers in plot (b) at $\chi = [0.87, 0.82, 0.77, 0.746]$ rad, (red curves are the x-axis, blue curves are the y-axis). The yellow trace in the plots is the parametric gain relative to the same χ.

First of all, from the superposition of the theoretical and numerically simulated peaks of Fig. 4.11 (b) we can note that the theoretical model predicts the spectral bands with great accuracy. The only discrepancy is that the χ interval in which the parametric gain predicts the double peaks is not the same as the simulated one. In particular, the simulations show that the x and y components of the spectra have different peaks when χ is between 0.76 and 0.86 rad, while the theoretical results predict the double peak gain in the region $0.76 < \chi < 0.94$ rad. This is due to the imbalance between the amplitudes of the parametric gain peaks, which can be clearly seen in the 2D evolution of plot of Fig. 4.11 (a). If one of the two peaks is much more pronounced than the other, it will dominates and the x and y spectra will grow at the same frequency.

Finally, to better illustrate the characteristic of the spectra, we show some

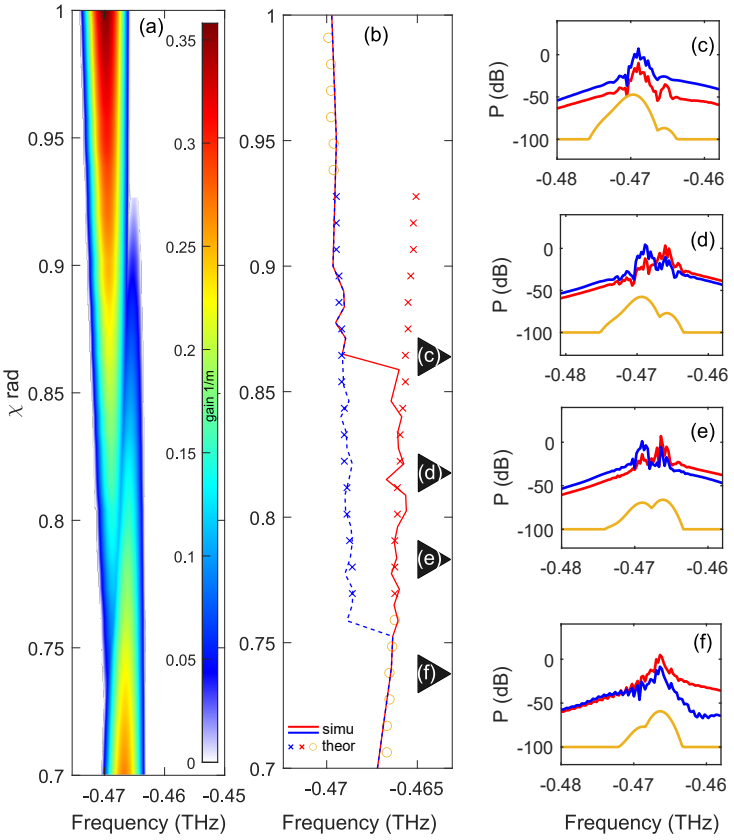

Figure 4.11 – (a) Evolution of the parametric gain as a function of the injection angle χ. (b) comparison between the peak positions of the parametric gain (colored symbols), and the numerical simulations peak positions (blue dashed lines for the y axes, red solid lines for the x axis). Finally, plots (c), (d), (e) and (f) are the negative spectral band for $\chi = [0.87, 0.82, 0.77, 0.746]\, rad$ respectively. The parameters are: $L = 100\, m$, $\rho = \sqrt{0.95}$, $\theta = \sqrt{0.05}$, $\gamma = 2.5\, /W/km$, $\beta_2 = 0.5\, ps^2/Km$,$\Delta\beta_1 = 0.5\, ps/Km$, $\phi_{0x,y} = -arg[H_{x,y}(0)]$, $P_{in} = 0.1\, W$, $a = 85e9\, ns/rad$, $b = -2.45$, $f_{cx} = 193.49\, THz$, $f_{cy} = f_{cx} + 0.25\, THz$.

specific examples (see the black marker in Fig. 4.11 (b)). In particular, in Fig. 4.11 (f) $\chi = 0.746$ rad, and the parametric gain shows a single band on the x-polarisation side, so both spectra grow accordingly. In Fig. 4.11 (e), where $\chi = 0.77$ rad, the two gain peaks are almost identical, with the x side slightly higher, and the spectra following the same evolution. In Fig. 4.11 (d) $\chi = 0.82$ rad, the opposite is true, the gain of the two components is high enough to get a double peaked spectrum, but the y component is more intense than the x side.

In Fig. 4.11(c),$\chi = 0.87$ rad, the y component of the gain is so intense that it overpowers the other and both axes develop a spectrum around this frequency.

In conclusion, we shown how the injection angle influences the formation of a double peaked parametric gain and how this is reflected in the spectra of the two polarisations.

4.4.2 Numerical results: filter central wavelengths

We will now analyse the dependence of the power spectra on the relative filter components position $\Delta_{\lambda f} = \lambda_{fx} - \lambda_{fy}$, where $\lambda_{f_{x,y}}$ are the central components of the filter. As explained earlier, assuming that a PM FBG is used as a filter, the x and y components generate two slightly detuned spectral losses due to the different refractive index of the polarisation axes. The relative spectral distance between the two components can be altered by applying physical stress to the filter [120].

In Fig. 4.12(a) we show the 2D plot of the LLE parametric gain of Eq. (4.27), in a $\Delta_{\lambda f} = \pm 0.02nm$. In particular, λ_{fx} is kept fixed and λ_{fy} is shifted. In the plot of Fig. 4.12 (b) we have compared the theoretical maxima of the parametric gain (yellow and black symbols) with the simulated maxima of the x and y components of the spectra (blue solid lines for the y polarisation and red solid line for the x polarisation).

Between -0.006 nm and 0.012 nm the parametric gain is composed of a single band (black '+' symbols in Fig. 4.12 (b)), as λ_{fx} and λ_{fy} are too close together to produce two distinct peaks, but the simulations still show the formation of two detuned peaks in the two polarisation axes.

The black marks, correspond to four examples of simulated spectra, in particular at intervals of $[0.015, 0.0016, -0.003, -0.015]$ nm for the plots of Fig. 4.12 (c), (d), (e) and (f), respectively.

In this case as well, the theoretical and numerical result are in good agreement. As predicted, the position of the bands on the x axes remains the same for each simulation, while the peak of the y axes moves accordingly with the shift of the filter. In the plots of Fig. 4.12 (c)-(f), one can appreciate the evolution in the gap between the two spectral peaks. When the spectra become very close

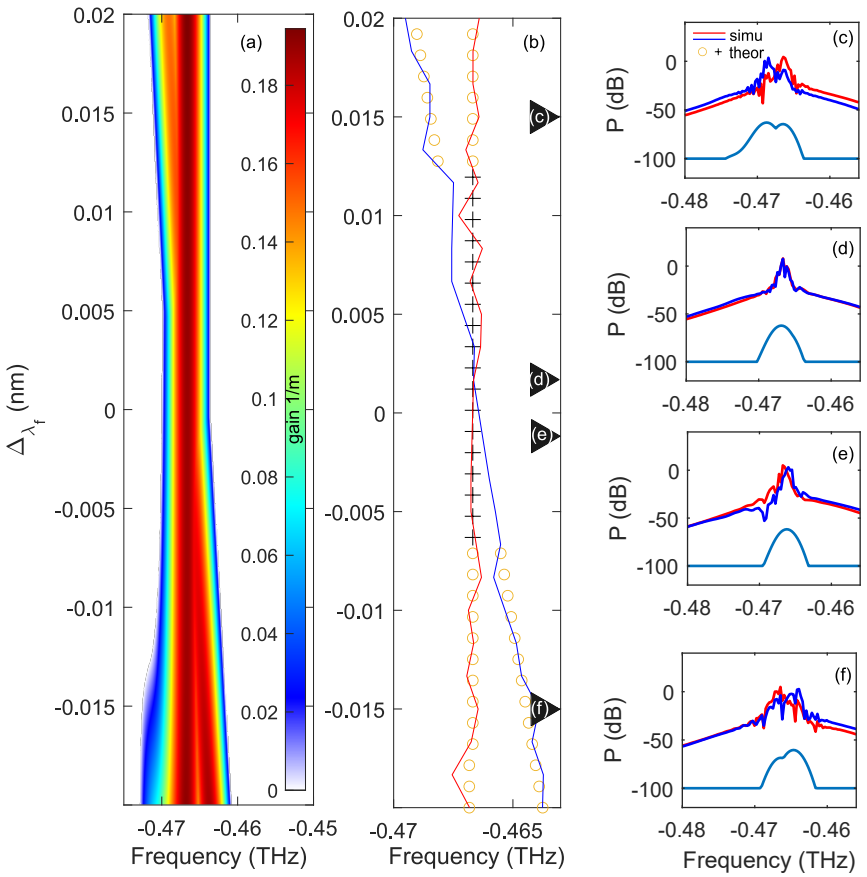

Figure 4.12 – (a) 2D evolution of the parametric gain band as a function of Δ_{λ_c} (b) Comparison between the theoretical gain peaks and the peaks of the simulated spectra. (c)-(f) examples of the first negative sidebands of GTF, for $\Delta_{\lambda_c} = [0.015, 0.0016, -0.003, -0.015]\, nm$, respectively. The red traces are the x polarization components, while blue traces are for the y polarization components. The parameters used are: $L = 100\, m$, $\rho = \sqrt{0.95}$, $\theta = \sqrt{0.05}$, $\gamma = 2.5\, /W/km$, $\beta_2 = 0.5\, ps^2/km$,$\Delta\beta_1 = 0.5\, ps/km$, $\phi_{0x,y} = -arg[H_{x,y}(0)]$, $P_{in} = 0.1\ W$, $a = 85e9\, ns/rad$, $b = -2.45$, $\lambda_{cx} = 193.49\, nm$, $\lambda_{cy} = \lambda_{cx} + \Delta_\lambda c\, nm$.

together, as in the case of plot (e), it can be useful to look at the interference pattern in the time domain.

If the spectra on the two polarisations grow at different frequencies, the period of the modulation in the time domain will also be different. Since it might be difficult to measure the difference between the periods of the two signals directly, one way to visualise this characteristic is to study the interference

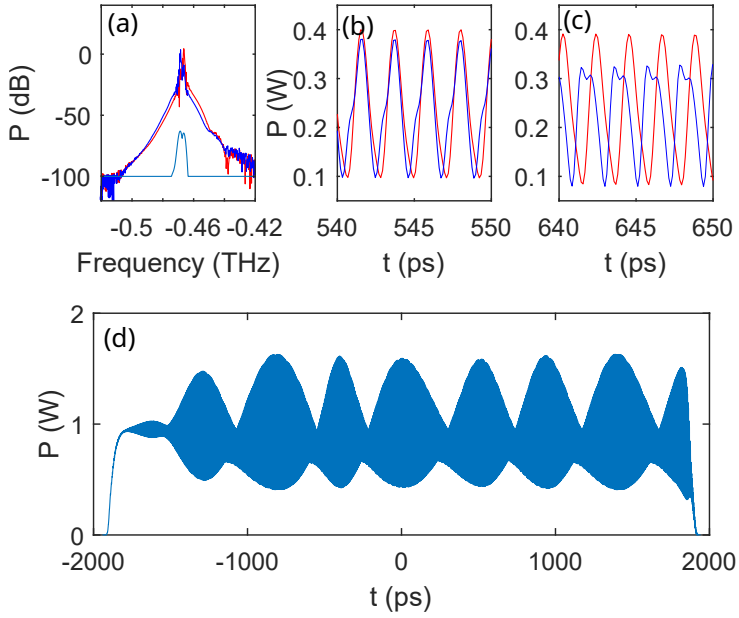

Figure 4.13 – (a) Examples of first sideband of the spectra, for $\Delta_\lambda = 0.015\,nm$. (b) and (c) are the delayed time windows of the time domain signal of the two polarizations. (d) is the respective interference pattern, where this time one can clearly see the modulation given by the beating of the two polarizations signals. The parameters are the same of Fig. 4.12.

pattern that the two signals produce when beaten together in the time domain. The x and y signals are coherent because they come from the same source. In a numerical simulation the interference pattern can be visualised by plotting $|E_x(t,z) + E_y(t,z)|^2$, and in a real experiment this can be done by simply beating the two signals on the same photodiode.

In Fig. 4.13 we show an example of time domain dynamics with $\Delta_{\lambda_c} = 0.015\,nm$, with spectra depicted in Fig. 4.12 (a). The plots in Fig. 4.13 (b) and (c) show the modulated time signal in two slightly delayed time windows of $10\,ps$. In windows (b), the red and blue signal (x and y polarization components) are perfectly synchronized and their frequency equal to the first harmonic of the MI spectra. In second window (c), the blue and red signals are delayed, which suggest a difference in the period of the two components. Fig. 4.13 (d) shows the interference pattern P_{int}. The over-modulation visible upon the signal has a period which is proportional to the period difference of the two

signals, as expected. In this case the spectral shift between the two spectra is $2.6\,GHz$, giving a interference pattern of with a mean period of $384\,ps$ which is $1/(2.6\,GHz)$.

One can see that the period is not very regular. This is due to the distortion of the two signals, visible for example in the blue trace of Fig. 4.13 (c). As stated before, the x and y components are always coupled through the XPM term $P_{x,y} + \sigma P_{y,x}$ in the model of Eqs. (4.19) and (4.20). This coupling brings to the presence of mutual spectral components in the two polarizations, which create a distortion in the pulse profile, thus in the interference pattern. We will discuss a brief solution to this problem in the Perspective section at the end of the chapter.

4.4.3 Numerical simulations: group velocity mismatch

In this last part we will analyse the effect of the group velocity mismatch.Fig. 4.14(a) is the 2D plot of the parametric gain as a function of $\Delta\beta_1$. The black crosses and yellow stars highlight the maxima of the gain. We can not that the the parametric gain is not symmetrical respect $\Delta\beta_1 = 0$, and the interval in which the gain has a single peak is between $\Delta\beta_1 = \pm 13.74\,ps/m$. This gives an interval where the $\delta\beta_1$ is too small to guarantee the formation of the dual frequency comb. In Fig. 4.14 we plot the evolution of the position of the peak of the x and y polarisations as and, as can be seen, the agreement with the theoretical model is good. As in the other cases analysed, there is a slight disagreement between the theoretical preliminary peak position and the simulated results, mainly due to the intensity of the parametric gain: when two peaks are present, the spectra tend to evolve around the highest gain peaks.

The plots of Fig. 4.14 (c), (d) and (e) are three examples taken for $\Delta\beta_1 = [0.47, -0.05, -0.47]: \; ps/m$ respectively, with the red traces being the x polarization components and the blue traces the y polarization components.

4.5 Perspective

At this stage, this remains a theoretical and numerical study, but it demonstrates that a passive dual-frequency comb like MI spectrum could be obtained by

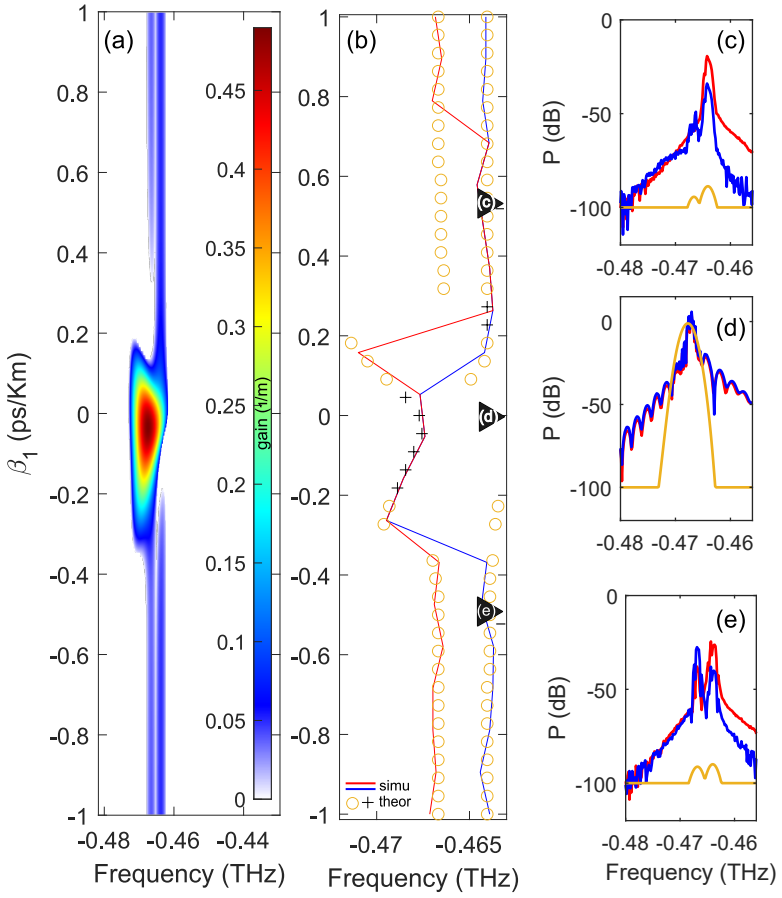

Figure 4.14 – (a) 2D plots of the parametric gain as a function of $\Delta\beta_1$. (b) comparison between the peaks of the gain, coloured symbols, and the numerical simulated peak (red lines for the x component, blue lines the y components). (c)-(e), three examples of spectra for $\Delta\beta_1 = [0.47, -0.05, -0.47]$: ps/m, respectively. The parameters are : $L = 100\,m$, $\rho = \sqrt{0.95}$, $\theta = \sqrt{0.05}$, $\alpha = 1-\rho$, $\gamma = 2.5e^{-3}/W/m$, $\beta_2 = 0.5\,ps^2/km$, $\phi_{0x,y} = -arg[H_{x,y}(0)]$, $P_{in} = 0.1\ W$, $a = 85e9\,ns/rad$, $b = -2.45$, $\chi = \pi/4$ rad $f_{cx} = 193.49\,THz$, $f_{cy} = f_{cx} + 0.25\,THz$.

exploiting the PM fibre characteristic with the GTF different degrees of freedom. In this work we have kept a "real world" realisation oriented approach, characterising some of the parameters that could be tested in a real experiment. This study is interesting because it could potentially overcome some of the intrinsic limitations of dual frequency comb generation, such as the fixed repetition rates of the lasers or fixed frequency shifts [123, 124, 125, 63].

This theoretical study opens the way to several experimental verifications.

First of all, it would be interesting to reproduce the dual-frequency comb generation with GTF. This could be done by adapting the experimental setup already described in Chap. 3 to handle two polarisations. This is technically challenging but feasible. Once the PM GTF is experimentally demonstrated, it would be possible to address some critical points. First, the XPM problem: the cross-polarisation components on the two axes create mutual interference that doesn't allow the generation of a clean pulse train (see Fig. 4.13). Secondly, the modulation obtained by GTF is almost sinusoidal, whereas dual-frequency comb generation usually requires sharper pulses.

The first problem could be solved by contrasting the cross-polarisation effect, e.g. by injecting two linearly polarised beams parallel to the x- and y-polarisation axes of the cavity. The generation of sharper pulses can actually be performed by MI [23]. Once the two optical frequency combs are generated and separated, the respective modulated pulses can be propagated in an appropriate fibre system, where they can act as seeds for MI. This can lead to the formation of a train of soliton, with a repetition rate equal to the original modulated frequency.

4.6 Summary

- In this chapter, we have analysed the theory of GTF in an all-polarization maintaining setup, which includes a PM cavity and a PM filter.
- Once defined the Ikeda Map model of the system, consisting of two coupled NLSE with the relative boundary conditions, we performed the calculation of the steady states and a stability analysis. The stability analysis doesn't bring to an analytical formula for the calculation of the gain, but can be easily resolved numerically.
- We derived the equivalent LLE model for the system, and performed a stability analysis which lead to a semi-analytical parametric gain model. We compared the Ikeda and LLE models, and found out that, under the appropriate conditions, they are basically equivalents. Given that, we focused on the LLE for the numerical simulations, because it substantially faster to use.

- We conducted a numerical study on the dependency of the PM GTF on different parameters of the filter: injection angle, spectral distance of the polarization components of the filter and polarization group-velocity mismatch. That analysis shown how it is possible to obtain dual-frequency structures inside the cavity, and that the frequency of the MI spectra on the two polarization axes can be controlled by the filters characteristic.

Chapter 5

Effects of pump-cavity synchronization mismatch

5.1 Introduction

In this chapter we discuss a central topic in the construction and use of fiber cavities, which is the effect of synchronization mismatch between the driving signal and the natural repetition rate of the cavity. In the experiment presented in chapter 3, as well as in a large number of works involving the use of fibre resonators [101, 74, 61, 82, 65], the cavity is driven by a pulsed signal.

This is due to two main necessities: (i) limiting the SBS and (ii) achieving a higher peak power. Indeed, the lossy nature of passive fibre resonators requires the use of relatively high peak power to stimulate non-linear effects. This latter characteristic, also allows a much higher conversion efficiency in the generation of optical frequency combs [52, 126, 127]. A pulsed pump requires very precise control of the repetition rate of the pulses in order to avoid degradation of the coherence and stability of the optical frequency combs [128, 129, 130]. To obtain a perfectly coherent drive, the repetition rate of the pulses must be an exact integer multiple of the free spectral range of the cavity, with a required accuracy in the order of hundreds of hertz. Such a requirement is not easy to meet, and a synchronisation mismatch between the cavity and the drive pump is expected. Therefore, studying the dependence of a phenomenon such as MI

from the synchronization mismatch is of primary interest in our studies, since pulsed driving is almost always our first choice.

So far, in the study of MI (see Chap. 2 and Chap. 3), we have only covered the contribution of the even order of dispersion, β_2. Higher orders of dispersion can become important as β_2 becomes small, and it has been shown how this can lead to drift instabilities in the time domain. This drift process can actually compete with the amplification process that allows MI to form, in a phenomenon known as convective instability [131, 84]. The contribution of the low odd-order dispersion term, β_1, which actually corresponds to the synchronisation mismatch between the driving pump and the cavity, is known to modify the resonator dynamics, but does not have a significant impact on the shape of the MI spectra.

With this study, made in collaboration with Saliya Coulibaly, MDC at Université de Lille, we show how the first-order dispersion actually leads to the modification of the position of the MI sidelobe. This fact is quite unexpected, because the standard stability analysis does not predict this before.

5.2 Theoretical analysis

The theoretical analysis is based on the LLE model, generalized in order to account for the group velocity mismatch $\Delta\beta_1$, reading:

$$i\frac{\partial E(z,\tau)}{\partial z}+i\Delta\beta_1\frac{\partial E(z,\tau)}{\partial \tau}-\frac{\beta_2}{2}\frac{\partial^2 E(z,\tau)}{\partial \tau^2}+\gamma|E(z,\tau)|^2E(z,\tau)=i\frac{\theta}{L}E_{in}+\Big(\delta-i\alpha\Big)\frac{E}{L}. \quad (5.1)$$

Following the formalism used in previous chapters, L is the length of the cavity, τ is the time reference, z is the distance travelled by the pulse, $E(z,\tau)$ is the intracavity electric field and E_{in} is the input electric field. γ is the Kerr nonlinearity parameter and β_2 is the group velocity dispersion. The group velocity mismatch is defined as $\Delta\beta_1 = \frac{t_R - t_{R,0}}{L}$, where t_R is the period of the input pulse train and $t_{R,0}$ is the natural repetition rate of the cavity $t_{R,0} = nL/c$, c being the velocity of light in the void. With this definition, $\Delta\beta_1$ represents the difference between the repetition rate of the drive pulse train and the actual repetition rate of the cavity. The parameters θ and ρ are the transmission and reflection parameters of the cavity, and $\alpha = 1-\rho$ accounts for the total losses. $\delta_0 = -\phi_0$ is the linear phase

detuning between the cavity and the laser.

We can write the steady state solution of Eq. 5.1, as $E_s = \sqrt{I_s}e^{\phi_s}$ such that $S^2 - I_s[\alpha^2 + (\delta - I_s)^2] = 0$ [105]. A perturbation in the form of $e^{i(\omega t - \lambda z)}$ gives the following dispersion relation:

$$D(\lambda, \omega) = (\lambda - \Delta\beta_1\omega + i\alpha)^2 + [I_s^2 - (\omega^2 + \delta - 2I_s)^2]^2. \tag{5.2}$$

It is possible to compute the eigenvalue λ by simply solving $D(\lambda, \omega) = 0$. The steady state solution is then stable if the imaginary part of the following λ is negative:

$$\lambda(\omega) = \Delta\beta_1\omega + i[-\alpha + \sqrt{I_s^2 - (\omega^2 + \delta - 2I_s)^2}]. \tag{5.3}$$

At this point, the position of the MI can be easily found by solving $\mathrm{Im}[(\delta\lambda/\delta\omega) = 0]$, which gives $\omega_{MI} = \sqrt{2I_s - \delta}$. The corresponding phase velocity is $v_\phi = Re(\lambda)/\omega = \Delta\beta_1$. Eq. (5.3) has to be fulfilled to get MI, but, since the gain depends on the imaginary part of λ, the effect of $\Delta\beta_1$ is not evident by only looking at this formulations.

To get a more complete description of the dynamic of a system pumped with pulses, the linear stability analysis must be considered through the determination of the linear response of the system [132, 133]. In practice, if one define the initial perturbation (pump) as $S(\gamma, \omega)$, the linear solution can be computed with an inverse Fourier-Laplace integral as[133]:

$$E_{lin}(\tau_0 + b_1 z, z) = \int_{-\infty}^{+\infty} d\omega \int_{i\sigma-\infty}^{i\sigma+\infty} \frac{S(\lambda + \Delta\beta_1\omega, \omega)}{D(\lambda + \Delta\beta_1\omega, \omega)} \times e^{i(\omega\tau_0 - \lambda z)} d\lambda \tag{5.4}$$

where τ_0 is the time in the absolute reference frame, and b_1 is the velocity at which the perturbation is moving respect the absolute reference frame, and σ defines a contour of integration in which the frequency is grater that the maximum growth rate of the perturbation, $\sigma > \sigma_m = \max\{\omega_i | D(\lambda, \omega) = 0, -\infty < \lambda < +\infty\}$. For large enough intervals, the integrals of Eq. (5.4) are dominated by the saddle points $\omega = \omega_s$ and $\lambda = \lambda(\omega_s)$ which satisfy [131]: $D(\lambda + \Delta\beta_1\omega, \omega)|_{\omega_s} = 0$ and $\frac{\partial D(\lambda + \Delta\beta_1\omega, \omega)}{\partial\omega}|_{\omega_s} = 0$. By evaluating the linear response solution of Eq. (5.4), it is possible to depict the effect of $\Delta\beta_1$ on the parametric gain.

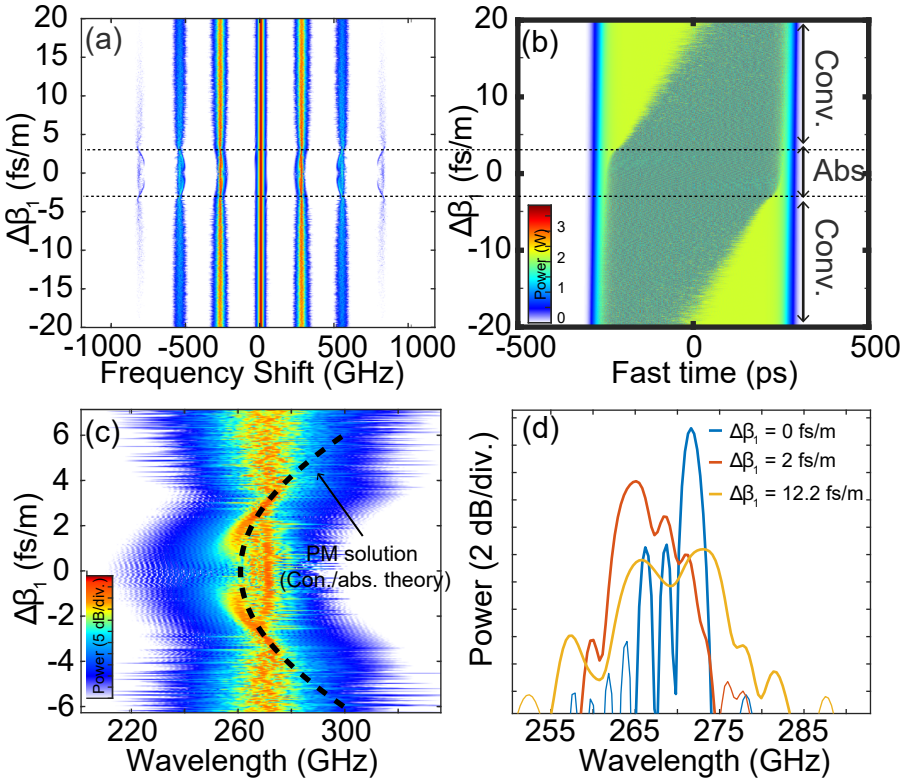

Figure 5.1 – (a) Evolution of the output spectrum as a function of the group velocity mismatch ($\Delta\beta_1$) from numerics [LLE integration, Eq. (1)]. (b) Evolution of the output power as a function of the group velocity mismatch. (c) Zoom on a MI sidelobe. The black dashed lines represent theoretical predictions from Eq. (5.3)-(5.4). (d) Zoom in on the MI sidelobe for different mismatch values (0, 2, 12 fs/m respectively from numerics).

Figure 5.1 (a) is the 2D plot of the output spectra as a function of the synchronisation mismatch in an interval of ±20 fs/m, obtained by integrating the LLE of Eq. (5.1), with parameters corresponding to the experiment. When the synchronisation mismatch is higher than ±5 fs/m, the MI sidebands does not change position respect $\Delta\beta_1$, and remain located at ±270 GHz from the pump.

When the synchronisation mismatch is $|\Delta\beta_1| < 5$ fs/m, the sidebands move towards the pump as the mismatch decreases, see Fig. 5.1 (c) for a zoom on the first sideband. The trajectory is parabolic, moving from 270 GHz to 260 GHz in the minimum. When $\Delta\beta_1 = 0$ fs/m, the bands move back to the initial position of 270 GHz, creating the hole in the parabolic evolution. It's also interesting to

note the difference in the width of the sidebands, which are significantly thinner at these intervals than at larger $\Delta\beta_1$, as shown in Fig. 5.1 (d).

The evolution of the band is due to the transition from a so-called convective regime to an absolute regime, which can also be better appreciated by looking at the time-domain evolution of the perturbation in Fig. 5.1 (b). In the convective regime, when $|\Delta\beta_1| > 5$ fs/m, the MI perturbation is shifted outside the pulse as the synchronisation mismatch becomes larger. Eventually, the entire perturbation is shifted out of the driving pulse and the MI sidebands disappear (not shown here for clarity). On the contrary, $|\Delta\beta_1| < 5$ fs/m, the perturbation covers the entire pulse (absolute regime), and the movement of the bands follows the round-trip-to-roundtrip shift of the modulation.

The trajectory of the sidebands in the absolute regime can be calculated from Eqs.(5.3)-(5.4). In Fig. 5.1(c) it's superimposed on the numerical simulation, black dashed line, with a good agreement in the parabolic motion followed by the sideband.

The physical interpretation of the movement of the MI bands can be understood by considering that the phenomenon is observed in a fixed reference frame respect the MI perturbation. Indeed, if an observer travels in the same reference frame of the perturbation (at the same velocity of the pulse), he wouldn't see any change in the modulation frequency. But by looking the phenomenon from a fixed reference frame, different from the one of the moving pulse, by changing the velocity of pulse (thus the synchronization mismatch of the pump), the observer would see the frequency of the modulation change as the synchronization mismatch.

There is a small discrepancy in the total duration of the absolute regime, theoretically present from ±6 fs/m, but numerically visible only for $|\Delta\beta_1| < 4$ fs/m. This may be due to non-linear effects not considered in the space-time analysis (the power of the perturbation is always considered weak compared to the power pump in the stability analysis). Another small discrepancy between the theoretical result and the numerical simulation is the presence of a fixed frequency component around 270 GHz, which creates a sort of "halo".

In Fig. 5.2 we have plotted the evolution of the trajectory of the first sideband in the absolute regime as a function of cavity detuning δ and pump power. In

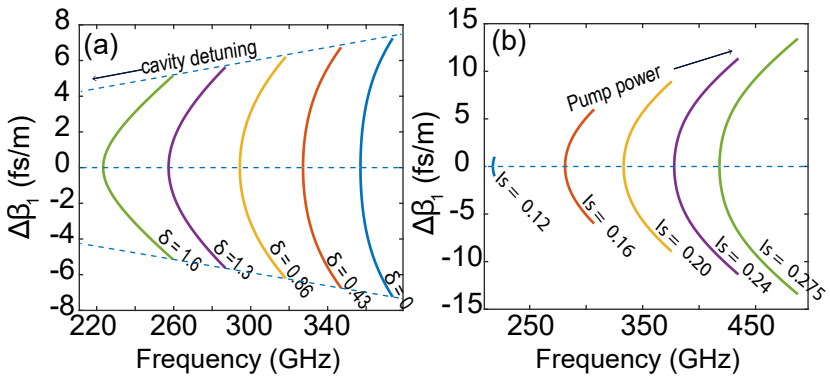

Figure 5.2 – (a) and (b) Evolutions of the sidelobe positions and of the absolute regime zone as a function of the cavity detuning and the pump power, respectively, from theory Eq. (5.3)-(5.4). With $\alpha = 0.2327$, $\theta = 0.05$, and $|E_{in}|^2 2 = 2.3$ W, extracted from experimental parameters which are all listed in Fig. 5.3's caption.

particular, in Fig. 5.2 (a) one can see how, at higher detuning, the sidebands generally rise closer to the pump, with a more pronounced parabolic motion. It's also noticeable how the absolute instability zone becomes larger for smaller detunings. The evolution with power is shown in Fig. 5.2(b): as the power increases, the area of the absolute regime becomes larger.

5.3 Experimental Setup

The setup used for this experiment is shown in Fig. 5.3. The cavity is made up of a dispersion-shifting fibre with a dispersion $\beta_2 = -4.5\, ps^2/km$ at 1545 nm, a nonlinear coefficient $\gamma = 2.5\, W^{-1}km^{-}1$ and a 90/10 coupler, also made with the same fibre type. The total length is $L = 27.44$ m, with a finesse of 15.6. Inside the cavity, a polarisation controller (PC3) is used to change and fix the phase detuning. This is achieved by cross-polarising the drive and control signals on the two polarisation axes of the cavity. The PC3 then imposes a physical deformation on the fibre, which changes the refractive index on the two polarisation axes and thus the phase detuning between the drive and control signals. A mechanical stretcher is also placed inside the spool to finely vary the length of the cavity and thus control the synchronisation mismatch. It should be noted that the use of the stretcher also changes the phase detuning, which has to be reset each

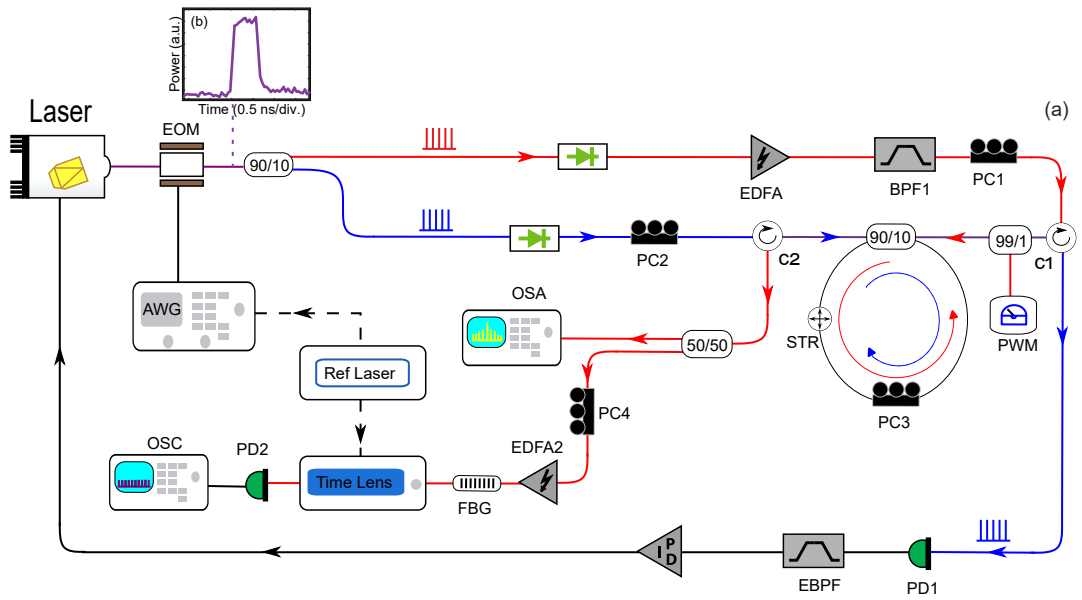

Figure 5.3 – (a) Experimental setup. EOM, electro-optical modulator; PC (1-4), polarization controllers; PD, photodetector; OSA, optical spectrum analyzer; EDFA, erbium-doped fiber amplifier; BPF1, optical bandpass filter; EBPF: electronic bandpass filter; STR: fiber stretcher; Ref Laser: femtosecond laser; OSC, oscilloscope; PID, proportionalintegrate-derivate controller; FBG, fiber Bragg grating; PWM, power meter; AWG, arbitrary wave generator. Parameters: pulse width = 560 ps, L = 27.44 m,γ= 2.5 /W/km, $\beta_2 = -4.5\, ps^2/km$, finesse of 15.6, PP = 2.3W, Δ = 1, and the zero mismatch repetition rate 7.431 555 16 MHz. The delay accumulated after one round trip when the pump pulse train has a synchronization mismatch with the cavity of ΔT = 1/FPump - 1/F' Pump. (b) Typical pump pulse from experimental recordings

time. Two circulators allows to inject the counterpropagative driving and control fields, without the need of a tap coupler. The CW laser is modulated into pulses of 560 ps by an electro-optical modulator (EOM) controlled by an AWG, which allows the repetition rate of the pulses to be fine-tuned. The pulse train is then split into two beams. The non-linear driving field, in red, passes through an isolator, a fibre amplifier (EDFA1) and a band-pass optical filter (BPF1). Its polarisation can be controlled by a paddle controller (PC1) and then a circulator (C1) directs it into the input/output 90/10 coupler. Note that before injection, a small part of the power is collected for power measurement. In the same way, the control beam, the blue path, passes through an isolator and a polarisation

controller (PC1) before being directed into the cavity with a circulator (C2).

The nonlinear and control beams are extracted from the cavity by the same circulators used for injection. In particular, the control beam leaves the cavity through C1, where it is collected by a photodiode (PD1). As it is still a pulsed signal, it is processed through an electrical bandpass filter before being fed to the PID controller. The PID produces the error signal that drives the CW laser, closing the feedback loop that stabilises the cavity.

The non-linear beam exits the cavity through (C2) and undergoes a different type of processing. In fact, 10% of the total output power is directed to the OSA for spectral recording. The remaining part passes through an additional polarisation controller (PC4), is amplified (EDFA2) and then processed with an FBG to suppress the carrier of the spectrum. The signal obtained is processed with a *time lens* system, which allows the time domain signal to be stretched without distortion. The time stretching effect was obtained by pumping the time lens with a femtosecond laser centred at 1570 nm, providing pulses with a fixed repetition rate of 99.88 MHz. This laser was used as the reference clock for all the electronics in the setup. The magnified signal (magnification factor 57) was recorded by a fast photodiode and an oscilloscope (70 GHz bandwidth each). With this time-lens system, we were able to record the real-time evolution of the output cavity field over a window of 40 ps with a resolution of about 300 fs.

In this setup, there are two ways to vary the synchronisation mismatch: by the frequency of the AWG or by the stretcher (STR) placed inside the cavity. The first method is very straightforward and allows very fine tuning of the mismatch. In fact, changing the pump repetition rate by as little as 1 Hz results in a sync delay of 19.8 fs (a synchronisation mismatch of 0.7 fs/m). We therefore used a highly stable frequency synthesiser to tune the repetition rate by only a few Hz around a reference repetition rate with zero mismatch, which we measured at 7.111 231 MHz (at 1545 nm).

The second method is to vary the length of the cavity using a mechanical stretcher. This choice was made because it allowed the synchronisation between the AWG and the timelens system to be maintained, while changing the synchronisation between the cavity and the driving field. With this method we were able to tune the mismatch roughly around ±20 fs/m to study the round-trip to

round-trip time drift of the modulated pulses.

5.4 Experimental Results

As a first result, we show the overall evolution of the spectra as a function of the synchronisation mismatch. For these measurements, we varied the repetition rate of the pulses. The synchronisation mismatch was tuned at an interval of ±250 fs/m, corresponding to a total repetition rate variation of 756 Hz. By pumping the cavity above the MI threshold, we obtain the formation of sidebands in the interval of ±150 fs/m, corresponding to a mismatch of ±4.05 ps, respecting perfect synchronisation. This means that a desynchronisation of 0.7% is sufficient to stop the process completely.

The overall evolution is shown in the 2D plot of Fig. 5.4 (a), and Fig. 5.4 (b) and (c) are zooms on the harmonics of the spectral evolution. From the overall 2D plot of Fig. 5.4 (a), it can be seen that the MI spectrum is almost symmetric with respect to the zero mismatch value $\Delta\beta_1 = 0$. The slight asymmetry observed is due to a slow drift of the experimental parameters over the entire acquisition time, which exceeds 15 min. Therefore, for simplicity, only the positive mismatch interval will be analysed. In the plot of Fig. 5.4 (d) we have plotted different spectra for specific $\Delta\beta_1$ values, corresponding to the coloured triangles in the panels 5.4 (a) and (c). The case of perfect synchronisation ($\Delta\beta_1 = 0$) shows a set of two narrow symmetrical sidebands (10 GHz at FWHM) located at 280 GHz from the pump, as seen in the cyan trace of Fig. 5.4 (d). By slightly increasing the detuning to $\Delta\beta_1 = 2$ fs/m, the sidelobes move towards the pump at about 250 GHz, keeping the same shape as shown in the red trace of Fig. 5.4 (d). By increasing the detuning further, the bands start to move back to the original position, up to 280 GHz at $\Delta\beta_1 = 5$ fs/m. The black dotted line in Fig. 5.4(c) represents the theoretical position of the bands as calculated in the previous sections, and it is quite a good agreement, confirming that the displacement of the bands is due to the synchronisation mismatch.

Finally, the green and black traces of Fig. 5.4 (d) are two spectra in the "convective regime" and, as explained before, they don't manifest any particular changes in position and simply disappear when the synchronisation mismatch

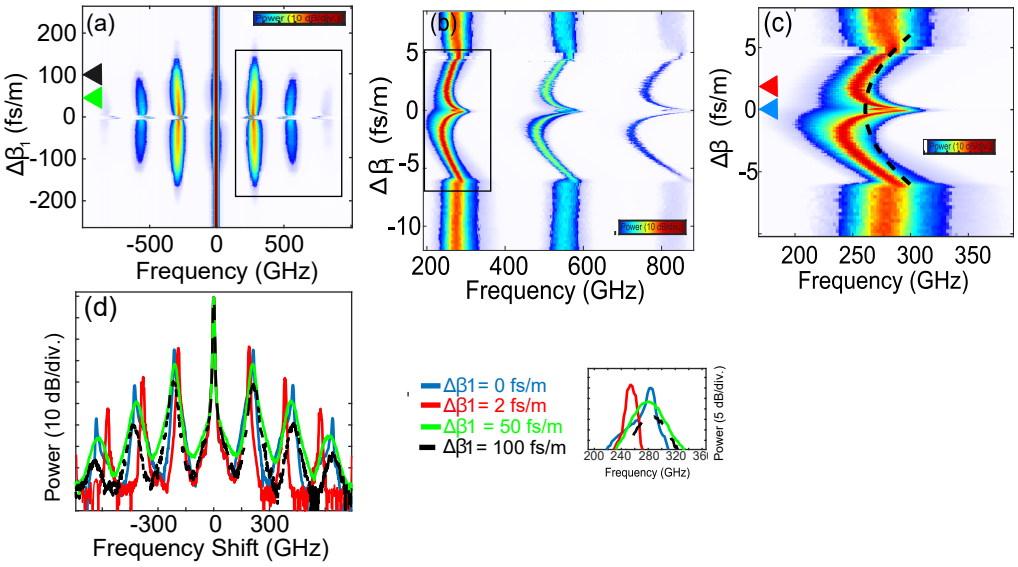

Figure 5.4 – (a) Two-dimensional (2D) plot of the output spectra as a function of the synchronization mismatch. (b)-(c) Progressive zoom on the harmonics and the central part of the first sidelobe. (d) Output spectra for specific values of $\Delta\beta_1$ (0, 2, 50, and 100 fs/m). Inset: Zoom on the first sidelobe.

becomes too high.

In the time domain, the effect of the synchronization mismatch can be seen through a drift of the ripples of the modulated pulses. Thanks to the use of a time lens system, we were able to record the dynamic of the MI from roundtrip to roundtrip. In particular, we were able to record the pulse train at the output of the cavity, that manifest a modulation with a period of 4 ps, with a very high temporal resolution (300 fs).

Five typical recordings of the real-time evolution of the output cavity are shown in Fig. 5.5 (a)-(e). In particular, Fig. 5.5 (c) is an example taken for a perfect synchronization case: we can see that the modulated signal is straight from round-trip to round-trip, and its period is ≈ 3.2 ps. At this point, acting on the stretcher of the cavity one can observe how negative synchronisation mismatches produce a negative slope in the modulation, see Figs. 5.5 (a) and (b), while positive synchronisation mismatches produce a positive drift, as in Figs. 5.5 (d) and (e). In Fig. 5.5 (f) we have plotted the evolution of the drift as a function of the synchronisation mismatch. The drift can be considered as the

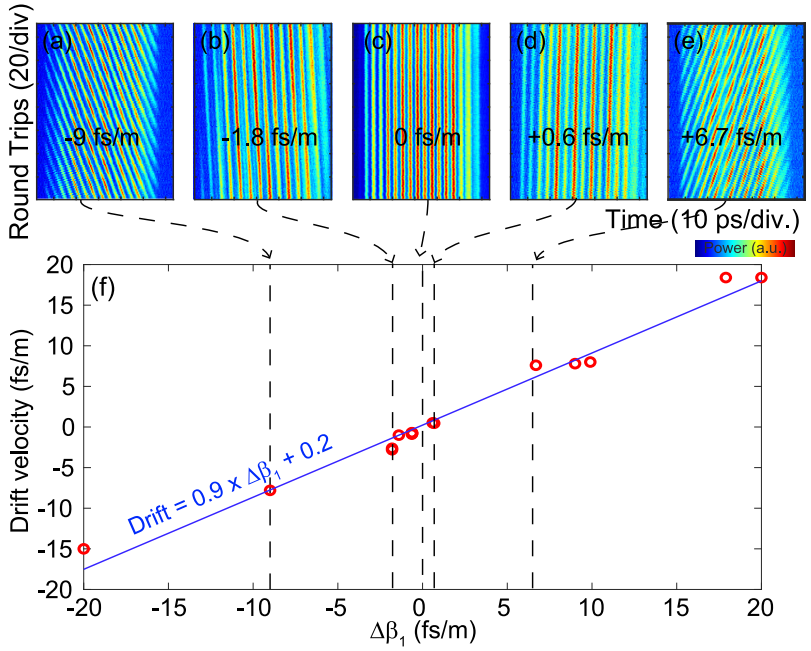

Figure 5.5 – (a)–(e) Round-trip to round-trip temporal trace evolution for three specific values of $\Delta\beta_1$ (-9, -1.8, 0, 0.6, and 6.7 fs/m). (f) Temporal drift of the pattern vs $\Delta\beta_1$.

variation of the phase velocity of the driving pulses and is in particular equal to $\mathcal{V}_\phi = Re[\partial_\omega \lambda] = \Delta\beta_1$ (see eq. (5.3)). From the measurements we have measured the drift, and its slope as a function of $\Delta\beta_1$ is 0.9, which is remarkably close to the theoretical value of 1.

In conclusion, we demonstrated how the synchronization mismatch influences the dynamic of modulation instability. The effect can be appreciated in two different way: first of all the dependency of the position of the side-lobe of the MI spectra from the synchronization mismatch in the absolute regime area and, secondly, the round-trip to round-trip time drift of the modulated pulses.

5.5 Perspective: Synchronization and GTF

The previous results showed the effects of the synchronisation mismatch on the MI spectra. In particular, we have described the competition between the absolute and convective regimes, in which the position of the bands changes

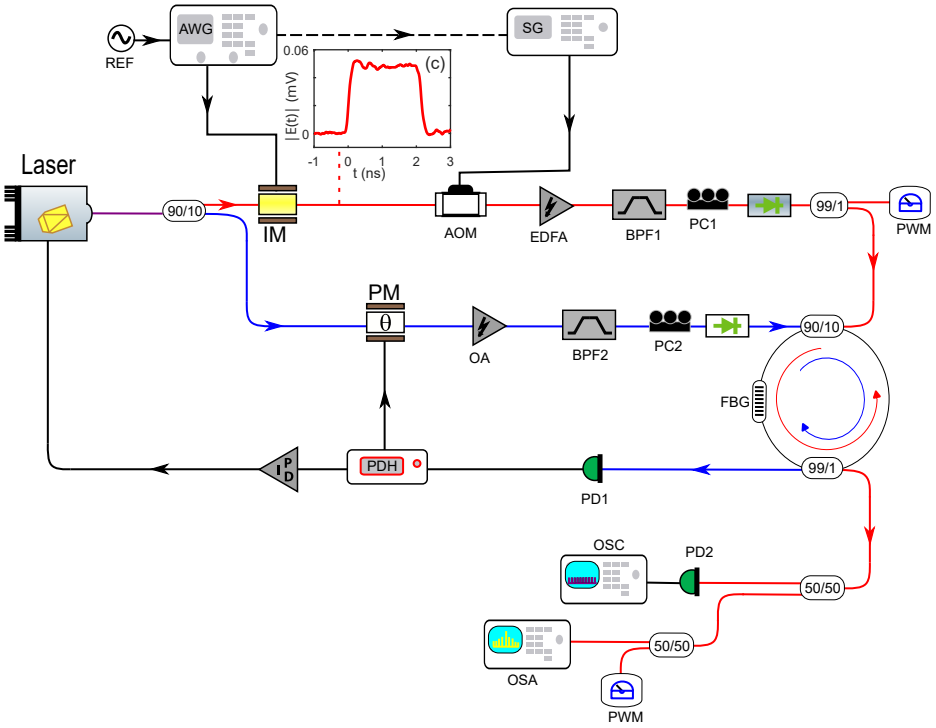

Figure 5.6 – Experimental setup used for the study of GTF dependency on $\Delta\beta_1$. For the detailed description see Fig. 3.1, in Chap. 3.

significantly. The study of such a phenomenon required a special analysis, which confirmed the experimental observation. Interestingly, a similar phenomenon can be observed for GTF instabilities. This test was carried out on the cavity described in Chap. 3 and with the same setup, where the $\Delta\beta_1$ can be tuned by carefully modulating the reference frequency of the AWG. For the sake of clarity, we propose the scheme of the experiment in Fig. 5.6 again, but for a detailed description we address the reader to the specific section 3.1. In the scheme of Fig. 5.6, the reference frequency and thus the $\Delta\beta_1$ can be tuned with the function generator labeled as REF.

Similarly to the previous section, we set the pump power $P_{in} = 17.5$ W and a detuning where the cavity is monostable $\phi_0 = 0.05$ rad. The wavelength of the pump was fixed at $\lambda_p = 1545.4$ nm to destabilise only GTF instabilities. We then stabilised the cavity and started to detune the synchronisation by acting on the REF. The result is shown in Fig. 5.7. In particular, Fig. 5.7(a) is the evolution of

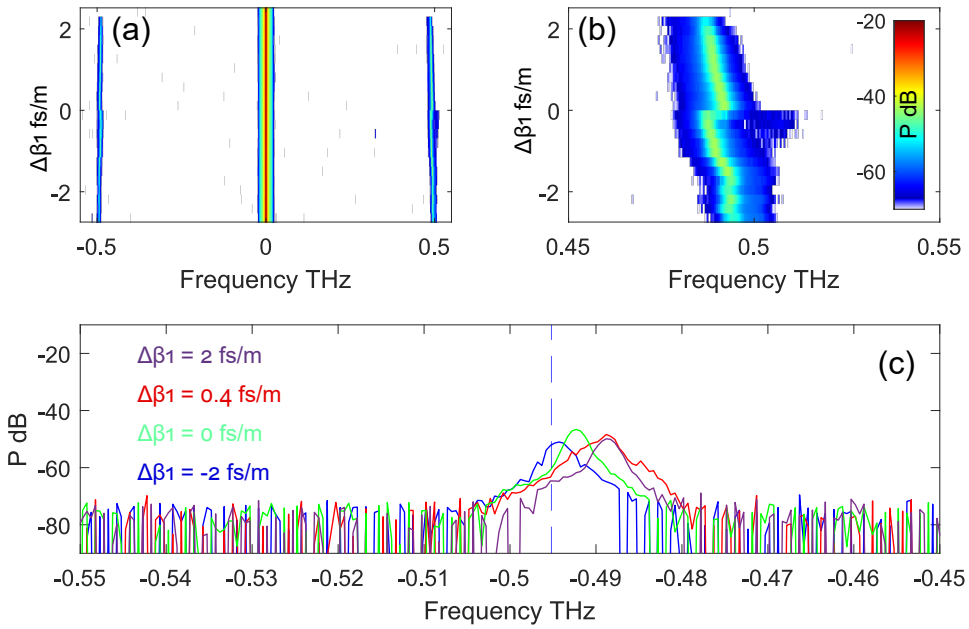

Figure 5.7 – (a) Evolution of the GTF spectra as a function of $\Delta\beta_1$. (b) zoom on the first negative band. (c) Four examples of the sidebands taken at different $\Delta\beta_1$, the dashed blue line is the central position of the filter.

the spectrum for $\Delta\beta_1 \in [-2.5, 2.5]$ fs/m. To get a clearer view of the evolution of the GTF band shift, we plot the first negative GTF band in Fig. 5.7(b). Fig. 5.7 (c) are the spectra at $[-2, 0, 1, 2]$ fs/m for the blue, green, red and violet traces respectively. It's interesting to note that, in this case too, the position of the band does indeed vary with the cavity's synchronisation mismatch. The variation is less intense than that observed for the MI bands, but it is still noticeable. In particular, at the interval ±1 fs/m, where the band first moves away from the pump and then back towards the centre, as shown in figure 5.7 (b).

Unfortunately, it wasn't possible to record data in the temporal domain because the repetition rate of the time-lens system (integer multiple of 99.88 MHz) was not synchronised with the repetition rate of the cavity. However, it may be interesting to explore this possibility in the future.

As a final result, we present the evolution of the threshold of GTF and parametric instabilities in the case of anomalous dispersion. In Chap. 3 we gave a detailed explanation of the evolution of the thresholds as a function of the linear phase ϕ_0. During the measurements in the anomalous dispersion regime,

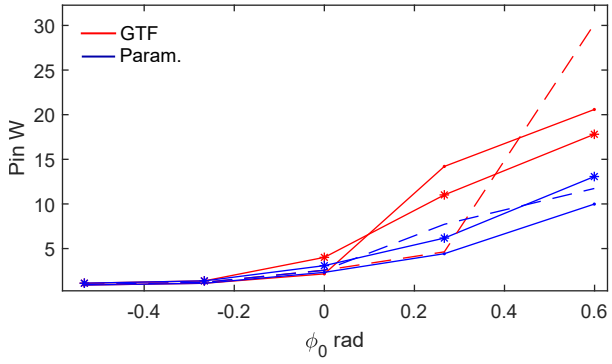

Figure 5.8 – Evolution of the threshold of GTF (red) and parametric (blue) instabilities, as function of the linear detuning ϕ_0, at different synchronization mismatches. The dashed curves are for $\Delta\beta_1 = +1.57$ fs/m, the solid lines with dots are $\Delta\beta_1 = +0.36$ fs/m and the solid lines with stars are for $\Delta\beta_1 = -1.69$ fs/m.

we decided to analyse the dependence of the threshold on the synchronisation mismatch, and the result is shown in Fig. 5.8. The blue curves are the evolution of the parametric instabilities and the red curves are the GTF instabilities. The dashed curves are for $\Delta\beta_1 = +1.57$ fs/m, the solid lines with dots are for $\Delta\beta_1 = +0.36$ fs/m and the solid lines with stars are for $\Delta\beta_1 = -1.69$ fs/m. In the low detuning range, where the two instabilities rise almost together, $\Delta\beta_1$ does not affect the thresholds too much, but as the phase detuning increases, the thresholds start to vary. The simulation of the effects of synchronization mismatch in the context of GTF is still a work in progress, and it will not shown in this thesis.

5.6 Summary

- In this chapter, we have theoretically and experimentally analysed the dependence of the frequency of the MI on the synchronisation mismatch between the pump pulses and the cavity.

- The theoretical analysis showed how the synchronisation mismatch leads to the competition between two different instability regimes: absolute and convective. This competition leads to the movement of the sidebands of the MI spectrum as well as to a temporal drift of the modulated signal.

- We build a setup with which we were able to records the evolution in both frequency and temporal domain. The temporal domain recording were possible thanks to the use of a time-lens system, which allows to magnify the temporal dynamics without distortions.
- Finally, we shown how the synchronization mismatch acts also on the position and on the thresholds of GTF instabilities. A theoretical work is still needed to fully describe the phenomenon.

Chapter 6

GTF in an active cavity

6.1 Introduction

One of the major limitations in fibre cavities are the losses induced by the elements of the resonators, such as couplers and filters. In the context of MI and GTF, when the losses are very high, the thresholds of the phenomena could be unreachable in experiments.

A clever solution to this problem has recently been proposed by Englebert *et. al.* [64, 65, 66], consisting of the compensation of the intracavity losses by means of a fibre amplifier embedded in the structure. This technique, allows to pass from finesse in the order of 20, to finesse in the order of 100. Thanks to the collaboration of Nicolas Englebert, we were able to implement such a solution in our setup for the study of GTF, dramatically lowering the power thresholds. We also collaborated with Auro M. Perego and Minji Shi from the Aston Institute of Photonic Technologies at Aston University (Birmingham, UK) on the theoretical development of GTF in an active cavity.

6.2 GTF in active cavity

We propose in the following the main points to derive the LLE model. The active medium used for this setup is a piece of Erbium-Doped Fiber, typically used in the construction of EDFA. We can extend the Ikeda Map model of Eq. 2.24 by

including the propagation in the EDF as follows:

$$i\frac{\partial E_n(z,\tau)}{\partial z} = \left(\frac{g}{2} - \frac{g}{2\Omega_g^2}\frac{\partial^2 E_n(z,\tau)}{\partial t^2}\right)\frac{\beta_2^{(1)}}{2}\frac{\partial^2 E_n(z,\tau)}{\partial \tau^2} + \\ -\gamma^{(1)}|E_n(z,\tau)|^2 E_n(z,\tau),\ 0 < z < L_1 \tag{6.1}$$

$$i\frac{\partial E_n(z,\tau)}{\partial z} = \frac{\beta_2^{(2)}}{2}\frac{\partial^2 E_n(z,\tau)}{\partial \tau^2} - \gamma^{(2)}|E_n(z,\tau)|^2 E_n(z,\tau),\ L_1 < z < L_2 \tag{6.2}$$

$$E_{n+1}(z=0,\tau) = \theta E_{in} + \rho e^{i\phi_0} h(t) \star E_n(z=L_2,\tau). \tag{6.3}$$

Where the gain $g(z) = \dfrac{g_0}{1 + (P_{sat}t_R)^{-1}\int_0^{t_R}|E_n(L_1,t)|^2 dt}$, g_0 is the unsaturated power, P_{sat} is the gain saturation power, t_R is the round-trip time of the cavity [64, 134] and Ω_g is the bandwidth of the gain. Eq. 6.1, describes the propagation of the intracavity field E_n in the EDF, so $\beta_2^{(1)}$ and $\gamma^{(1)}$ are the dispersion and Kerr parameters of the doped fibre, and L_1 is its the length. Equations 6.2 accounts for the propagation in the single mode fibre: $\beta_2^{(2)}$ is the dispersion, $\gamma^{(2)}$ the Kerr nonlinear parameter and L_2 is its length. Finally, Eq. 6.3 describes the boundary condition of the system: θ and ρ are the transmission and reflection parameter of the coupler, ϕ_0 is the phase detuning, $h(t)$ is the filter and E_{in} is the input field. τ is the variable representing time in the pulse reference frame and z represents the distance space. The description of the filter is the one used in chapter 2, so that $H(\omega) = e^{F(\omega)+i\psi(\omega)}$, and $h(t) = \mathcal{F}^{-1}H(\omega)$, where $F(\omega)$ and $\psi(\omega)$ defines the losses and the phase profile of the filter as in Eq. 2.22 and 2.23.

We can assume the steady state solution of the cavity in the form $E_n(z) = \sqrt{P_n(z)}e^{i\phi_n(z)}$, where $\phi_n(z)$ is the steady state phase. By using this, is possible to compute the well known relation between the intracavity and input power as:

$$P = \frac{\theta^2 P_{in}}{1 - \rho'^2 - 2\rho'\cos\Phi}, \tag{6.4}$$

where $\rho' = \rho e^{g_0 L_1/2 + F(0)}$ and $\Phi = \phi_0 + \psi(0)$. The new definition of ρ' becomes particularly useful by to directly compute the finesse of the cavity $\mathcal{F} = 2\pi\sqrt{\rho'}/(1-\rho')$, giving a direct way to estimate the losses of the cavity and the unsaturated gain

factor g_0.

6.2.1 LLE model: stability analysis and parametric gain

From the map of Eqs. (6.1) - (6.3), it is possible to derive the equivalent LLE model which reads:

$$\begin{aligned} L\frac{\partial E}{\partial z} =& [-\alpha + i\phi_0 + \Phi\star + i\Psi\star]E \\ &+ \frac{g}{2}L_1 + \frac{g}{2\Omega_g^2}\frac{\partial^2 E}{\partial \tau^2} - \frac{iL\beta_2}{2}\frac{\partial^2 E}{\partial \tau^2} + iL\gamma|E|^2E + \theta'\sqrt{P_{in}}. \end{aligned} \tag{6.5}$$

where $L = L_1 + L_2$ is the total length of the cavity, and $\beta_2 = (\beta_2^{(1)}L_1 + \beta_2^{(2)}L_2)/L$ and $\gamma = (\gamma^{(1)}L_1 + \gamma^{(2)}L_2)/L$ are the averaged dispersion and nonlinear parameter, respectively. Assuming the steady state solution as $E_0 = \sqrt{P}e^{\xi}$, the relation between the intracavity P and input power P_{in} can be obtained as:

$$P = \frac{\theta^2 P_{in}}{(\ln\rho + \frac{g_0 L_1}{2+2P/P_{sat}} + F(0))^2 + (\phi_0 + \psi(0) + \gamma PL)^2} \tag{6.6}$$

We can compute the parametric gain associated with the LLE by performing a stability analysis. We can consider a perturbation of the steady state solution such that $E = E_0 + ae^{-i\omega t} + be^{i\omega t}$, with $|a|, |b| \ll |E_0|$. By linearising Eq. 6.5 with respect to the small perturbation, we obtain the following system:

$$L\frac{\partial}{\partial z}\begin{pmatrix} a \\ b^* \end{pmatrix} = \left[\begin{pmatrix} d(\omega) & 0 \\ 0 & d(\omega) \end{pmatrix} + \begin{pmatrix} S(\omega) & C \\ C^* & -S(\omega) \end{pmatrix}\right]\begin{pmatrix} a \\ b^* \end{pmatrix} \tag{6.7}$$

where the elements of the matrix are:

$$\begin{aligned} d(\omega) &= \ln\rho + \frac{1}{2}(1 - \frac{\omega^2}{\omega_g^2})\frac{g_0 L_1}{1 + P/P_{sat} + F_e(\omega) + i\psi_o(\omega)}, \\ S(\omega) &= F_o(\omega) + i\Big[\phi_0 + \psi_e(\omega) + \omega^2\beta_2 L/2 + 2\gamma PL\Big], \\ C &= i\gamma PLe^{i2\xi}. \end{aligned} \tag{6.8}$$

$F_o(\omega)$ and $\psi_e(\omega)$ are the odd and even part of the function $F(\omega)$ and $\psi(\omega)$, which

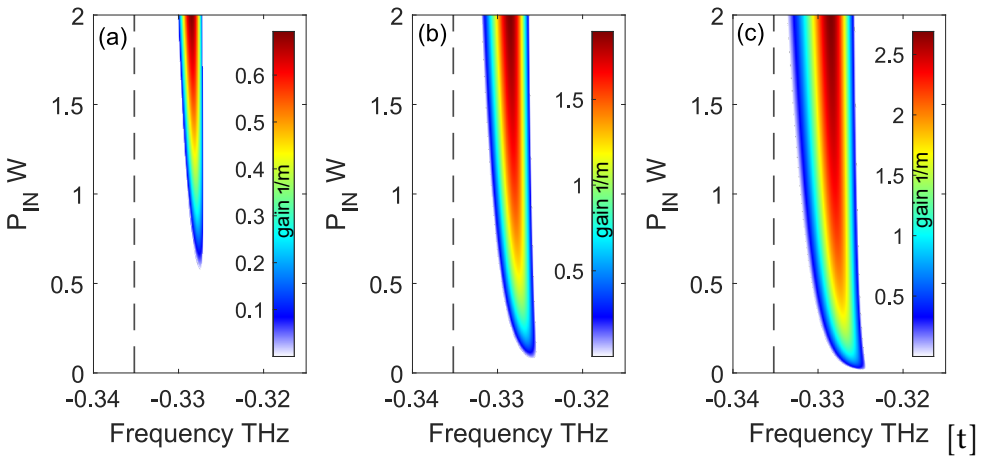

Figure 6.1 – 2D plots of the parametric gain as function of P_{in} computed with Eq. (6.9). (a) the finesse is 62, equivalent to $\rho' = 0.951$ and unsaturated gain $g_0 = 3.9481\, dB/m$; (b) the finesse is 82, equivalent to to $\rho' = 0.96$ and unsaturated gain $g_0 = 4.2617\, dB/m$; (c) the finesse is 105, equivalent to to $\rho' = 0.97$ and unsaturated gain $g_0 = 4.68\, dB/m$. The other parameters are: $\rho = \sqrt{0.67}$, $\theta = \sqrt{(0.05)}$, $a = 43$ rad/ns, $b = -1.06$, $\omega_f = 193.65$ THz, $P_{sat} = 0.5$ W, $\Omega_g = 25.13$ THz, $\beta_2^1 = -23\, ps^2$/km, $\gamma^{(1)} = 1.3e^{-3}$ /w/m, $L_1 = 0.33$m, $\beta_2^2 = 1.4\, ps^2$/km, $\gamma^{(s)} = 2.5e^{-3}$ /W/m, $L_2 = 85$m.

describes the loss and the phase of the filter in the frequency domain, respectively. The eigenvalues of the system Eq. (6.7) which describe the evolution of the perturbation are $\lambda_\pm = d(\omega) \pm \sqrt{S(\omega)^2 + |C|^2}$, from which is possible to compute the MI gain as:

$$g_{LLE}(\omega) = \frac{2}{L} Re(\lambda_+) \tag{6.9}$$

With Eq. (6.9) we are able to compute the parametric gain as function of the unsaturated gain g_0 which will be the control parameter in the experiment. In Fig. 6.1 are three example of parametric gain as function of P_{in}, computed with Eq. (6.9) for three different g_0. The black dashed line is the central position of the filter. Fig. 6.1 (a) shows the gain with finesse of 62, equivalent to $\rho' = 0.951$ ($g_0 = 3.9481\, dB/m$). In this case, the GTF P_{in} threshold is 0.6 W. Fig. 6.1 (b) is the parametric gain with a finesse of 82, equivalent to $\rho' = 0.96$ ($g_0 = 4.2617\, dB/m$), the GTF P_{in} threshold is 0.1 W. Finally, (c) is the parametric gain with a finesse of 105, equivalent to to $\rho' = 0.97$ ($g_0 = 4.68\, dB/m$) and the GTF P_{in} threshold

is 0.05 W. As expected, as the finesse increases, the power threshold decreases. A standard cavity for GTF (with two couplers and a filter) typically feature a finesse of 20. That finesse will give a GTF threshold of about $P_{in} = 32$ W. So, the active cavity analysed in this example lowers the threshold of about 53 times, in the worst case, which is a gigantic improvement.

6.2.2 Experimental Setup

The experimental setup, illustrated in Fig. 6.2, is fundamentally the same that used in chapter 3, so for an in depth description we address the reader to section 3.1. For the stabilization we kept the PDH system, and the driving of the cavity is made with a pulsed pump approach. The basic scheme of the cavity is shown in Fig. 6.2 (b). The main body is composed by 80 m of DSF, with a dispersion $\beta_2 = 3.8\, ps^2/km$. The driving (red) and stabilization (blue) signals are injected into the cavity trough the 90/10 coupler, and extracted trough the 99/1 tap coupler. The filter used is an FBG with central wavelength $\lambda_f = 1547.97$ nm, and it is fitted to the Lorenztian description used in Chap. 2 with the parameters $a = 43$ rad/ns and $b = -1.06$. The driving signal has a pulse width of 1 ns, and period $t_R = 435.1$ ns. The active part of the cavity is composed by a piece of $L_2 = 0.33$ m of Erbium Doped Fiber (EDF), spliced to the main body of the cavity through two wavelength division multiplexers (WDM). The pump of the EDF is is a laser diode (LD pump) at 1490 nm, injected through one of the WDM.

The active section must be carefully tuned to give maximum unsaturated gain. The unsaturated gain depends on the length of the active fibre [135]: if the fibre is too short, the gain will saturate at low pump powers (the active fibre pump, LD pump), whereas if the fibre is too long, the lasing threshold will be reached before saturation, limiting the maximum gain provided by the EDF. Experimentally, the lasing thresholds depend on the losses of the entire cavity, so the search for the ideal length is done by trials and errors. In particular, we start with a piece of EDF about 40 cm long and shorten it by one centimetre at a time until the cavity doesn't lase any more. The final length of the EDF obtained with this method is 33 cm. The active cavity generates an Amplified Spontaneous Emission (ASE) visible as a noise floor in the spectrum of the intracavity field

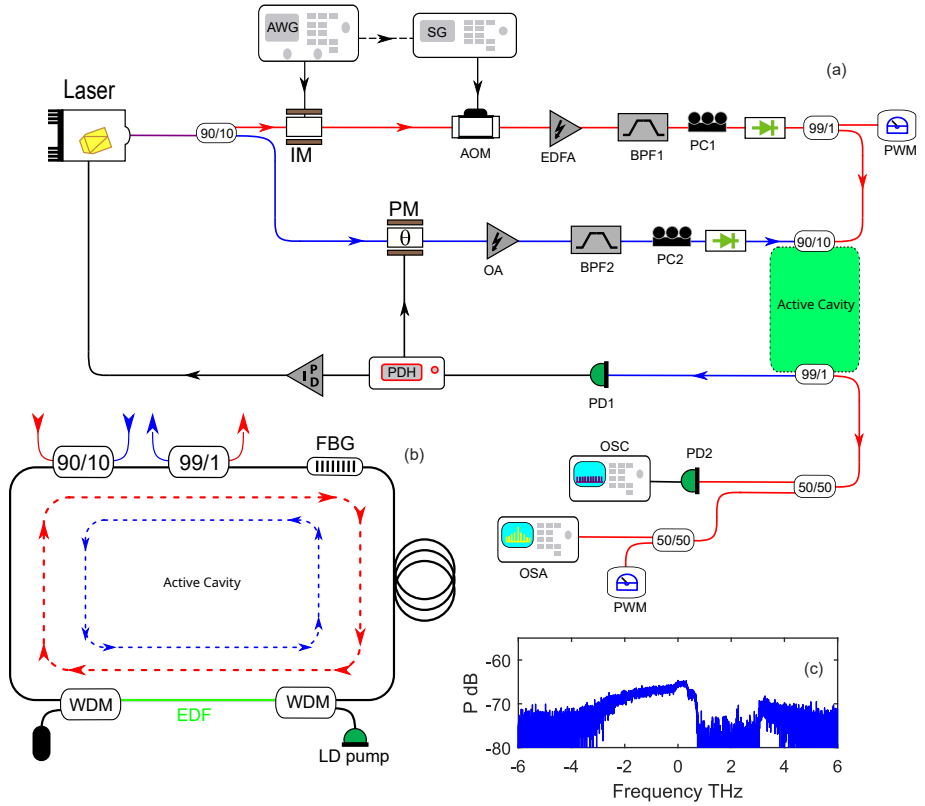

Figure 6.2 – (a) Experimental setup for the active cavity experimentation. For the complete description see section 3.1. (b) Structure of the active cavity: input/ouput coupler (90/10), TAP coupler (99/1), FBG. The EDF fiber is highlithed in green, and it's connected to the main body with two WDM. LF pump is the laser pump of the active section of the cavity, and have a wavelength of 1490 nm. (c) Typical ASE of the intracavity EDF.

(see Fig. 6.2 (c)). In the plot the ASE is visible between ±4 THz around the pump, with a hole in region 1 – 3 THz due to the WDM.

6.2.3 Experimental results

We measured the intracavity spectrum at increasing powers, for different level of EDF amplifications. The result is the consecutive decrease of the threshold of the GTF as the losses of the cavity are increasingly compensated by the EDF amplification. In Fig. 6.3 we plotted the intracavity spectrum as function of P_{in}, for an estimated finesse of 62. In this case the unsaturated gain of the EDF is

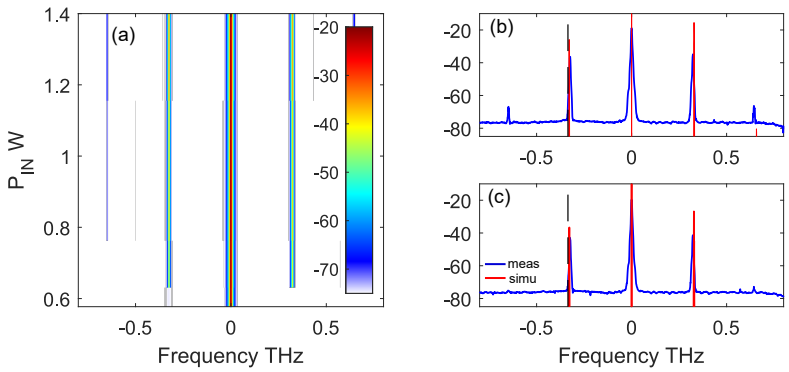

Figure 6.3 – (a) 2D plot of the spectra as a function of P_{in} for a finesse of about 62. (b) and (c) two example of measured spectra (blue) and simulated spectra, for $P_{in} = 0.96$ W and $P_{in} = 0.63$ W respectively. The black dashed line marks the central position of the filter.The parameter of the simulation are listed in the caption of Fig. 6.1.

$g_0 = 3.9481\ dB/m$, and the threshold of the GTF is $P_{in} = 0.6$ W . Fig. 6.3 (b) and (c) are two example for $P_{in} = 0.63$ W and $P_{in} = 0.97$ W respectively, where the blue traces are the experimental results and the red traces are the simulation obtained by integration of Eq.(6.5). We repeated the experiment with for higher gains, in particular in Fig. 6.4 $g_0 = 4.2617\ dB/m$, and Fig. Fig. 6.4 (b) and (c) are two examples for $P_{in} = 0.45$ W and $P_{in} = 0.9$ W. Finally, in Fig. 6.5 $g_0 = 4.68\ dB/m$, and the two spectra in Fig. 6.5 (b) and (c) refers to a $P_{in} = 0.35$ W and $P_{in} = 0.53$ W, respectively.

For all three examples, the simulations are in good agreement with the measurements. The only small disagreement is the exact value of the power threshold of the GTF. Indeed, even if the evolution of the threshold is coherent with the compensation of the losses (higher finesses bring to lower thresholds), the theoretical threshold computed for the highest finesses reached in this case is much lower. We plot the theoretical and experimental threshold as function of finesse in Fig. 6.6. The blue line are the theoretical results, computed with Eq. (6.5), and the red stars are the measured thresholds. As shown, there is a quantitative difference between the theoretical and the measured results. We attribute that to different factors, among which we mention the uncertainty on some of the parameters that compose the system (in particular the dispersion of

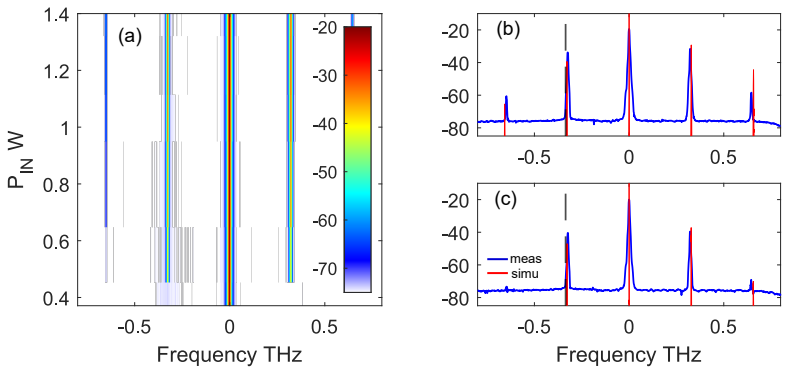

Figure 6.4 – (a) 2D plot of the spectra as a function of P_{in} for a finesse of about 82. (b) and (c) two example of measured spectra (blue) and simulated spectra, for $P_{in} = 0.9$ W and$P_{in} = 0.45$ W respectively. The black dashed line marks the central position of the filter.The parameter of the simulation are listed in the caption of Fig. 6.1.

the EDF). With that, the theoretical model doesn't take into account the counter-propagative scheme of the experiment. Usually this is not a problem, because the control signal is much weaker respect to the nonlinear signal, but in this case the amplification happen in both ways. A possible solution could be the use of an isolator inside the cavity, which force the circulation of the light in one direction only. Another idea could be to not using a dedicated signal for the stabilization signal, but using a portion of the driving signal to lock the stabilization system [65, 64], both alternatives could be tested in further investigations.

6.2.4 Conclusion and perspective

In conclusion, we successfully developed an active cavity for the study of GTF. The inclusion of the EDF inside the resonator, allowed for a drastic reduction of the GTF threshold, of about 53 time respect a passive cavity with equivalent dispersion and nonlinearity characteristic. The study is still a work in progress, and our first objective now is the characterization of the evolution of the threshold as a function of the gain of the EDF. Beside that, this setup allows for the exploration of domain which require high finesses, such as soliton formation and bistable dynamics [65, 64].

We also note here that a different version of the experiment involving the

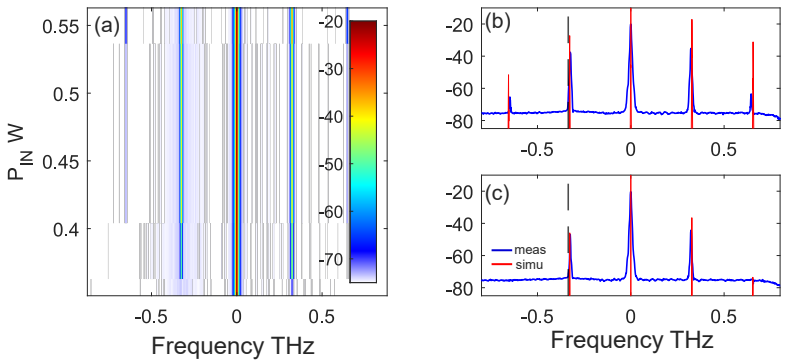

Figure 6.5 – (a) 2D plot of the spectra as a function of P_{in} for a finesse of about 105. (b) and (c) two example of measured spectra (blue) and simulated spectra, for P_{in} = 0.53 W and P_{in} = 0.35 W respectively. The black dashed line marks the central position of the filter.The parameter of the simulation are listed in the caption of Fig. 6.1.

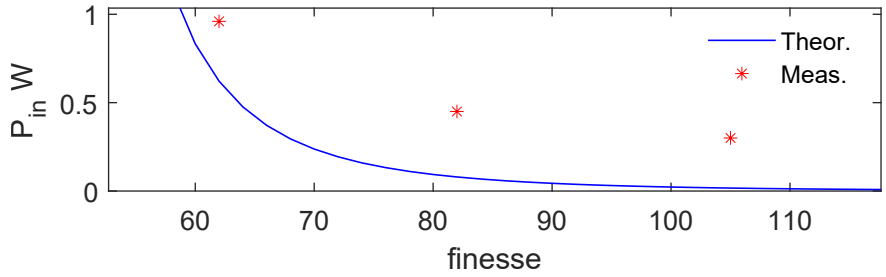

Figure 6.6 – Theoretical (blue) and experimental (red star) input power thresholds as a function of the finesse. The parameters of the theoretical calculation are listed in the caption of Fig. 6.1.

generation of MI at a wavelength of 2μm, using an active fiber cavity is reported in Appendix A.

6.3 Summary

- In this chapter we have presented a method for reducing the power losses in a fibre cavity for GTF. It consists of embedding an ED fiber amplifier in the fibre cavity to compensate for the losses. A fine adjustment of the gain allows the whole system to act as a passive cavity with an extremely high finesse.

- In collaboration with Minji Shi (AiPT), we developed a theoretical model to describe GTF in the context of an active cavity. We described the LLE model and proposed a semi-analytical description of the parametric gain. As expected, the higher the gain of the EDFA, the lower the losses and hence the lower the GTF threshold.

- In collaboration with Nicolas Englebert (ULB), we have constructed an active cavity setup that allows the measurement of GTF spectra. We describe the procedure for tuning the gain section to keep the cavity below the lasing threshold and the experimental result. The overall agreement with the theoretical and numerical model is quite good.

Conclusion

In this thesis, we primarily investigated a phenomenon known as Gain Through Filtering in optical fiber cavities. In particular, we experimentally and theoretically studied GTF in different scenarios, that can be summarized as follows:

- We have characterised GTF in fibre cavities with normal and anomalous dispersion. In particular, we have shown how GTF can coexist with parametric MI and how the two phenomena behave as a function of cavity detuning and input power. This theoretical and experimental study proved that in the normal dispersion regime, the input power thresholds of GTF and parametric MI can be inverted by carefully tuning the phase detuning. The same phenomenon cannot be achieved in the anomalous dispersion regime. In the realization of the experimental setup, we upgraded the stabilization system by adapting the PDH to our cavity setup, which proved to be very effective.

- We have theoretically studied GTF in a polarisation-maintaining (PM) cavity. In particular, we generalised the Ikeda map and the LLE model to describe propagation in a fully PM resonator (including filter) and derived the corresponding parametric gain functions. We characterised the parametric gains as a function of several cavity and filter parameters: the injection angle χ, the distance between the central frequencies of the polarisation components of the filter, and $\Delta_{\beta 1}$. To validate the theoretical model, we compared the results with the numerical integration of the Ikeda map and the LLE. The result of this study demonstrated how it is possible to generate dual frequency combs in a fully PM cavity using GTF.

- Inspired by the work of Englebert *et al.* [64], we built an active fiber cavity for the study of GTF. In particular, a regular cavity for GTF studies has been modified by adding a portion of EDF. The gain produced by the EDF compensate for the losses of the cavity, allowing relatively high finesses. With this setup, we were able to lowering the power threshold of GTF of about 53 times. For the theoretical study of the phenomenon we developed, in collaboration with Minji Shi and Auro Perego of AiPT, a generalized GTF in active cavity theory, which includes the effects of the gain of the EDF. The agreement between the theory and the numerical simulation is good.

In the general context of intracavity modulation instability, we conducted some fundamental studies of the phenomenon. In particular:

- We have investigated the effect of pump-cavity synchronisation mismatch on the location of MI.This study shows how the position of the sidebands of MI is influenced by the synchronisation mismatch that can occur between the input and intracavity pulse trains. This dependence is due to the competition between two regimes of MI: absolute and convective. The convective state occurs when the synchronisation mismatch is relatively large, so the drive pulse is only partially modulated, but the position of the band doesn't change. In the absolute regime, the whole pulse is modulated, but if the driving pulse is even slightly desynchronised with respect to the natural repetition rate of the cavity, a competition with the convective regime takes place. This leads to two effects: in the time domain, the modulated signal is drifted due to the imperfect superposition of the intracavity and input pulses, while in the frequency domain, the position of the peaks of the MI is shifted, which was quite unexpected. We were able to measure this phenomenon in both the spectral and time domain, confirming the observation by numerical simulations and theoretical results. This study helped to understand the importance of the synchronisation mismatch in the context of pulsed pumped devices.

There are also some potential lines of developments which are still open. In particular:

- Experimental proof of PM GTF is still lacking. The theoretical model that we developed gave some optimistic results, suggesting that a dual frequency comb obtained by a fibre cavity is theoretically possible. The experiment could present some technical difficulties, in particular because of the large number of parameters that need to be controlled. Nevertheless, we believe that a simplified version of the phenomenon could be demonstrated by first using a PM FBG in a standard isotropic fibre cavity. The two polarisations could then be separated at the output of the cavity using a polarisation beam splitter. A second issue to be addressed is the intrinsic coupling of the fields in the two polarisations. As expected, one possible solution would be to introduce two orthogonal linearly polarised beams, parallel to the two polarisation axes of the cavity. In theory, this keeps the two polarisations independent and minimises the XPM term that distorts the pulses. Once a clean dual-comb is generated, the two components could be separated and the two modulated signals can be used as seeds to generate the actual train of solitons by MI. We therefore believe that this theoretical study really paves the way for many interesting experimental demonstrations.

- As part of the Mefista project, we hosted Moritz Bartnick from EPFL. With him, we adapted the active cavity setup built for the GTF experiment into a 2 μm fibre cavity. With our study we've shown that it's possible to get MI instability in this region even with a standard SMF cavity. Although this is a simple demonstration, we have shown with this study that most of the results obtained in the C/L band are basically reproducible in the $2\mu m$ band by effectively compensating for the large losses of this region. We believe that with an improved setup, especially in terms of system stabilisation, it should be possible to study even more complex nonlinear dynamics, such as the formation of solitons and optical frequency combs. In addition to the fundamental interest of such a study, this wavelength range is very attractive in the context of spectroscopy due to the high efficiency absorption of many organic elements.

Appendix A

MI at 2 micron fiber resonator

As part of the ITN Mefista project, we collaborated with PhD student Moritz Bartnick from the Ècole Politechnique Fèdèrale de Lausanne. The main aim of this collaboration was to observe MI in a fibre cavity operating in the $2\mu m$ region. Recently, interest in the mid-infrared has grown rapidly, especially for spectroscopic applications. The development of techniques such as dual-frequency comb spectroscopy [123, 136, 125], and the strong molecular absorption in the mid-infrared spectral range [137], is confronted with the lack of a directly generate optical frequency combs at 2μm. Until now, most approaches to obtain frequency combs in this region consist in down-converting frequency combs in the L/C band, which can be easily obtained by cascading intensity and phase modulators (EOMs) [138, 139].

We have already discussed how MI could be a valid method for generating Kerr frequency combs in optical cavities [54], and in this work we want to demonstrate that it is possible to obtain MI in a 2 μm fibre cavity. The main challenge from this point of view is the losses: indeed, standard SMF are optimised to work in the telecom band, around 1.5 μm, and the losses increase steeply in this kind of support (> 10 dB/km). Inspired by the work of the previous section 6.2.2, we decided to adapt the active cavity setup to this case.

A.0.1 Experimental Setup

Fig. A.1 (a) is the schematic of the experimental setup used for this experiment. The source is a 2 μm thermally tunable laser provided by another member of the ETN Mefista project, PhD student Anamika Nair Karunakara, in collaboration with NKT Photonics. The source is modulated into pulses with a width of $\tau = 1$ ns and a repetition rate of $T_0 = 830\, ns$ and amplified using a commercial thulium-doped fibre amplifier (TDFA). The pulse train is split into two: 90% is

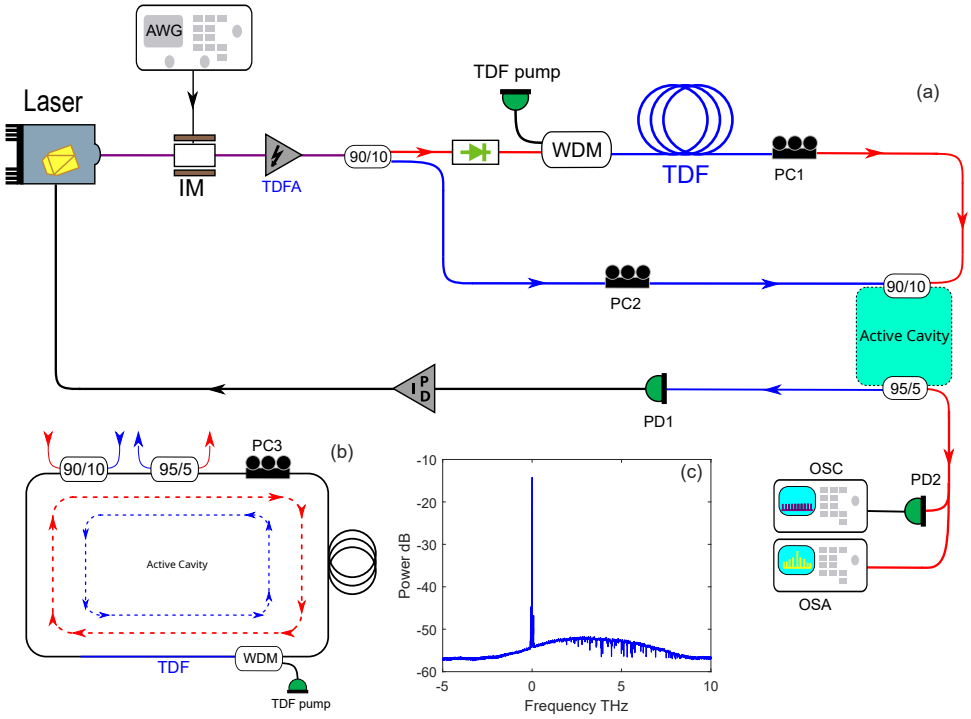

Figure A.1 – (a) Scheme of the experimental setup. IM: intensity modulator; TDFA: Thulium doped fiber amplifier; WDM: wavelength division multiplexer; TDF pump: laser diode pump for Thulium fiber (1550 nm); TDF: Thulium doped fiber; PC(1,2,3) polarization controllers; PD: photo diodes; PID: proportional-integrative-derivative controller module; OSC/OSA : oscilloscope and spectrum analizer. (b) Scheme of the active cavity; (c) typical example of the intracavity field where is possible to note the driving pump (at 0 THz) and the amplified spontaneous emission of the TDF.

used as the non-linear beam (red), while 10% is used as the control beam. The non-linear beam is amplified again, this time with a TDFA , consisting of a piece of TDF and a pump at around 1550 nm. Once amplified, the signal is passed through a polarisation controller (PC1) and injected into the cavity. The control beam (blue) is injected directly into the cavity in the opposite direction. A tap coupler is used to collect the two beams: the non-linear beam is collected and processed by an optical spectrum analyser (OSA) and an oscilloscope (OSC), while the control beam passes through a photodiode (PD2). The signal from the photodiode is processed by a PID module, which provides the correction signal to the pump. In the scheme, the two polarisation controllers PD1 and PD2 are used to align the polarisation state of the nonlinear and control beams to the polarisation axes of the cavity, while PD3 (inside the cavity) is used to control

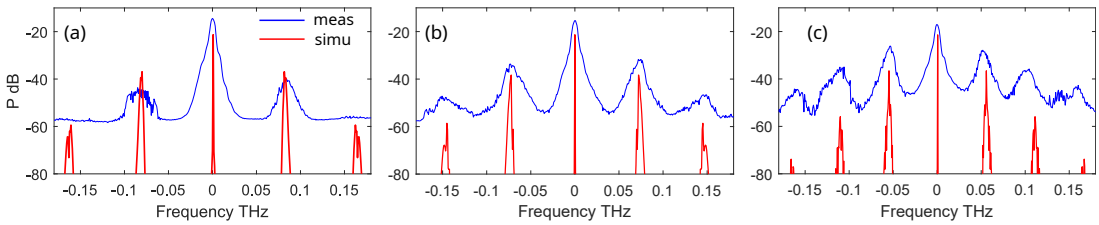

Figure A.2 – Three examples of MI spectra in the 2 micron active cavity. Blue traces are the measures, red traces are the simulations. (a) $P_{in} = 0.85$ W and $\phi_0 = 0$ rad, (b) $P_{in} = 1.8$ W and $\phi_0 = 0.05$ rad, finally in (c) $P_{in} = 0.9$ W and $\phi_0 = 0.18$ rad. The parameters used for the simulation are: L=35.6 m, $\beta_2 = -80\, ps^2/km$, $\gamma = 1.5$ 1/W, $\rho = \sqrt{0.7}$, $\theta = \sqrt{0.1}$.

the linear phase detuning. A typical intracavity spectrum is shown in Fig. A.1(c): at 0 THz the driving pump peak is visible, and between -3 THz and 8.5 THz the amplified spontaneous emission of the TDF can be seen.

A.0.2 Experimental results

The main objective of this experiment was to demonstrate that it is possible to generate MI in a $2\mu m$ cavity. Due to the limitations of the setup, the result was quite challenging. In the experiment to record the MI spectra, we fixed a phase detuning and changed the power of the input TDFA. In Fig. A.2 we propose three different examples of MI at 2 μm: in Fig. A.2 (a) $P_{in} = 0.85$ W and $\phi_0 = 0$ rad, in Fig. A.2 (b) $P_{in} = 1.8$ W and $\phi_0 = 0.05$ rad and in Fig. A.2 (c) $P_{in} = 0.9$ W and $\phi_0 = 0.18$ rad. The blue line is the measurement, while the red lines are the simulations made by integrating the LLE of Eq. (2.12) with the parameters listed in the caption of Fig. A.2. The P_{in} and the ϕ_0 have been fitted to the simulations, while the other parameters are listed in the caption of the figures. We can see that by fitting ϕ_0 the position of the MI bands is confirmed by the numerical simulations. In particular, while the position of the bands is mainly determined by the dispersion $\beta_2 = -80\, ps^2/km$, small changes in the detuning lead to important changes in the FRS of the spectrum.

A.0.3 Conclusions and perspective

In conclusion, with this experiment we have shown that the generation of MI at $2\mu m$ is possible, but we have also highlighted some critical problems: the amount of losses, at least with standard SMF 28 fibre, makes the use of an active setup mandatory. A robust stabilisation technique must be used to keep the phase, and therefore the MI bands, stable. We also think that with a more optimised

scheme, typical nonlinear phenomena such as cavity solitons could be generated.

Bibliography

[1] C. V. Raman and K. S. Krishnan. "A New Type of Secondary Radiation". en. In: *Nature* 121.3048 (Mar. 1928). Number: 3048 Publisher: Nature Publishing Group, pp. 501–502. ISSN: 1476-4687. DOI: 10.1038/121501c0. URL: https://www.nature.com/articles/121501c0 (visited on 08/21/2020).

[2] U. Eckern. "Editorial: Ann. Phys. 7–8/2008". en. In: *Annalen der Physik* 521.7-8 (Aug. 2009), pp. 465–465. ISSN: 0003-3804, 1521-3889. DOI: 10.1002/andp.200952107-803. URL: https://onlinelibrary.wiley.com/doi/10.1002/andp.200952107-803 (visited on 09/22/2023).

[3] T. H. Maiman. "Optical and Microwave-Optical Experiments in Ruby". en. In: *Phys. Rev. Lett.* 4.11 (June 1960), pp. 564–566. ISSN: 0031-9007. DOI: 10.1103/PhysRevLett.4.564. URL: https://link.aps.org/doi/10.1103/PhysRevLett.4.564 (visited on 09/22/2023).

[4] T. H. Maiman. "Stimulated Optical Radiation in Ruby". en. In: *Nature* 187.4736 (Aug. 1960). Number: 4736 Publisher: Nature Publishing Group, pp. 493–494. ISSN: 1476-4687. DOI: 10.1038/187493a0. URL: https://www.nature.com/articles/187493a0 (visited on 09/22/2023).

[5] P. A. Franken et al. "Generation of Optical Harmonics". en. In: *Phys. Rev. Lett.* 7.4 (Aug. 1961), pp. 118–119. ISSN: 0031-9007. DOI: 10.1103/PhysRevLett.7.118. URL: https://link.aps.org/doi/10.1103/PhysRevLett.7.118 (visited on 09/22/2023).

[6] W. Kaiser and C. G. B. Garrett. "Two-Photon Excitation in Ca F 2 : Eu 2 +". en. In: *Phys. Rev. Lett.* 7.6 (Sept. 1961), pp. 229–231. ISSN: 0031-9007. DOI: 10.1103/PhysRevLett.7.229. URL: https://link.aps.org/doi/10.1103/PhysRevLett.7.229 (visited on 09/22/2023).

[7] EJ Woodbury and WK Ng. "Ruby laser operation in the near IR". In: *proc. IRE* 50.11 (1962), pp. 2347–2348.

[8] R. W. Hellwarth. "Theory of Stimulated Raman Scattering". In: *Phys. Rev.* 130.5 (June 1963). Publisher: American Physical Society, pp. 1850–1852. DOI: 10.1103/PhysRev.130.1850. URL: https://link.aps.org/doi/10.1103/PhysRev.130.1850 (visited on 09/22/2023).

[9] R. Y. Chiao, C. H. Townes, and B. P. Stoicheff. "Stimulated Brillouin Scattering and Coherent Generation of Intense Hypersonic Waves". In: *Phys. Rev. Lett.* 12.21 (May 1964). Publisher: American Physical Society, pp. 592–595. DOI: 10.1103/PhysRevLett.12.592. URL: https://link.aps.org/doi/10.1103/PhysRevLett.12.592 (visited on 09/22/2023).

[10] R. L. Carman, R. Y. Chiao, and P. L. Kelley. "Observation of Degenerate Stimulated Four-Photon Interaction and Four-Wave Parametric Amplification". In: *Phys. Rev. Lett.* 17.26 (Dec. 1966). Publisher: American Physical Society, pp. 1281–1283. DOI: 10.1103/PhysRevLett.17.1281. URL: https://link.aps.org/doi/10.1103/PhysRevLett.17.1281 (visited on 09/22/2023).

[11] P. D. Maker, R. W. Terhune, and C. M. Savage. "Intensity-Dependent Changes in the Refractive Index of Liquids". In: *Phys. Rev. Lett.* 12 (18 May 1964), pp. 507–509. DOI: 10.1103/PhysRevLett.12.507. URL: https://link.aps.org/doi/10.1103/PhysRevLett.12.507.

[12] F. P. Kapron, D. B. Keck, and R. D. Maurer. "RADIATION LOSSES IN GLASS OPTICAL WAVEGUIDES". In: *Applied Physics Letters* 17.10 (Oct. 1970), pp. 423–425. ISSN: 0003-6951. DOI: 10.1063/1.1653255. URL: https://doi.org/10.1063/1.1653255 (visited on 09/22/2023).

[13] E P Ippen and R H Stolen. "Stimulated Brillouin scattering in optical fibers". en. In: (Aug. 1972), p. 4.

[14] R. H. Stolen and E. P. Ippen. "Raman gain in glass optical waveguides". en. In: *Appl. Phys. Lett.* 22.6 (Mar. 1973), pp. 276–278. ISSN: 0003-6951, 1077-3118. DOI: 10.1063/1.1654637. URL: http://aip.scitation.org/doi/10.1063/1.1654637 (visited on 12/07/2020).

[15] R H Stolen and Chinlon Lin. "Self-phase-modulation in silica optical fibers". en. In: (1978), p. 7.

[16] R. Stolen and A. Ashkin. "Optical Kerr effect in glass waveguide". en. In: *IEEE J. Quantum Electron.* 8.6 (June 1972), pp. 548–549. ISSN: 0018-9197, 1558-1713. DOI: 10.1109/JQE.1972.1077248. URL: http://ieeexplore.ieee.org/document/1077248/ (visited on 12/07/2020).

[17] R. Stolen. "Phase-matched-stimulated four-photon mixing in silica-fiber waveguides". en. In: (Mar. 1975), p. 4.

[18] Akira Hasegawa and Frederick Tappert. "Transmission of stationary nonlinear optical pulses in dispersive dielectric fibers. I. Anomalous dispersion". In: *Appl. Phys. Lett.* 23.3 (Aug. 1973). Publisher: American Institute of Physics, pp. 142–144. ISSN: 0003-6951. DOI: 10.1063/1.1654836. URL: https://aip-scitation-org.ressources-electroniques.univ-lille.fr/doi/abs/10.1063/1.1654836 (visited on 09/21/2020).

[19] Akira Hasegawa and Frederick Tappert. "Transmission of stationary nonlinear optical pulses in dispersive dielectric fibers. II. Normal dispersion". en. In: *Appl. Phys. Lett.* 23.4 (Aug. 1973), pp. 171–172. ISSN: 0003-6951, 1077-3118. DOI: 10.1063/1.1654847. URL: http://aip.scitation.org/doi/10.1063/1.1654847 (visited on 10/26/2021).

[20] A. Hasegawa and W. Brinkman. "Tunable coherent IR and FIR sources utilizing modulational instability". en. In: *IEEE J. Quantum Electron.* 16.7 (July 1980), pp. 694–697. ISSN: 0018-9197. DOI: 10.1109/JQE.1980.1070554. URL: http://ieeexplore.ieee.org/document/1070554/ (visited on 12/07/2020).

[21] T. Brooke Benjamin and J. E. Feir. "The disintegration of wave trains on deep water Part 1. Theory". en. In: *J. Fluid Mech.* 27.3 (Feb. 1967), pp. 417–430. ISSN: 0022-1120, 1469-7645. DOI: 10.1017/S002211206700045X. URL: https://www.cambridge.org/core/product/identifier/S002211206700045X/type/journal_article (visited on 09/21/2020).

[22] T. Taniuti and H. Washimi. "Self-Trapping and Instability of Hydromagnetic Waves Along the Magnetic Field in a Cold Plasma". en. In: *Phys. Rev. Lett.* 21.4 (July 1968), pp. 209–212. ISSN: 0031-9007. DOI: 10.1103/PhysRevLett.21.209. URL: https://link.aps.org/doi/10.1103/PhysRevLett.21.209 (visited on 12/07/2020).

[23] Akira Hasegawa. "Generation of a train of soliton pulses by induced modulational instability in optical fibers". en. In: *Opt. Lett.* 9.7 (July 1984), p. 288. ISSN: 0146-9592, 1539-4794. DOI: 10.1364/OL.9.000288. URL: https://www.osapublishing.org/abstract.cfm?URI=ol-9-7-288 (visited on 03/17/2020).

[24] Kuochou Tai et al. "Generation of subpicosecond solitonlike optical pulses at 0.3 THz repetition rate by induced modulational instability". In: *Applied Physics Letters* 49 (1986), pp. 236–238. URL: https://api.semanticscholar.org/CorpusID:121442333.

[25] K. Tai, A. Hasegawa, and A. Tomita. "Observation of modulational instability in optical fibers". In: *Phys. Rev. Lett.* 56.2 (Jan. 1986). Publisher: American Physical Society, pp. 135–138. DOI: 10.1103/PhysRevLett.56.

135. URL: https://link.aps.org/doi/10.1103/PhysRevLett.56.135 (visited on 03/13/2020).

[26] John M. Dudley, Goëry Genty, and Stéphane Coen. "Supercontinuum generation in photonic crystal fiber". en. In: *Rev. Mod. Phys.* 78.4 (Oct. 2006), pp. 1135–1184. ISSN: 0034-6861, 1539-0756. DOI: 10.1103/RevModPhys.78.1135. URL: https://link.aps.org/doi/10.1103/RevModPhys.78.1135 (visited on 12/09/2020).

[27] M. Taki et al. "Third-order dispersion for generating optical rogue solitons". en. In: *Physics Letters A* 374.4 (Jan. 2010), pp. 691–695. ISSN: 03759601. DOI: 10.1016/j.physleta.2009.11.058. URL: https://linkinghub.elsevier.com/retrieve/pii/S0375960109014911 (visited on 06/25/2021).

[28] Nail Akhmediev et al. "Roadmap on optical rogue waves and extreme events". In: *Journal of Optics* 18 (2016). URL: https://api.semanticscholar.org/CorpusID:37652186.

[29] Yunfei Yue, Lili Huang, and Yong Chen. "Modulation instability, rogue waves and spectral analysis for the sixth-order nonlinear Schrödinger equation". en. In: *Communications in Nonlinear Science and Numerical Simulation* 89 (Oct. 2020), p. 105284. ISSN: 10075704. DOI: 10.1016/j.cnsns.2020.105284. URL: https://linkinghub.elsevier.com/retrieve/pii/S1007570420301167 (visited on 09/23/2023).

[30] F. Matera et al. "Sideband instability induced by periodic power variation in long-distance fiber links". In: *Opt. Lett.* 18.18 (Sept. 1993), pp. 1499–1501. DOI: 10.1364/OL.18.001499. URL: https://opg.optica.org/ol/abstract.cfm?URI=ol-18-18-1499.

[31] F. Kh. Abdullaev et al. "Modulational instability of electromagnetic waves in media with varying nonlinearity". In: *J. Opt. Soc. Am. B* 14.1 (Jan. 1997), pp. 27–33. DOI: 10.1364/JOSAB.14.000027. URL: https://opg.optica.org/josab/abstract.cfm?URI=josab-14-1-27.

[32] P.D. Drummond et al. "Cross-phase modulational instability in high-birefringence fibers". en. In: *Optics Communications* 78.2 (Aug. 1990), pp. 137–142. ISSN: 00304018. DOI: 10.1016/0030-4018(90)90110-F. URL: https://linkinghub.elsevier.com/retrieve/pii/003040189090110F (visited on 11/23/2022).

[33] S. G. Murdoch et al. "Quasi-phase-matched modulation instability in birefringent fibers". In: *Opt. Lett.* 22.10 (May 1997), pp. 682–684. DOI: 10.1364/OL.22.000682. URL: https://opg.optica.org/ol/abstract.cfm?URI=ol-22-10-682.

[34] F.Kh. Abdullaev et al. “Modulational instability in optical fibers with variable dispersion”. en. In: *Physics Letters A* 220.4-5 (Sept. 1996), pp. 213–218. ISSN: 03759601. DOI: 10.1016/0375-9601(96)00504-X. URL: https://linkinghub.elsevier.com/retrieve/pii/037596019600504X (visited on 09/23/2023).

[35] Jared C. Bronski and J. Nathan Kutz. “Modulational stability of plane waves in nonreturn-to-zero communications systems with dispersion management”. en. In: *Optics Letters* 21.13 (July 1996), p. 937. ISSN: 0146-9592, 1539-4794. DOI: 10.1364/OL.21.000937. URL: https://opg.optica.org/abstract.cfm?URI=ol-21-13-937 (visited on 09/23/2023).

[36] Stéphane Pitois and Guy Millot. “Experimental observation of a new modulational instability spectral window induced by fourth-order dispersion in a normally dispersive single-mode optical fiber”. en. In: *Optics Communications* 226.1-6 (Oct. 2003), pp. 415–422. ISSN: 00304018. DOI: 10.1016/j.optcom.2003.09.001. URL: https://linkinghub.elsevier.com/retrieve/pii/S0030401803019217 (visited on 10/12/2023).

[37] Andrea Armaroli and Fabio Biancalana. “Tunable modulational instability sidebands via parametric resonance in periodically tapered optical fibers”. In: *Opt. Express* 20.22 (Oct. 2012), pp. 25096–25110. DOI: 10.1364/OE.20.025096. URL: https://opg.optica.org/oe/abstract.cfm?URI=oe-20-22-25096.

[38] M. Droques et al. “Experimental demonstration of modulation instability in an optical fiber with a periodic dispersion landscape”. en. In: *Optics Letters* 37.23 (Dec. 2012), p. 4832. ISSN: 0146-9592, 1539-4794. DOI: 10.1364/OL.37.004832. URL: https://opg.optica.org/abstract.cfm?URI=ol-37-23-4832 (visited on 09/23/2023).

[39] Maxime Droques et al. “Fourth-order dispersion mediated modulation instability in dispersion oscillating fibers”. en. In: *Optics Letters* 38.17 (Sept. 2013), p. 3464. ISSN: 0146-9592, 1539-4794. DOI: 10.1364/OL.38.003464. URL: https://opg.optica.org/abstract.cfm?URI=ol-38-17-3464 (visited on 09/23/2023).

[40] François Copie et al. “Modulation instability in amplitude modulated dispersion oscillating fibers”. en. In: *Optics Express* 23.4 (Feb. 2015), p. 3869. ISSN: 1094-4087. DOI: 10.1364/OE.23.003869. URL: https://opg.optica.org/abstract.cfm?URI=oe-23-4-3869 (visited on 09/23/2023).

[41] H. Nakatsuka et al. “Observation of Bifurcation to Chaos in an All-Optical Bistable System”. en. In: *Phys. Rev. Lett.* 50.2 (Jan. 1983), pp. 109–112. ISSN: 0031-9007. DOI: 10.1103/PhysRevLett.50.109. URL: https://link.aps.org/doi/10.1103/PhysRevLett.50.109 (visited on 05/11/2022).

[42] R. M. Shelby, M. D. Levenson, and S. H. Perlmutter. “Bistability and other effects in a nonlinear fiber-optic ring resonator”. en. In: *J. Opt. Soc. Am. B* 5.2 (Feb. 1988), p. 347. ISSN: 0740-3224, 1520-8540. DOI: 10.1364/JOSAB.5.000347. URL: https://opg.optica.org/abstract.cfm?URI=josab-5-2-347 (visited on 05/11/2022).

[43] Stéphane Coen et al. “Bistable switching induced by modulational instability in a normally dispersive all-fibre ring cavity”. en. In: *J. Opt. B: Quantum Semiclass. Opt.* 1.1 (Feb. 1999), pp. 36–42. ISSN: 1464-4266, 1741-3575. DOI: 10.1088/1464-4266/1/1/009. URL: https://iopscience.iop.org/article/10.1088/1464-4266/1/1/009 (visited on 05/07/2020).

[44] Masataka Nakazawa, Kazunori Suzuki, and Hermann A. Haus. “Modulational instability oscillation in nonlinear dispersive ring cavity”. en. In: *Phys. Rev. A* 38.10 (Nov. 1988), pp. 5193–5196. ISSN: 0556-2791. DOI: 10.1103/PhysRevA.38.5193. URL: https://link.aps.org/doi/10.1103/PhysRevA.38.5193 (visited on 03/26/2020).

[45] M. Haelterman, S. Trillo, and S. Wabnitz. “Low dimensional modulational chaos in diffractive nonlinear cavities”. en. In: *Optics Communications* 93.5-6 (Oct. 1992), pp. 343–349. ISSN: 00304018. DOI: 10.1016/0030-4018(92)90198-Z. URL: https://linkinghub.elsevier.com/retrieve/pii/003040189290198Z (visited on 11/10/2020).

[46] M. Haelterman, S. Trillo, and S. Wabnitz. “Dissipative modulation instability in a nonlinear dispersive ring cavity”. en. In: *Optics Communications* 91.5 (Aug. 1992), pp. 401–407. ISSN: 0030-4018. DOI: 10.1016/0030-4018(92)90367-Z. URL: http://www.sciencedirect.com/science/article/pii/003040189290367Z (visited on 03/24/2020).

[47] S. Coen and M. Haelterman. “Modulational Instability Induced by Cavity Boundary Conditions in a Normally Dispersive Optical Fiber”. In: *Phys. Rev. Lett.* 79.21 (Nov. 1997). Publisher: American Physical Society, pp. 4139–4142. DOI: 10.1103/PhysRevLett.79.4139. URL: https://link.aps.org/doi/10.1103/PhysRevLett.79.4139 (visited on 05/20/2020).

[48] Stéphane Coen and Marc Haelterman. "Competition between modulational instability and switching in optical bistability". en. In: *Opt. Lett.* 24.2 (Jan. 1999), p. 80. ISSN: 0146-9592, 1539-4794. DOI: 10.1364/OL.24.000080. URL: https://www.osapublishing.org/abstract.cfm?URI=ol-24-2-80 (visited on 12/14/2020).

[49] Stéphane Coen and Marc Haelterman. "Continuous-wave ultrahigh-repetition-rate pulse-train generation through modulational instability in a passive fiber cavity". en. In: *Opt. Lett.* 26.1 (Jan. 2001), p. 39. ISSN: 0146-9592, 1539-4794. DOI: 10.1364/OL.26.000039. URL: https://www.osapublishing.org/abstract.cfm?URI=ol-26-1-39 (visited on 12/14/2020).

[50] François Leo et al. "Temporal cavity solitons in one-dimensional Kerr media as bits in an all-optical buffer". en. In: *Nature Photon* 4.7 (July 2010), pp. 471–476. ISSN: 1749-4885, 1749-4893. DOI: 10.1038/nphoton.2010.120. URL: http://www.nature.com/articles/nphoton.2010.120 (visited on 12/14/2020).

[51] T. Herr et al. "Temporal solitons in optical microresonators". en. In: *Nature Photon* 8.2 (Feb. 2014), pp. 145–152. ISSN: 1749-4885, 1749-4893. DOI: 10.1038/nphoton.2013.343. URL: http://www.nature.com/articles/nphoton.2013.343 (visited on 10/28/2021).

[52] Ewelina Obrzud, Steve Lecomte, and Tobias Herr. "Temporal solitons in microresonators driven by optical pulses". en. In: *Nature Photon* 11.9 (Sept. 2017). Number: 9 Publisher: Nature Publishing Group, pp. 600–607. ISSN: 1749-4893. DOI: 10.1038/nphoton.2017.140. URL: https://www.nature.com/articles/nphoton.2017.140 (visited on 08/29/2023).

[53] Alessia Pasquazi et al. "Micro-combs: A novel generation of optical sources". en. In: *Physics Reports* 729 (Jan. 2018), pp. 1–81. ISSN: 03701573. DOI: 10.1016/j.physrep.2017.08.004. URL: https://linkinghub.elsevier.com/retrieve/pii/S0370157317303253 (visited on 10/28/2021).

[54] Thomas Bunel et al. "Observation of modulation instability Kerr frequency combs in a fiber Fabry–Pérot resonator". en. In: *Opt. Lett.* 48.2 (Jan. 2023), p. 275. ISSN: 0146-9592, 1539-4794. DOI: 10.1364/OL.479466. URL: https://opg.optica.org/abstract.cfm?URI=ol-48-2-275 (visited on 01/31/2023).

[55] P Del'Haye et al. "Optical frequency comb generation from a monolithic microresonator". en. In: 450 (2007), p. 4.

[56] T.J. Kippenberg, Holzwarth, and Diddams. "Microresonator-Based Optical Frequency Combs". en. In: (Apr. 2011), p. 6.

[57] D. Anderson and M. Lisak. "Modulational instability of coherent optical-fiber transmission signals". en. In: *Opt. Lett.* 9.10 (Oct. 1984), p. 468. ISSN: 0146-9592, 1539-4794. DOI: 10.1364/OL.9.000468. URL: https://www.osapublishing.org/abstract.cfm?URI=ol-9-10-468 (visited on 12/15/2020).

[58] Magnus Karlsson. "Modulational instability in lossy optical fibers". en. In: *J. Opt. Soc. Am. B* 12.11 (Nov. 1995), p. 2071. ISSN: 0740-3224, 1520-8540. DOI: 10.1364/JOSAB.12.002071. URL: https://www.osapublishing.org/abstract.cfm?URI=josab-12-11-2071 (visited on 12/17/2021).

[59] Auro M. Perego, Sergei K. Turitsyn, and Kestutis Staliunas. "Gain through losses in nonlinear optics". en. In: *Light: Science & Applications* 7.1 (Aug. 2018). Number: 1 Publisher: Nature Publishing Group, p. 43. ISSN: 2047-7538. DOI: 10.1038/s41377-018-0042-9. URL: http://www.nature.com/articles/s41377-018-0042-9 (visited on 05/26/2020).

[60] Auro M. Perego, Arnaud Mussot, and Matteo Conforti. "Theory of filter-induced modulation instability in driven passive optical resonators". en. In: *Phys. Rev. A* 103.1 (Jan. 2021), p. 013522. ISSN: 2469-9926, 2469-9934. DOI: 10.1103/PhysRevA.103.013522. URL: https://link.aps.org/doi/10.1103/PhysRevA.103.013522 (visited on 08/26/2021).

[61] Florent Bessin et al. "Gain-through-filtering enables tuneable frequency comb generation in passive optical resonators". en. In: *Nature Communications* 10.1 (Oct. 2019). Number: 1 Publisher: Nature Publishing Group, p. 4489. ISSN: 2041-1723. DOI: 10.1038/s41467-019-12375-3. URL: https://www.nature.com/articles/s41467-019-12375-3 (visited on 06/09/2020).

[62] Guy Millot et al. "Frequency-agile dual-comb spectroscopy". en. In: *Nature Photon* 10.1 (Jan. 2016). Number: 1 Publisher: Nature Publishing Group, pp. 27–30. ISSN: 1749-4893. DOI: 10.1038/nphoton.2015.250. URL: https://www.nature.com/articles/nphoton.2015.250 (visited on 09/28/2023).

[63] Yiqing Xu et al. "Dual-microcomb generation in a synchronously driven waveguide ring resonator". en. In: *Optics Letters* 46.23 (Dec. 2021), p. 6002. ISSN: 0146-9592, 1539-4794. DOI: 10.1364/OL.443153. URL: https://www.osapublishing.org/abstract.cfm?URI=ol-46-23-6002 (visited on 12/07/2021).

[64] Nicolas Englebert et al. "Temporal solitons in a coherently driven active resonator". en. In: *Nat. Photon.* 15.7 (July 2021), pp. 536–541. ISSN: 1749-4885, 1749-4893. DOI: 10.1038/s41566-021-00807-w. URL: http://www.nature.com/articles/s41566-021-00807-w (visited on 10/22/2021).

[65] Nicolas Englebert et al. “Parametrically driven Kerr cavity solitons”. en. In: *Nat. Photon.* 15.11 (Nov. 2021), pp. 857–861. ISSN: 1749-4885, 1749-4893. DOI: 10.1038/s41566-021-00858-z. URL: https://www.nature.com/articles/s41566-021-00858-z (visited on 04/12/2022).

[66] Nicolas Englebert et al. “Bloch oscillations of coherently driven dissipative solitons in a synthetic dimension”. en. In: *Nat. Phys.* 19.7 (July 2023). Number: 7 Publisher: Nature Publishing Group, pp. 1014–1021. ISSN: 1745-2481. DOI: 10.1038/s41567-023-02005-7. URL: https://www.nature.com/articles/s41567-023-02005-7 (visited on 09/14/2023).

[67] K. Ikeda, H. Daido, and O. Akimoto. “Optical Turbulence: Chaotic Behavior of Transmitted Light from a Ring Cavity”. en. In: *Phys. Rev. Lett.* 45.9 (Sept. 1980), pp. 709–712. ISSN: 0031-9007. DOI: 10.1103/PhysRevLett.45.709. URL: https://link.aps.org/doi/10.1103/PhysRevLett.45.709 (visited on 12/10/2020).

[68] L. A. Lugiato and R. Lefever. “Spatial Dissipative Structures in Passive Optical Systems”. en. In: *Phys. Rev. Lett.* 58.21 (May 1987), pp. 2209–2211. ISSN: 0031-9007. DOI: 10.1103/PhysRevLett.58.2209. URL: https://link.aps.org/doi/10.1103/PhysRevLett.58.2209 (visited on 12/08/2022).

[69] Govind Agrawal. “Introduction”. en. In: Elsevier, 2013, pp. 1–25. ISBN: 978-0-12-397023-7. DOI: 10.1016/B978-0-12-397023-7.00001-2. URL: https://linkinghub.elsevier.com/retrieve/pii/B9780123970237000012 (visited on 07/03/2023).

[70] R. F. Cregan et al. “Single-Mode Photonic Band Gap Guidance of Light in Air”. en. In: *Science* 285.5433 (Sept. 1999), pp. 1537–1539. ISSN: 0036-8075, 1095-9203. DOI: 10.1126/science.285.5433.1537. URL: https://www.science.org/doi/10.1126/science.285.5433.1537 (visited on 07/03/2023).

[71] Govind Agrawal. “Self-Phase Modulation”. en. In: Elsevier, 2013, pp. 87–128. ISBN: 978-0-12-397023-7. DOI: 10.1016/B978-0-12-397023-7.00004-8. URL: https://linkinghub.elsevier.com/retrieve/pii/B9780123970237000048 (visited on 07/03/2023).

[72] Govind Agrawal. “Group-Velocity Dispersion”. en. In: Elsevier, 2013, pp. 57–85. ISBN: 978-0-12-397023-7. DOI: 10.1016/B978-0-12-397023-7.00003-6. URL: https://linkinghub.elsevier.com/retrieve/pii/B9780123970237000036 (visited on 07/03/2023).

[73] Govind Agrawal. “Pulse Propagation in Fibers”. en. In: Elsevier, 2013, pp. 27–56. ISBN: 978-0-12-397023-7. DOI: 10.1016/B978-0-12-397023-7.00002-4. URL: https://linkinghub.elsevier.com/retrieve/pii/B9780123970237000024 (visited on 07/03/2023).

[74] François Copie et al. “Modulation instability in the weak dispersion regime of a dispersion modulated passive fiber-ring cavity”. en. In: *Opt. Express* 25.10 (May 2017), p. 11283. ISSN: 1094-4087. DOI: 10.1364/OE.25.011283. URL: https://www.osapublishing.org/abstract.cfm?URI=oe-25-10-11283 (visited on 07/19/2021).

[75] F Bessin et al. “Modulation instability in the weak normal dispersion region of passive fiber ring cavities”. en. In: (2017), p. 4.

[76] Govind P. Agrawal. “Optical Solitons”. en. In: Elsevier, 2013, pp. 129–191. ISBN: 978-0-12-397023-7. DOI: 10.1016/B978-0-12-397023-7.00005-X. URL: https://linkinghub.elsevier.com/retrieve/pii/B978012397023700005X (visited on 07/03/2023).

[77] Kensuke Ikeda. “Multiple-valued stationary state and its instability of the transmitted light by a ring cavity system”. en. In: *Optics Communications* 30.2 (Aug. 1979), pp. 257–261. ISSN: 00304018. DOI: 10.1016/0030-4018(79)90090-7. URL: https://linkinghub.elsevier.com/retrieve/pii/0030401879900907 (visited on 12/10/2020).

[78] L. F. Stokes, M. Chodorow, and H. J. Shaw. “All-single-mode fiber resonator”. en. In: *Opt. Lett.* 7.6 (June 1982), p. 288. ISSN: 0146-9592, 1539-4794. DOI: 10.1364/OL.7.000288. URL: https://www.osapublishing.org/abstract.cfm?URI=ol-7-6-288 (visited on 01/20/2021).

[79] J.E. Heebner et al. “Optical transmission characteristics of fiber ring resonators”. en. In: *IEEE J. Quantum Electron.* 40.6 (June 2004), pp. 726–730. ISSN: 0018-9197. DOI: 10.1109/JQE.2004.828232. URL: http://ieeexplore.ieee.org/document/1303787/ (visited on 05/22/2023).

[80] S. Coen et al. “Experimental investigation of the dynamics of a stabilized nonlinear fiber ring resonator”. en. In: *J. Opt. Soc. Am. B* 15.8 (Aug. 1998), p. 2283. ISSN: 0740-3224, 1520-8540. DOI: 10.1364/JOSAB.15.002283. URL: https://www.osapublishing.org/abstract.cfm?URI=josab-15-8-2283 (visited on 10/13/2021).

[81] Arnaud Mussot et al. “Modulation instability in dispersion oscillating fibers”. EN. In: *Adv. Opt. Photon., AOP* 10.1 (Mar. 2018). Publisher: Optica Publishing Group, pp. 1–42. ISSN: 1943-8206. DOI: 10.1364/AOP.10.000001. URL: https://opg.optica.org/aop/abstract.cfm?uri=aop-10-1-1 (visited on 05/13/2023).

[82] Florent Bessin et al. “Real-Time Characterization of Period-Doubling Dynamics in Uniform and Dispersion Oscillating Fiber Ring Cavities”. In: *Phys. Rev. X* 9.4 (Nov. 2019). Publisher: American Physical Society, p. 041030. DOI: 10.1103/PhysRevX.9.041030. URL: https://link.aps.org/doi/10.1103/PhysRevX.9.041030 (visited on 03/15/2022).

[83] K. Ikeda and O. Akimoto. “Instability Leading to Periodic and Chaotic Self-Pulsations in a Bistable Optical Cavity”. en. In: *Phys. Rev. Lett.* 48.9 (Mar. 1982), pp. 617–620. ISSN: 0031-9007. DOI: 10.1103/PhysRevLett.48.617. URL: https://link.aps.org/doi/10.1103/PhysRevLett.48.617 (visited on 04/07/2020).

[84] S. Coen et al. “Convection versus Dispersion in Optical Bistability”. en. In: *Phys. Rev. Lett.* 83.12 (Sept. 1999), pp. 2328–2331. ISSN: 0031-9007, 1079-7114. DOI: 10.1103/PhysRevLett.83.2328. URL: https://link.aps.org/doi/10.1103/PhysRevLett.83.2328 (visited on 06/23/2021).

[85] Tobias Hansson and Stefan Wabnitz. “Frequency comb generation beyond the Lugiato–Lefever equation: multi-stability and super cavity solitons”. en. In: *J. Opt. Soc. Am. B* 32.7 (July 2015), p. 1259. ISSN: 0740-3224, 1520-8540. DOI: 10.1364/JOSAB.32.001259. URL: https://opg.optica.org/abstract.cfm?URI=josab-32-7-1259 (visited on 04/05/2022).

[86] Stefania Malaguti, Matteo Conforti, and Stefano Trillo. “Dispersive radiation induced by shock waves in passive resonators”. en. In: *Opt. Lett.* 39.19 (Oct. 2014), p. 5626. ISSN: 0146-9592, 1539-4794. DOI: 10.1364/OL.39.005626. URL: https://www.osapublishing.org/abstract.cfm?URI=ol-39-19-5626 (visited on 11/03/2021).

[87] Stefania Malaguti, Gaetano Bellanca, and Stefano Trillo. “Dispersive wave-breaking in coherently driven passive cavities”. en. In: *Opt. Lett.* 39.8 (Apr. 2014), p. 2475. ISSN: 0146-9592, 1539-4794. DOI: 10.1364/OL.39.002475. URL: https://www.osapublishing.org/abstract.cfm?URI=ol-39-8-2475 (visited on 11/03/2021).

[88] Fabrizio Castelli et al. “The LLE, pattern formation and a novel coherent source”. en. In: *Eur. Phys. J. D* 71.4 (Apr. 2017), p. 84. ISSN: 1434-6060, 1434-6079. DOI: 10.1140/epjd/e2017-70754-1. URL: http://link.springer.com/10.1140/epjd/e2017-70754-1 (visited on 07/06/2023).

[89] L. A. Lugiato et al. “From the Lugiato–Lefever equation to microresonator-based soliton Kerr frequency combs”. In: *Philosophical Transactions of the Royal Society A: Mathematical, Physical and Engineering Sciences* 376.2135 (Dec. 2018). Publisher: Royal Society, p. 20180113. DOI: 10.1098/rsta.

2018.0113. URL: http://royalsocietypublishing.org/doi/10.1098/rsta.2018.0113 (visited on 12/09/2022).

[90] M. Haelterman, S. Trillo, and S. Wabnitz. "Additive-modulation-instability ring laser in the normal dispersion regime of a fiber". en. In: *Opt. Lett.* 17.10 (May 1992), p. 745. ISSN: 0146-9592, 1539-4794. DOI: 10.1364/OL.17.000745. URL: https://www.osapublishing.org/abstract.cfm?URI=ol-17-10-745 (visited on 03/30/2020).

[91] V. E. Zakharov and L. A. Ostrovsky. "Modulation instability: The beginning". en. In: *Physica D: Nonlinear Phenomena* 238.5 (Mar. 2009), pp. 540–548. ISSN: 0167-2789. DOI: 10.1016/j.physd.2008.12.002. URL: http://www.sciencedirect.com/science/article/pii/S0167278908004223 (visited on 03/12/2020).

[92] B Ghosh and K P Das. "Modulational instability of electron plasma waves in a cylindrical wave guide". en. In: *Plasma Phys. Control. Fusion* 27.9 (Sept. 1985), pp. 969–982. ISSN: 0741-3335. DOI: 10.1088/0741-3335/27/9/003. URL: https://iopscience.iop.org/article/10.1088/0741-3335/27/9/003 (visited on 10/05/2021).

[93] Conrad Bertrand Tabi, Phelo Otlaadisa, and Timoléon Crépin Kofané. "Modulation instability of two-dimensional Bose-Einstein condensates with helicoidal and a mixture of Rashba-Dresselhaus spin-orbit couplings". en. In: *Physics Letters A* 449 (Oct. 2022), p. 128334. ISSN: 03759601. DOI: 10.1016/j.physleta.2022.128334. URL: https://linkinghub.elsevier.com/retrieve/pii/S0375960122004169 (visited on 07/03/2023).

[94] Govind P. Agrawal. "Modulation instability induced by cross-phase modulation". en. In: *Phys. Rev. Lett.* 59.8 (Aug. 1987), pp. 880–883. ISSN: 0031-9007. DOI: 10.1103/PhysRevLett.59.880. URL: https://link.aps.org/doi/10.1103/PhysRevLett.59.880 (visited on 10/04/2021).

[95] Joshua E. Rothenberg. "Modulational instability for normal dispersion". In: *Physical Review A* 42.1 (July 1990). Publisher: American Physical Society, pp. 682–685. DOI: 10.1103/PhysRevA.42.682. URL: https://link.aps.org/doi/10.1103/PhysRevA.42.682 (visited on 09/09/2023).

[96] John D. Harvey et al. "Scalar modulation instability in the normal dispersion regime by use of a photonic crystal fiber". en. In: *Optics Letters* 28.22 (Nov. 2003), p. 2225. ISSN: 0146-9592, 1539-4794. DOI: 10.1364/OL.28.002225. URL: https://opg.optica.org/abstract.cfm?URI=ol-28-22-2225 (visited on 09/09/2023).

[97] M. Guasoni. "Generalized modulational instability in multimode fibers: Wideband multimode parametric amplification". In: *Physical Review A* 92.3 (Sept. 2015). Publisher: American Physical Society, p. 033849. DOI: 10.1103/PhysRevA.92.033849. URL: https://link.aps.org/doi/10.1103/PhysRevA.92.033849 (visited on 09/09/2023).

[98] M. Haelterman. "Period-doubling bifurcations and modulational instability in the nonlinear ring cavity: an analytical study". en. In: *Opt. Lett.* 17.11 (June 1992), p. 792. ISSN: 0146-9592, 1539-4794. DOI: 10.1364/OL.17.000792. URL: https://www.osapublishing.org/abstract.cfm?URI=ol-17-11-792 (visited on 10/13/2021).

[99] Matteo Conforti et al. "Parametric instabilities in modulated fiber ring cavities". en. In: *Opt. Lett.* 41.21 (Nov. 2016), p. 5027. ISSN: 0146-9592, 1539-4794. DOI: 10.1364/OL.41.005027. URL: https://www.osapublishing.org/abstract.cfm?URI=ol-41-21-5027 (visited on 09/14/2021).

[100] John Bechhoefer. "Kramers–Kronig, Bode, and the meaning of zero". en. In: *American Journal of Physics* 79.10 (Oct. 2011), pp. 1053–1059. ISSN: 0002-9505, 1943-2909. DOI: 10.1119/1.3614039. URL: http://aapt.scitation.org/doi/10.1119/1.3614039 (visited on 12/09/2021).

[101] François Copie et al. "Competing Turing and Faraday Instabilities in Longitudinally Modulated Passive Resonators". en. In: *Phys. Rev. Lett.* 116.14 (Apr. 2016), p. 143901. ISSN: 0031-9007, 1079-7114. DOI: 10.1103/PhysRevLett.116.143901. URL: https://link.aps.org/doi/10.1103/PhysRevLett.116.143901 (visited on 10/04/2021).

[102] Léon Brillouin. "Diffusion de la lumière et des rayons X par un corps transparent homogène: Influence de l'agitation thermique". fr. In: *Ann. Phys.* 9.17 (1922), pp. 88–122. ISSN: 0003-4169, 1286-4838. DOI: 10.1051/anphys/192209170088. URL: http://www.annphys.org/10.1051/anphys/192209170088 (visited on 07/12/2023).

[103] Andrey Kobyakov, Michael Sauer, and Dipak Chowdhury. "Stimulated Brillouin scattering in optical fibers". en. In: *Adv. Opt. Photon.* 2.1 (Mar. 2010), p. 1. ISSN: 1943-8206. DOI: 10.1364/AOP.2.000001. URL: https://opg.optica.org/aop/abstract.cfm?uri=aop-2-1-1 (visited on 04/27/2023).

[104] J. K. Jang and S. G. Murdoch. "Strong Brillouin suppression in a passive fiber ring resonator". en. In: *Opt. Lett.* 37.7 (Apr. 2012), p. 1256. ISSN: 0146-9592, 1539-4794. DOI: 10.1364/OL.37.001256. URL: https://opg.optica.org/abstract.cfm?URI=ol-37-7-1256 (visited on 04/27/2023).

[105] Stefano Negrini et al. “Pump-cavity synchronization mismatch in modulation instability induced optical frequency combs”. en. In: *Phys. Rev. Research* 5.2 (May 2023), p. 023133. ISSN: 2643-1564. DOI: 10.1103/PhysRevResearch.5.023133. URL: https://link.aps.org/doi/10.1103/PhysRevResearch.5.023133 (visited on 07/12/2023).

[106] R. W. P. Drever et al. “Laser phase and frequency stabilization using an optical resonator”. en. In: *Applied Physics B Photophysics and Laser Chemistry* 31.2 (June 1983), pp. 97–105. ISSN: 0721-7269, 1432-0649. DOI: 10.1007/BF00702605. URL: http://link.springer.com/10.1007/BF00702605 (visited on 07/12/2023).

[107] B P and Abbott. “LIGO: the Laser Interferometer Gravitational-Wave Observatory”. en. In: *Rep. Prog. Phys.* 72.7 (July 2009), p. 076901. ISSN: 0034-4885, 1361-6633. DOI: 10.1088/0034-4885/72/7/076901. URL: https://iopscience.iop.org/article/10.1088/0034-4885/72/7/076901 (visited on 07/13/2023).

[108] Stefan Seel et al. “Cryogenic Optical Resonators: A New Tool for Laser Frequency Stabilization at the 1 Hz Level”. en. In: *Phys. Rev. Lett.* 78.25 (June 1997), pp. 4741–4744. ISSN: 0031-9007, 1079-7114. DOI: 10.1103/PhysRevLett.78.4741. URL: https://link.aps.org/doi/10.1103/PhysRevLett.78.4741 (visited on 07/13/2023).

[109] Eric D. Black. “An introduction to Pound–Drever–Hall laser frequency stabilization”. en. In: *American Journal of Physics* 69.1 (Jan. 2001), pp. 79–87. ISSN: 0002-9505, 1943-2909. DOI: 10.1119/1.1286663. URL: http://aapt.scitation.org/doi/10.1119/1.1286663 (visited on 01/12/2021).

[110] E. Mimoun et al. “Solid-state laser system for laser cooling of sodium”. en. In: *Appl. Phys. B* 99.1-2 (Apr. 2010), pp. 31–40. ISSN: 0946-2171, 1432-0649. DOI: 10.1007/s00340-009-3844-x. URL: http://link.springer.com/10.1007/s00340-009-3844-x (visited on 07/13/2023).

[111] Govind Agrawal. “Numerical Code for the NLS Equation”. en. In: Elsevier, 2013, pp. 615–617. ISBN: 978-0-12-397023-7. DOI: 10.1016/B978-0-12-397023-7.00015-2. URL: https://linkinghub.elsevier.com/retrieve/pii/B9780123970237000152 (visited on 07/03/2023).

[112] M. Haelterman, S. Trillo, and S. Wabnitz. “Polarization multistability and instability in a nonlinear dispersive ring cavity”. en. In: *J. Opt. Soc. Am. B* 11.3 (Mar. 1994), p. 446. ISSN: 0740-3224, 1520-8540. DOI: 10.1364/JOSAB.11.000446. URL: https://www.osapublishing.org/abstract.cfm?URI=josab-11-3-446 (visited on 12/13/2020).

[113] Julien Fatome et al. "Polarization modulation instability in a nonlinear fiber Kerr resonator". en. In: *Opt. Lett.* 45.18 (Sept. 2020), p. 5069. ISSN: 0146-9592, 1539-4794. DOI: 10.1364/OL.400474. URL: https://www.osapublishing.org/abstract.cfm?URI=ol-45-18-5069 (visited on 04/29/2021).

[114] D. Amans et al. "Vector modulation instability induced by vacuum fluctuations in highly birefringent fibers in the anomalous-dispersion regime". en. In: *Opt. Lett.* 30.9 (May 2005), p. 1051. ISSN: 0146-9592, 1539-4794. DOI: 10.1364/OL.30.001051. URL: https://opg.optica.org/abstract.cfm?URI=ol-30-9-1051 (visited on 11/23/2022).

[115] Stefan Wabnitz. "Modulational polarization instability of light in a nonlinear birefringent dispersive medium". en. In: *Phys. Rev. A* 38.4 (Aug. 1988), pp. 2018–2021. ISSN: 0556-2791. DOI: 10.1103/PhysRevA.38.2018. URL: https://link.aps.org/doi/10.1103/PhysRevA.38.2018 (visited on 11/23/2022).

[116] E. Seve et al. "Modulational instability and critical regime in a highly birefringent fiber". en. In: *Phys. Rev. A* 54.4 (Oct. 1996), pp. 3519–3534. ISSN: 1050-2947, 1094-1622. DOI: 10.1103/PhysRevA.54.3519. URL: https://link.aps.org/doi/10.1103/PhysRevA.54.3519 (visited on 11/25/2022).

[117] B. Frisquet et al. "Polarization modulation instability in a Manakov fiber system". en. In: *Phys. Rev. A* 92.5 (Nov. 2015), p. 053854. ISSN: 1050-2947, 1094-1622. DOI: 10.1103/PhysRevA.92.053854. URL: https://link.aps.org/doi/10.1103/PhysRevA.92.053854 (visited on 11/23/2022).

[118] Xin Zhao et al. "Polarization-multiplexed, dual-comb all-fiber mode-locked laser". en. In: *Photonics Research* 6.9 (Sept. 2018), p. 853. ISSN: 2327-9125. DOI: 10.1364/PRJ.6.000853. URL: https://opg.optica.org/abstract.cfm?URI=prj-6-9-853 (visited on 05/12/2023).

[119] Chenghong Zhang et al. "Recent Advances and Outlook in Single-Cavity Dual Comb Lasers". en. In: *Photonics* 10.2 (Feb. 2023), p. 221. ISSN: 2304-6732. DOI: 10.3390/photonics10020221. URL: https://www.mdpi.com/2304-6732/10/2/221 (visited on 05/12/2023).

[120] J.F. Botero-Cadavid, J.D. Causado-Buelvas, and P. Torres. "Spectral Properties of Locally Pressed Fiber Bragg Gratings Written in Polarization Maintaining Fibers". en. In: *J. Lightwave Technol.* 28.9 (May 2010), pp. 1291–1297. ISSN: 0733-8724, 1558-2213. DOI: 10.1109/JLT.2010.2040804. URL: http://ieeexplore.ieee.org/document/5406112/ (visited on 01/13/2023).

[121] Dipen Barot, Gang Wang, and Lingze Duan. “High-Resolution Dynamic Strain Sensor Using a Polarization-Maintaining Fiber Bragg Grating”. In: *IEEE Photonics Technology Letters* 31.9 (May 2019). Conference Name: IEEE Photonics Technology Letters, pp. 709–712. ISSN: 1941-0174. DOI: 10.1109/LPT.2019.2905951.

[122] Govind Agrawal. “Cross-Phase Modulation”. en. In: Elsevier, 2013, pp. 245–293. ISBN: 978-0-12-397023-7. DOI: 10.1016/B978-0-12-397023-7.00007-3. URL: https://linkinghub.elsevier.com/retrieve/pii/B9780123970237000073 (visited on 07/03/2023).

[123] Sandro M. Link et al. “Dual-comb modelocked laser”. en. In: *Optics Express* 23.5 (Mar. 2015), p. 5521. ISSN: 1094-4087. DOI: 10.1364/OE.23.005521. URL: https://opg.optica.org/abstract.cfm?URI=oe-23-5-5521 (visited on 05/12/2023).

[124] S. Mehravar et al. “Real-time dual-comb spectroscopy with a free-running bidirectionally mode-locked fiber laser”. en. In: *Applied Physics Letters* 108.23 (June 2016), p. 231104. ISSN: 0003-6951, 1077-3118. DOI: 10.1063/1.4953400. URL: https://pubs.aip.org/aip/apl/article/311808 (visited on 05/12/2023).

[125] Ruoyu Liao et al. “Dual-comb generation from a single laser source: principles and spectroscopic applications towards mid-IR—A review”. en. In: *Journal of Physics: Photonics* 2.4 (Sept. 2020), p. 042006. ISSN: 2515-7647. DOI: 10.1088/2515-7647/aba66e. URL: https://iopscience.iop.org/article/10.1088/2515-7647/aba66e (visited on 05/12/2023).

[126] Jiang Li et al. “Efficiency of pulse pumped soliton microcombs”. EN. In: *Optica, OPTICA* 9.2 (Feb. 2022). Publisher: Optica Publishing Group, pp. 231–239. ISSN: 2334-2536. DOI: 10.1364/OPTICA.443060. URL: https://opg.optica.org/optica/abstract.cfm?uri=optica-9-2-231 (visited on 08/29/2023).

[127] Tobias J. Kippenberg et al. “Dissipative Kerr solitons in optical microresonators”. en. In: *Science* 361.6402 (Aug. 2018). Publisher: American Association for the Advancement of Science Section: Review. ISSN: 0036-8075, 1095-9203. DOI: 10.1126/science.aan8083. URL: http://science.sciencemag.org/content/361/6402/eaan8083 (visited on 11/19/2020).

[128] M. Schmidberger et al. “Influence of timing jitter on nonlinear dynamics of a photonic crystal fiber ring cavity”. en. In: *Opt. Lett.* 37.17 (Sept. 2012), p. 3576. ISSN: 0146-9592, 1539-4794. DOI: 10.1364/OL.37.003576. URL: https://opg.optica.org/abstract.cfm?URI=ol-37-17-3576 (visited on 08/29/2023).

[129] Ian Hendry et al. "Spontaneous symmetry breaking and trapping of temporal Kerr cavity solitons by pulsed or amplitude-modulated driving fields". In: *Phys. Rev. A* 97.5 (May 2018). Publisher: American Physical Society, p. 053834. DOI: 10.1103/PhysRevA.97.053834. URL: https://link.aps.org/doi/10.1103/PhysRevA.97.053834 (visited on 08/29/2023).

[130] Ian Hendry et al. "Impact of desynchronization and drift on soliton-based Kerr frequency combs in the presence of pulsed driving fields". In: *Phys. Rev. A* 100.2 (Aug. 2019). Publisher: American Physical Society, p. 023829. DOI: 10.1103/PhysRevA.100.023829. URL: https://link.aps.org/doi/10.1103/PhysRevA.100.023829 (visited on 08/29/2023).

[131] Laurence S. Hall and Warren Heckrotte. "Instabilities: Convective versus Absolute". en. In: *Phys. Rev.* 166.1 (Feb. 1968), pp. 120–128. ISSN: 0031-899X. DOI: 10.1103/PhysRev.166.120. URL: https://link.aps.org/doi/10.1103/PhysRev.166.120 (visited on 09/05/2023).

[132] M. Yu and C. J. McKinstrie. "Impulse response of a nonlinear dispersive wave". en. In: *Phys. Rev. E* 52.6 (Dec. 1995), pp. 6826–6832. ISSN: 1063-651X, 1095-3787. DOI: 10.1103/PhysRevE.52.6826. URL: https://link.aps.org/doi/10.1103/PhysRevE.52.6826 (visited on 10/16/2023).

[133] Saliya Coulibaly et al. "Spatiotemporal wave-train instabilities in nonlinear Schrödinger equation: revisited". en. In: *Eur. Phys. J. D* 69.7 (July 2015), p. 186. ISSN: 1434-6060, 1434-6079. DOI: 10.1140/epjd/e2015-60212-7. URL: http://link.springer.com/10.1140/epjd/e2015-60212-7 (visited on 10/16/2023).

[134] A. Haboucha et al. "Analysis of soliton pattern formation in passively mode-locked fiber lasers". In: *Phys. Rev. A* 78.4 (Oct. 2008). Publisher: American Physical Society, p. 043806. DOI: 10.1103/PhysRevA.78.043806. URL: https://link.aps.org/doi/10.1103/PhysRevA.78.043806 (visited on 09/14/2023).

[135] Nicolas Englebert. *Temporal solitons in coherently driven active cavity*. PhD Thesis, Université Libre de Bruxelles, 2022.

[136] Weiqiang Wang et al. "Dual-pump Kerr Micro-cavity Optical Frequency Comb with varying FSR spacing". en. In: *Sci Rep* 6.1 (Sept. 2016), p. 28501. ISSN: 2045-2322. DOI: 10.1038/srep28501. URL: http://www.nature.com/articles/srep28501 (visited on 07/01/2021).

[137] Paul Skolik, Martin R. McAinsh, and Francis L. Martin. "Biospectroscopy for Plant and Crop Science". en. In: *Comprehensive Analytical Chemistry*. Vol. 80. Elsevier, 2018, pp. 15–49. ISBN: 978-0-444-64048-2. DOI: 10.1016/bs.coac.2018.03.001. URL: https://linkinghub.elsevier.com/retrieve/pii/S0166526X18300072 (visited on 09/28/2023).

[138] Vicente Durán, Peter A. Andrekson, and Víctor Torres-Company. "Electro-optic dual-comb interferometry over 40 nm bandwidth". EN. In: *Opt. Lett., OL* 41.18 (Sept. 2016). Publisher: Optica Publishing Group, pp. 4190–4193. ISSN: 1539-4794. DOI: 10.1364/OL.41.004190. URL: https://opg.optica.org/ol/abstract.cfm?uri=ol-41-18-4190 (visited on 09/28/2023).

[139] Alexandre Parriaux, Kamal Hammani, and Guy Millot. "Two-micron all-fibered dual-comb spectrometer based on electro-optic modulators and wavelength conversion". en. In: *Commun Phys* 1.1 (May 2018), p. 17. ISSN: 2399-3650. DOI: 10.1038/s42005-018-0017-4. URL: https://www.nature.com/articles/s42005-018-0017-4 (visited on 09/28/2023).

Appendix B

Author's bibliography

Publications in peer-reviewed journals:

- S. Negrini, S. Coulibaly, F. Copie, M. Taki, and A. Mussot, 'Pump-cavity synchronization mismatch in modulation instability induced optical frequency combs', Phys. Rev. Research, vol. 5, no. 2, p. 023133, May 2023, doi: 10.1103/PhysRevResearch.5.023133.

Publications in peer-reviewed journals accepted:

- S. Negrini, JB Ceppe, A. Perego, A. Kudlinski, M. conforti and A. Mussot," Coexistence of Gain Through Filtering and Boundary conditions parametric gain in an optical cavity", Opt. Express

Oral presentation at conferences:

- S. Negrini, S. Coulibaly, F. Copie, M. Taki, and A. Mussot, "Effect of synchronization mismatch on modulation instability in passive fiber-ring cavity", GDR ELIOS 2020 ;
- Negrini, S. Coulibaly, F. Copie, M. Taki, and A. Mussot, , "Effect of synchronization mismatch on modulation instability in passive fiber-ring cavity", CLEO Europe 2021;
- S. Negrini, J.B. Ceppe, A. Perego, A. Kudlinski, M. conforti and A. Mussot "Coexistence of Gain Through Filtering and Boundary conditions parametric gain in an optical cavity", GDR ELIOS 2021 ;
- S. Negrini, J.B. Ceppe, A. Perego, A. Kudlinski, M. conforti and A. Mussot " Coexistence of Gain through Filtering and Parametric Instability in a Fiber Ring Cavity", Advanced Photonic 2022

- S. Negrini, A. Perego, A. Kudlinski, M. conforti and A. Mussot , Dual frequency comb like source with PM passive fiber cavity and GTF ' EOSAM 2023

Invited international conference:

- S. Negrini, A. Perego, M. Conforti, A. Kudlinski, C. Naveau, P. Szriftgiser, G. Vanderhagen, A. Mussot "Gain through filtering in optical fibers" , OSA Conference CLEO, San Jose USA (2022)

Publications in preparation:

- S. Negrini, A. Perego, M. Conforti and A. Mussot, 'Dual frequency comb generation exploiting gain through filtering effect in birefringent polarisation maintaning fiber ring cavity , Opt. Express
- S. Negrini, M. Shi, A. Perego and A. Mussot, 'GTF in active resonator', Opt. Letters
- M. Bartnick, S. Negrini, A. Mussot and C. Bress 'Experimental observation of modulation instability in a fiber resonator pumped at 2 micron', Opt. Letters

Contents

Gain through filtering in fiber cavity resonators

Abstract

In this work, we study the phenomenon of modulation instability (IM) in fiber ring resonators, induced by asymmetric spectral losses in the form of a filter. The phenomenon, known as gain through filtering (GTF), consists in the modification of the phase matching condition of the resonator, given by the phase signature of the filter. We first characterised this phenomenon theoretically and experimentally in a passive fibre resonator for both normal and anomalous dispersion regimes, highlighting the relationship between GTF instabilities and parametric MI. We then developed a theoretical model to describe the formation of GTFs in a polarisation-maintaining (PM) cavity. Using this model, we have shown how it is theoretically possible to obtain two MI spectra with detuned spectral peaks. This is made possible by using a PM filter with a different loss profile in the two polarisation axes. In the more general context of fibre cavities, we have studied the effect of a synchronisation mismatch between the repetition rate of the pulse train driving the cavity and the natural repetition rate of the cavity. The mismatch results in a shift of the sideband of the MI spectra due to the competition between two MI regimes: absolute and convective. Finally, we built two active cavity devices. They consist of a fibre cavity in which a section of doped fibre (erbium or thulium dopant) is embedded in the coil to act as an amplifier. By carefully adjusting the gain of the amplifier, it's possible to compensate for the losses and still remain in a passive regime (below the lasing threshold). By using erbium-doped fiber as active media we were able to obtain GTF at very low power, while by using thulium-doped fiber we were able to generate MI at a wavelength of $2\mu m$.

Keywords: nonlinear optics, optical fiber, passive fiber cavity, modulation instability, gain through filtering, active cavity

---

Laboratoire de Physique des Lasers, Atomes et Molécules - PhLam
2, Av. Jean Perrin – 59650 Villeneuve-d'Ascq – France

Gain induit par des filtres dans les cavités fibrées passives

Résumé

Dans ce travail, nous étudions le phénomène d'instabilité de la modulation (IM) dans les résonateurs en anneau à fibre, induit par des pertes spectrales asymétriques. Le phénomène, connu sous le nom de gain through filtering (GTF), consiste en la modification de la condition accord de phase du résonateur, donnée par la signature de phase du filtre. Nous avons d'abord caractérisé ce phénomène théoriquement et expérimentalement dans un résonateur à fibre passif pour les régimes de dispersion normale et anormale, en mettant en évidence la relation entre les instabilités GTF et le MI paramétrique. Nous avons ensuite développé un modèle théorique pour décrire la formation des GTF dans une cavité à maintien de polarisation (PM). En utilisant ce modèle, nous avons montré comment il est théoriquement possible d'obtenir deux spectres MI avec des pics spectraux désaccordés. Ceci est possible en utilisant un filtre PM avec un profil de perte différent dans les deux axes de polarisation. Dans le contexte plus général des cavités à fibres, nous avons étudié l'effet d'un décalage de synchronisation entre le taux de répétition du train d'impulsions qui alimente la cavité et le taux de répétition naturel de la cavité. Le décalage entraîne un déplacement de la bande latérale des spectres MI en raison de la concurrence entre deux régimes MI : absolu et convectif.Enfin, nous avons construit deux dispositifs à cavité active. Ils consistent en une cavité à fibre dans laquelle une section de fibre dopée (dopant erbium ou thulium) est incorporée dans la bobine pour agir comme un amplificateur. En ajustant soigneusement le gain de l'amplificateur, il est possible de compenser les pertes tout en restant dans un régime passif (en dessous du seuil de télédiffusion). En utilisant une fibre dopée à l'erbium comme média actif, nous avons pu obtenir une FGT à très faible puissance, tandis qu'en utilisant une fibre dopée au thulium, nous avons pu générer un MI à une longueur d'onde de $2\mu m$.

Mots clés : optique non linéaire, fibre optique, cavité de fibre passive, instabilité de la modulation, gain par filtrage, cavité active